



**Pontificia Universidad  
Católica del Perú  
Escuela de Posgrado**

**Synthesis and characterization of nanostructured ternary MAX-phase  
thin films prepared by magnetron sputtering as precursors for twodimensional  
MXenes**

Tesis para obtener el grado académico de  
Magistra en Ingeniería y Ciencia de los Materiales que presenta:

*Marta Miranda Martí*

**Asesor:**

*Dr.-Ing. Rolf Grieseler (Pontificia Universidad Católica del Perú)*

*Dr. rer. nat. habil. Dr. h. c. Peter Schaaf (Technische Universität Ilmenau)*

**Lima, 2023**

## Declaración jurada de autenticidad


Yo, Rolf Grieseler, docente de la Escuela de Posgrado de la Pontificia Universidad Católica del Perú, asesor de la tesis de investigación titulado “**Synthesis and characterization of nanostructured ternary MAX-phase thin films by magnetron sputtering as precursors to two-dimensional MXenes**”, de la autora Marta Miranda Marti, código PUCP: 20216970, alumna de la Maestría en Ingeniería y Ciencia de los Materiales.

dejo constancia de lo siguiente:

- El mencionado documento tiene un índice de puntuación de similitud de 18%. Así lo consigna el reporte de similitud emitido por el software *Turnitin* el 25/01/2023.
- He revisado con detalle dicho reporte y la Tesis o Trabajo de Suficiencia Profesional, y no se advierte indicios de plagio.
- Las citas a otros autores y sus respectivas referencias cumplen con las pautas académicas.

Lugar y fecha:

Lima, Perú 25/01/2023.

Grieseler Rolf	
CE: 001660902	Firma: 
ORCID: 0000-0001-5307-7755	

# Contents

<b>Acknowledgement</b>	<b>ii</b>
<b>Abstract</b>	<b>iii</b>
<b>1 Introduction</b>	<b>1</b>
<b>2 Experimental Methods</b>	<b>4</b>
2.1 Magnetron Sputtering MS	4
2.2 Rapid Thermal Annealing RTP	6
2.3 Raman Spectroscopy	7
2.4 X-Ray Diffraction XRD	13
2.5 Scanning Electron Microscopy SEM and Energy Dispersive X-Ray EDX	17
2.6 4-point probes method	19
2.7 Variable Angle Spectroscopic Ellipsometry VASE	19
2.8 Etching Method to synthesize MXenes	23
<b>3 Deposition of the ternary system Ti-Al-C</b>	<b>25</b>
3.1 Determination of the deposition rate	25
3.2 Co-sputtering of Ti-Al-C thin films	29
3.3 Influential parameters in the deposition of thin films via sputtering	38
3.4 Oblique Angle Deposition of the ternary system Ti-Al-C	41
<b>4 Selective HF Etching for MXenes synthesis</b>	<b>50</b>
4.1 HF Etching of MAX phase thin films	50
4.2 Etching of nanostructured MAX phase thin films deposited at OAD	65
<b>5 Summary and Conclusions</b>	<b>82</b>
<b>6 Further experiments</b>	<b>85</b>
<b>Acronym Glossary</b>	<b>87</b>
<b>Bibliography</b>	<b>89</b>
<b>List of Figures</b>	<b>99</b>
<b>List of Tables</b>	<b>105</b>
<b>Annex</b>	<b>107</b>
Annex 1	107
Annex 2	107
Annex 3	109
Annex 4	110
<b>Eigenständigkeitserklärung</b>	<b>111</b>
<b>Declaration of Originality</b>	<b>112</b>

# Acknowledgement

First of all, I would like to acknowledge the financial support by ProCiencia under the grant number 149-2020-FONDECYT. I would also like to express my deepest gratitude to Prof. Dr. Schaaf and Dr. Grieseler for the brain-storming for this thesis, and for always being available with help and advice. I also appreciate the valuable input offered by Claudia Morales, M.Sc. Magali Camargo, M.Sc. Carlos Torres and Dr. Andrés Torres. M.Sc. Lara Eggerts is acknowledged for providing the referential MAX phase thin film samples, as well as M.Sc. Theresa Scheler for helping synthesizing the samples.

Special thanks to the master and doctoral students of the Pontificia Universidad Católica del Perú for developing some of the experiments and concepts described, in particular to Fabiola Bravo, Erick Serquen, Zully Calderon, Luis Alonso, Miguel Piñeiro, and Francisco Severo, for their support in the characterization and experimental work, and for the wonderful time spend in Perú as part of my exchange program. Many thanks to my main support in this experience, Antonella Hadzich, who made me feel at home.

Lastly, I would be remiss in not mentioning my family, especially my parents Raquel and Javier, my grandparents, Carmen and Luis, and my sister, Raquel, who supported and encourage my journey, as well as my chosen family Maria Paula, Maria Ines, Marco Tulio, and, of course, Mario Baez, for the support, love and patience throughout these years.

# Abstract

MAX phase thin films can be fabricated through firstly depositing a precursor thin film consisting of the initial elements M, A, and X close to the MAX phase stoichiometry employing physical vapor deposition techniques with a subsequent thermal annealing process.

This work presents different deposition configurations (multilayer and co-sputtering) for the fabrication of the  $\text{Ti}_2\text{AlC}$  and  $\text{Ti}_3\text{AlC}_2$  MAX phase thin films by magnetron sputtering from three elemental targets (Ti, Al, and C). It was found that the depositions followed mainly amorphous thus the MAX phase was not able to form. By implementing the deposition parameters such as temperature and substrate voltage, the deposition morphology could be tailored to crystalline and MAX phases could be created.

Moreover,  $\text{Ti}_2\text{AlC}$  and  $\text{Ti}_3\text{AlC}_2$  nanostructured MAX phase thin films were fabricated by magnetron sputtering with three elemental targets (Ti, Al, and C) at oblique angle, resulting in a columnar thin film, and the properties of the thin film were described as a function of the column tilt angle.

Lastly, the MAX phases at normal configuration and at oblique angle configuration were wet etched and the properties of the resulting MXene thin films were analyzed. It was demonstrated that only the surface of the sample was attacked by the etching solution. Thus, only the surface of the MAX phase was transformed into MXene. This hypothesis was verified by multiple characterizations such as e.g., X-Ray Diffraction and Raman spectroscopy to understand the possible morphology and chemical transformation and its influence on the etched thin film properties.

The aim of this work is to unravel the connection between the morphology of the MAX phase thin films and the properties of the resulting MXenes. By understanding this relationship, it would be possible to tailor their features for specific applications.

# Kurzfassung

MAX-Phasen- Dünnschichten können hergestellt werden, indem zunächst eine Vorläufer-Dünnschicht mit den drei Elementen M, A und X nahe der Stöchiometrie der MAX-Phasen durch physikalische Abscheidung aus der Gasphase abgeschieden wird, gefolgt von einem thermischen Glühprozess.

In dieser Arbeit werden verschiedene Abscheidungskonfigurationen (Multilayer und Co-Sputtern) für die Herstellung von  $Ti_2AlC$  und  $Ti_3AlC_2$ -MAX-Phasen-Dünnschichten durch Magnetron-Sputtern aus drei elementaren Targets (Ti, Al und C) vorgestellt. Es wurde festgestellt, dass die Abscheidungen hauptsächlich amorph erfolgten, so dass sich die MAX-Phase nicht bilden konnte. Durch Einstellen der Abscheidungsparameter wie Temperatur und Substratspannung konnte die Abscheidungsmorphologie auf kristalline beeinflusst werden.

Darüber hinaus wurden  $Ti_2AlC$  and  $Ti_3AlC_2$  nanostrukturierte MAX-Phasen - Dünnschichten durch Magnetronsputtern mit drei elementaren Targets (Ti, Al und C) in einem schrägen Winkel hergestellt (Oblique Angle Deposition), was zu einer säulenförmigen Dünnschicht führte, und die Eigenschaften der Dünnschicht wurden als Funktion des Säulenwinkels beschrieben.

Schließlich wurden die MAX-Phasen in normaler und OAD-Konfiguration geätzt und die Eigenschaften der resultierenden MXen-Dünnschichten analysiert. Es zeigte sich, dass nur die Oberfläche der Probe von der Ätzlösung angegriffen wurde. Somit wurde nur die Oberfläche der MAX-Phase in MXen umgewandelt. Diese Hypothese wurde durch verschiedene Untersuchungen wie Röntgenbeugung und Raman-Spektroskopie verifiziert, um die mögliche Morphologie und chemische Umwandlung und deren Einfluss auf die Eigenschaften der geätzten Dünnschicht zu verstehen.

Ziel dieser Arbeit ist, den Zusammenhang zwischen der Morphologie der MAX-Phasen-Dünnschichten und den Eigenschaften der entstehenden MXene zu entschlüsseln. Durch das Verständnis dieses Zusammenhangs wäre es möglich, die Eigenschaften dieser Schichten für bestimmte Anwendungen zu optimieren.

# 1 Introduction

MAX phases are an innovative class of materials with laminated structure that follow the general formula  $M_{n+1}AX_n$  where M is an early transition metal, A is an A-group element (element of group III A or IV A), and X is either carbon C or nitrogen N. These nanolaminated ternary nitrides or carbides are divided into three categories depending on the value of  $n$ : 211 ( $n=1$ ), 312 ( $n=2$ ), and 413 ( $n=3$ ), e.g.,  $Ti_2AlC$ ,  $Ti_3AlC_2$  and  $Ti_4AlC_3$ , whereas in this case the last one are not thermodynamically stable [36]. Regardless of the group they belong to, all MAX phases exhibit an hexagonal structure, where the transition metal atoms M and the carbon or nitrogen atoms X form octahedral edge sharing building (MX) blocks interleaved by pure A-element layers [42]. The index  $n$  refers to the number of M layers separating the A layers, located at the center of trigonal prisms, as Figure 1.1 shows.

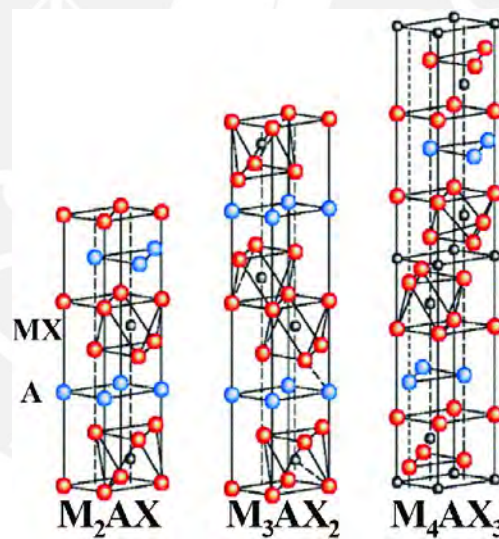


Figure 1.1 Hexagonal crystal structure of the  $M_{n+1}AX_n$  phases depending on the index  $n$  ( $n = 1, 2, 3$ ) [42]

Due to the mixed metallic-covalent nature of the M-X bond, which is considered exceptionally strong, and the nano-laminal crystal structure, MAX phases' combination of properties fulfill the gap between ceramics and metals. Similar to ceramics, these materials exhibit high mechanical stability, high temperature strength, low density, small thermal expansion coefficient and high hardness, but also good electrical and thermal conductivity simultaneously, properties attributed commonly to metals [30]. Various applications take advantage of their remarkable combination of the physical,

electrical, and mechanical properties, such as high temperature components, e.g., protective coating [25], as well as bond-coats for gas turbines as joining material [36], electrical contacts, and catalyst [19].

Upon the 150 MAX phases [36] explored in the last years, the most well-known is  $\text{Ti}_2\text{AlC}$  due to the outstanding corrosion resistance and high irradiation damage resistance, which make this MAX phase a perfect candidate for applications as a protective coating [93]. Of the various deposition for the MAX phases techniques, such as pulsed laser deposition or plasma spraying, a well-extended method for the fabrication of thin films is the deposition by magnetron sputtering (MS) [62]. MS is a high-rate vacuum coating technique for depositing metals, alloys, and compounds onto a wide range of materials with thicknesses up to millimeters [11]. MAX phase thin films can be fabricated through firstly depositing a precursor thin film consisting of the initial elements M, A, and X close to the MAX phase stoichiometry employing physical vapor deposition techniques with a subsequent thermal annealing process [30]. Thin films fabricated by MS are normally deposited on substrates placed perpendicular to the material flux and thus parallel to the target, resulting in compact thin films. In contrast to the normal configuration of the substrate with respect to the vapor flux, they can be placed at oblique angles (oblique angle deposition: OAD), also known as off-normal configuration, to fabricate porous thin films in the shape of separated and tilted nanocolumns, as Figure 1.2 shows. As a result, the morphology and therefore properties of the thin film can be tailored.

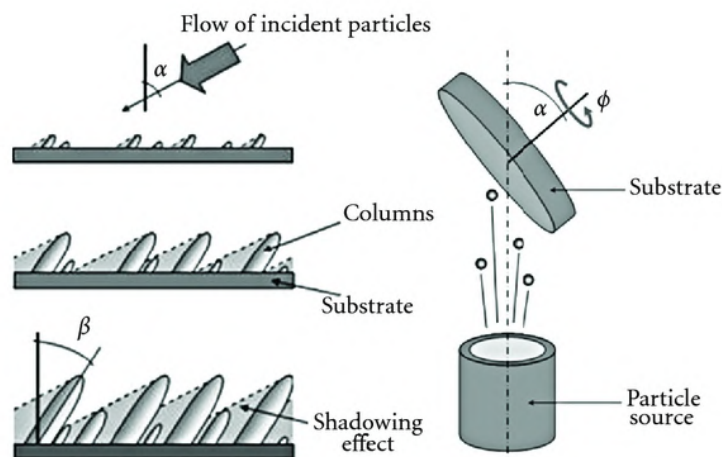


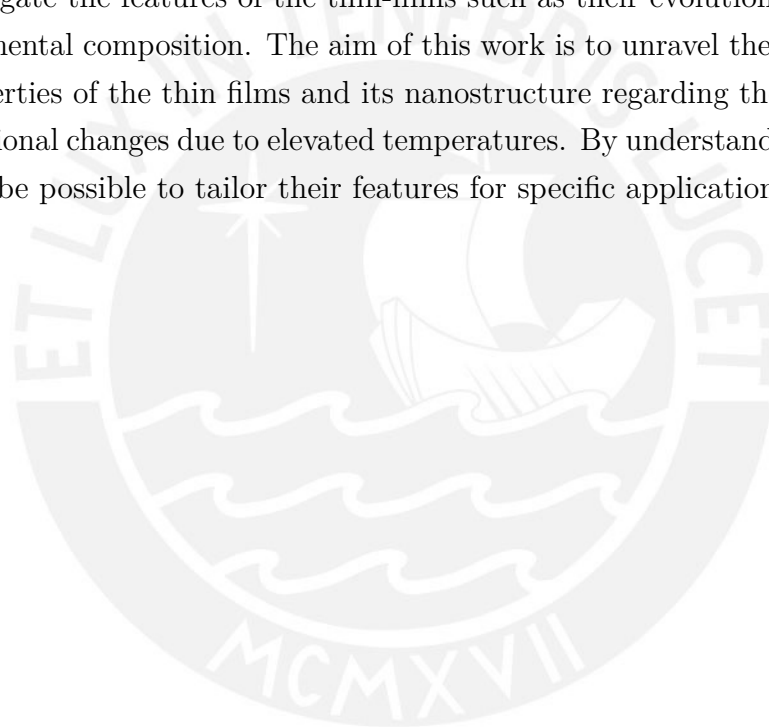
Figure 1.2 Principles of oblique angle deposition (OAD) [14]

Furthermore, the three-dimensional MAX phases have been extensively studied in the last years as precursors of the two-dimensional materials MXene [70] by simply selective



etching with hydrofluoric acid (HF) the A-atom of the MAX structure. These two-dimensional early transition metal carbides and/or nitrides are considered an important class of materials due to their exceptional electronic, optical and mechanical properties [43], inherited from MAX phases, and find a place in the industry as membranes [24], catalysts [59], and sensors [112].

This work presents a methodology for the deposition of Ti-Al-C MAX phases via magnetron sputtering with a subsequent annealing using rapid thermal processing (RTP), as well as the influence of the deposition angle on the formation and the properties of the MAX phases. Furthermore, the properties of the resulting MXenes will be analyzed according to the MAX phase precursors. Several characterizations were used to investigate the features of the thin-films such as their evolution in morphology and their elemental composition. The aim of this work is to unravel the connection between the properties of the thin films and its nanostructure regarding the morphological and compositional changes due to elevated temperatures. By understanding this relationship, it would be possible to tailor their features for specific applications.



## 2 Experimental Methods

### 2.1 Magnetron Sputtering MS

Thin film vapor deposition methods are separated into two principal categories: Chemical Vapor Deposition (CVD) and Physical Vapor Deposition (PVD). In CVD, the deposition takes place by using thermally induced chemical reactions at the surface of the substrate. On the other hand, PVD techniques use physical means to deposit a thin layer. Firstly, a solid precursor becomes gaseous and their liberated atoms are directed in a vacuum chamber towards a substrate. Atoms originating from the material source condense on the substrate, forming a thin film [11]. Among the most used PVD methods, there is the deposition by thermal evaporation and by sputtering [102]. In the thermal evaporation, the source of material evaporates due to higher temperature in a vacuum chamber and condenses the particles on a substrate, whereas in the sputtering, the deposition results from atoms or molecules eroded from a solid target by the impact of ions. Among the advantages of magnetron sputtering (MS) stand out an easy control of the deposition rates, large coating area, and strong adhesion to the substrate [85]. It also allows the deposition of a wide range of materials at relatively high purity and low cost. In MS, a plasma of positive charged argon ( $\text{Ar}^+$ ) ions is created in the deposition chamber, where they are accelerated towards the negatively charged target (cathode) to strike out atoms or molecules from it, as Figure 2.1 shows.

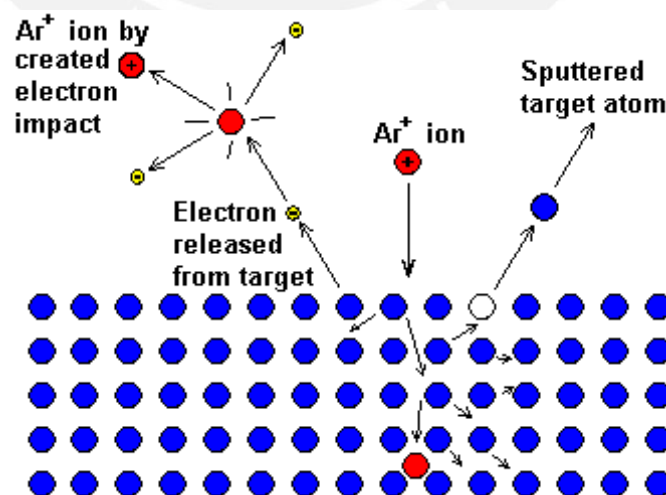


Figure 2.1 Schematic of the target surface processes during the magnetron sputtering deposition [10]

Because Argon is an inert gas, the sputtering ions do not interfere with the deposition (passive sputtering). The eroded atoms from the target are condensed on the substrate growing a thin film. The ion impact leads to the emission of secondary electrons from the target surface, which helps to sustain the plasma.

On the other hand, in reactive sputtering, a reactive gas like Nitrogen ( $N_2$ ) chemically reacts with the sputtered particles and is deposited on the substrate. There are two types of MS: direct current (DC) MS and radio frequency (RF) MS, as Figure 2.2 shows.

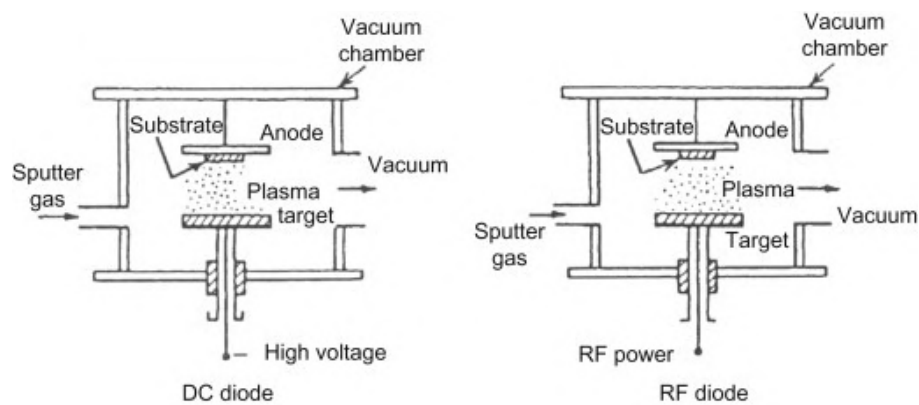


Figure 2.2 Schematic principle of magnetron sputtering by a) direct current (DC) and b) radio frequency (RF) [2]

While in DC sputtering the source of power is direct current, RF sputtering applies alternative current (frequency of about 13.56 MHz). The RF sputtering consists of two steps. In the first step, the target is negatively charged, pulling the argon gas ions towards the target surface, and eroding atoms from the source (similar to the DC sputtering). The eroded ions remain in the surface of the target due to its polarization and, in the second step, the target changes its polarization to positive accelerate the atoms towards the substrate, which deposit forming the thin film. In RF magnetron sputtering the target material does not present the limitation present in DC magnetron sputtering, meaning that it does not require to be electrically conductive. This allows theoretically any material to be deposited by RF magnetron sputtering. Since various deposition configurations were employed in this work, the individual deposition parameters of the samples are explained in the subsequent sections of this thesis.

Figure 2.3 shows the schematic diagram of magnetron sputtering system installed in the Physics Section at PUCP that was employed for a section of the deposition experiments, where the Ti-Al-C elemental targets can be observed. The magnetrons were facing the substrate holder and were positioned to guarantee a homogeneous

composition in the center of the sample, while the substrate holder rotates.

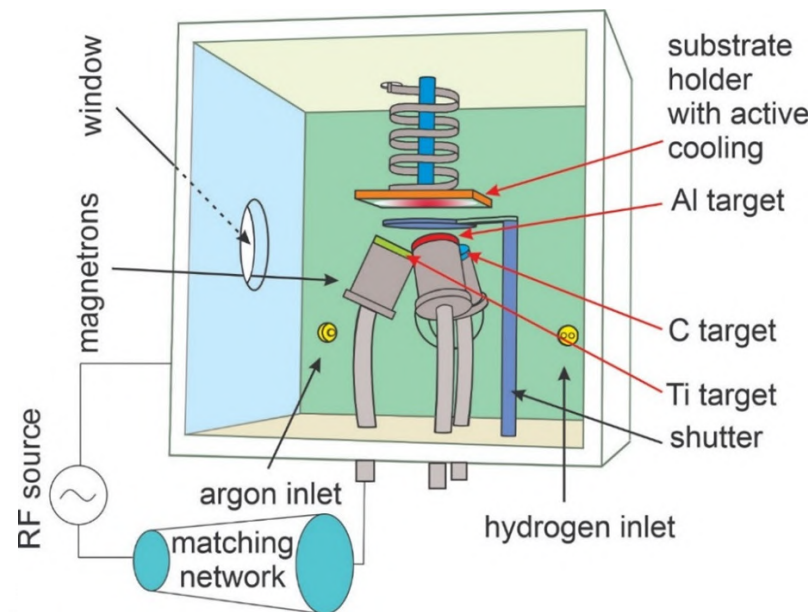


Figure 2.3 Schematic of the RF magnetron sputtering system of titanium, aluminium and carbon installed in the Physics Section at Pontificia Universidad Católica del Perú and employed in this work [72]

## 2.2 Rapid Thermal Annealing RTP

Rapid Thermal Processing (RTP) is a technology extensively exploited in the microelectronics industry for annealing, thermal oxidation and reducing the thermal redistribution of impurities [3] among other uses. In this process, a wafer is heated to temperatures over 1000 °C in a matter of seconds. Then, in a timescale of several seconds or less, the wafer is cooled down. This short exposure to high temperatures is often sufficient to achieve the desired objective of annealing without damaging the substrate or any other temperature-sensitive parts of the wafer. Figure 2.4 shows a schematical set-up of the RTP chamber.

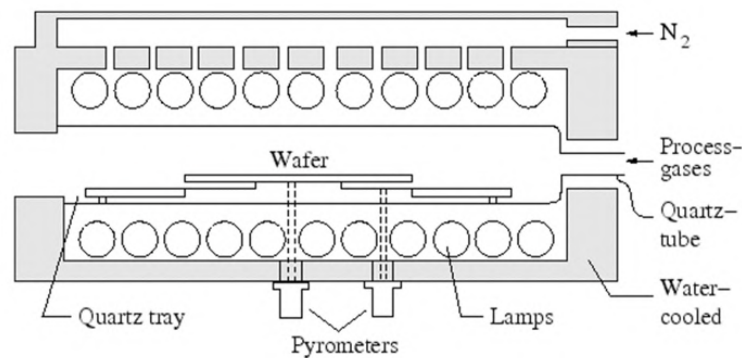


Figure 2.4 Rapid Thermal Annealing (RTP) system configuration [3]

In the first step, the wafer is introduced in the RTP chamber. To prevent the oxidation of the sample, a vacuum of around  $1 \times 10^{-5}$  mbar must be established. Then, a flow of inert gas, usually  $N_2$  or Ar, must be programmed. The rapid heating rates (20-200 °C/sec) [26] are reached by employing high intensity lamps or lasers, which measure the sample temperature and consist generally of pyrometers and thermocouples.

For this work, the samples produced in the TU Ilmenau were annealed in a RTP (Jet First, Joint Industrial Processors for Electronics) under an argon inert atmosphere. Two temperatures were set to complete the MAX phase transformations: 700 °C and 900 °C. The heating and cooling rates were held constant for all experiments at 10 K/s and 5 K/s respectively and the argon flow was set to 600 sccm.

For the samples produced in the PUCP, an oven Nabertherm B400 was employed as an alternative to the RTP oven. This tubular alumina oven also has the possibility to heat the sample under vacuum and under inert atmosphere, thus the oxidation of the samples is prevented. In contrast to the RTP equipment, the heating and cooling could not be achieved at high rates due to equipment limitations, and was established at 0.08 K/s. The pressure of the oven was set to  $4 \times 10^{-4}$  mbar with the help of a turbomolecular and a mechanical pump, and the argon flow was set to 600 sccm.

## 2.3 Raman Spectroscopy

Raman spectroscopy is a non-destructive spectroscopic analysis technique based on the inelastic interaction of light with the chemical bonds within a material [104], also known as the Raman effect. This analysis technique is used for the determination of molecular interactions and provides information about its structural fingerprint [32], phase and crystallinity [104]. Figure 2.5 shows the three types of scattering processes that occur when monochromatic light interacts with a molecule.

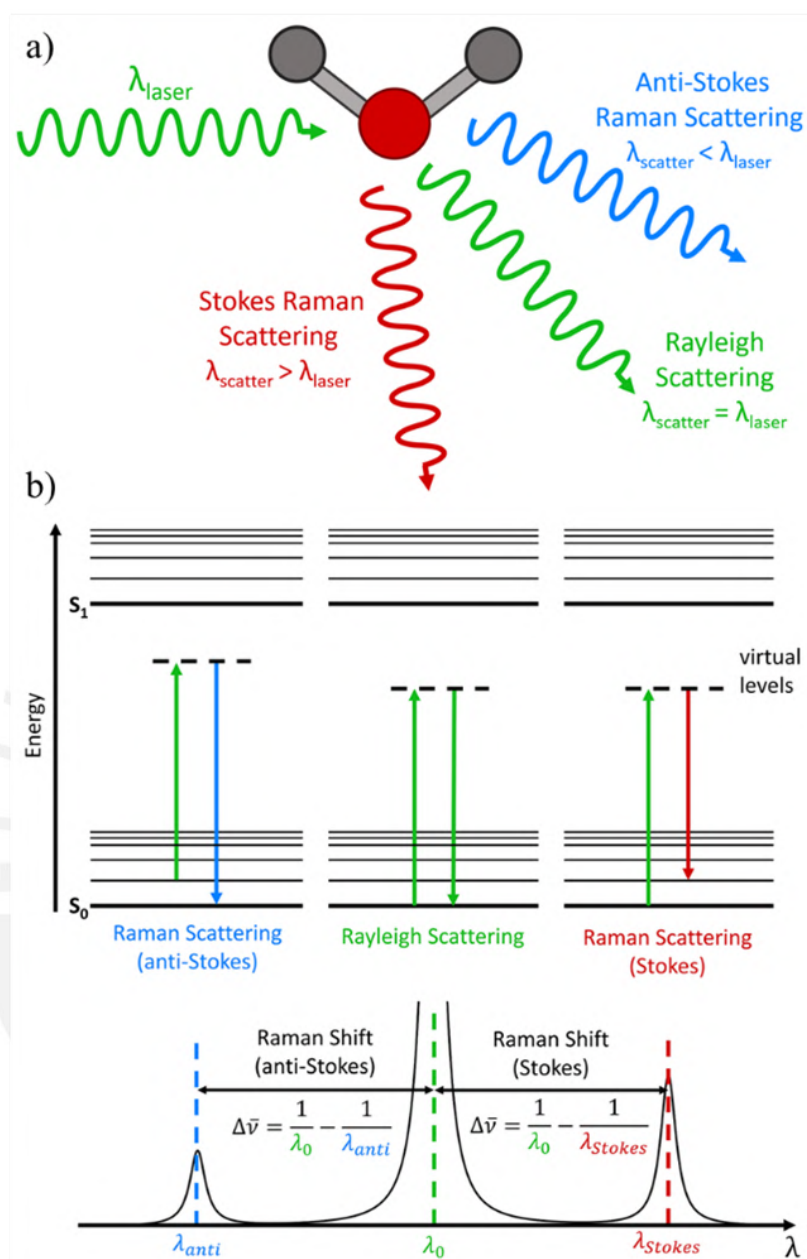


Figure 2.5 a) Types of scattering processes that occur when monochromatic light interacts with a molecule; b) Electronic transitions and its resulting spectra (Reprinted from Reference [104])

A source of monochromatic light from a laser ( $h\nu_i$ ) interacts with the molecular bond, also seen as molecular vibrations. The incident photon leads to the excitation of electrons, which move into the higher energy positions i.e., the virtual state, for a short time. After, the electrons fall back into lower energetic levels and a photon is emitted. The dominant process of the scattering events is called the Rayleigh Scattering. During this elastic interaction, both the energy of the molecule and the energy of the incident

photon, and therefore its wavelength, remain unchanged ( $\lambda_{\text{scatter}} = \lambda_{\text{laser}}$ ). Because this scattering does not provide information about the analyzed material, the Rayleigh Scattering is filtered out, while the rest of the signal is collected onto the detector.

A small amount of the monochromatic light [27] transfers energy by exhibiting an inelastic scattering process between the analyzed molecule and the scattered photon. This inelastic scattering depends on the chemical structure of the analyzed material and is called the Raman Scatter. If the molecule energy increases its energy during the this process by getting excited to a higher vibrational level, the scattered photon loses energy i.e., its wavelength increases ( $\lambda_{\text{scatter}} < \lambda_{\text{laser}}$ ). This process is called the Stokes Raman Scattering. Conversely, if the molecule reduces its energy by relaxing to a lower vibrational level, the energy of the scattered photon increases and therefore its wavelength decreases ( $\lambda_{\text{scatter}} > \lambda_{\text{laser}}$ ). Following the same nomenclature, this process is called the Anti-Stokes Raman Scattering. The resultant radiation is amplified and plotted as intensity against the wavelength.

Figure 2.6 shows the main components of a Raman microscope system, which can be divide into two main elements: the sample chamber, where the excitation source and the sample are located, and the spectrometer that contains the detection and computer control, as well as the processing systems.

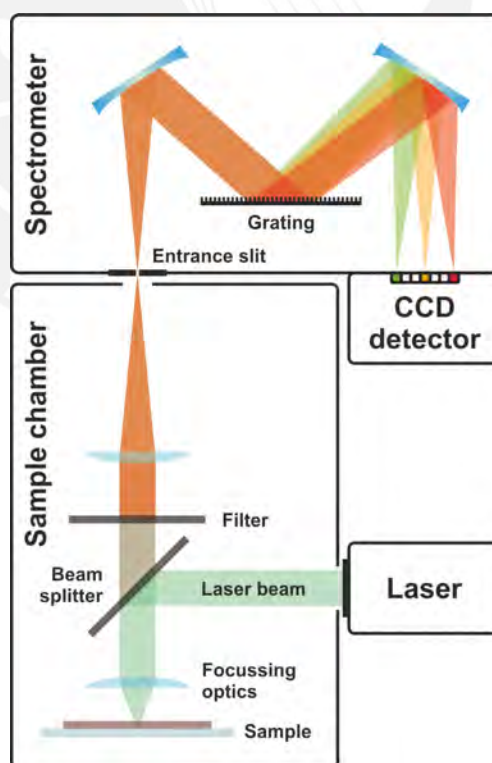


Figure 2.6 Schematic principle of Raman spectrometer setup [81]

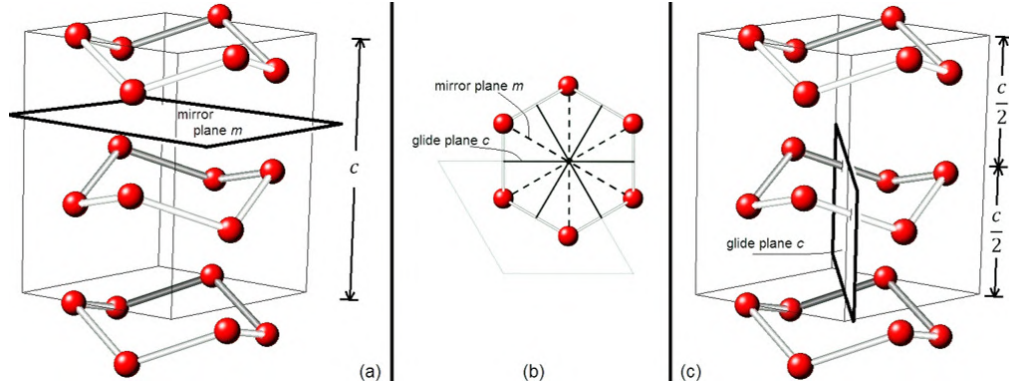


Lasers are the most appropriate excitation sources for this characterization technique due to their highly monochromatic beams, small radiant flux, and linear polarization [50] since the resolution of the Raman spectrum is mostly determined by the laser's bandwidth. A series of focusing and collection optics are necessary to excite and collect from the sample. The collection optics consist of achromatic lenses, which include collecting and focusing lenses, to collect the scattered light and focus it on the entrance aperture. One of the main challenges that present this analysis method is the difficulty to separate the inelastically scattered spectrum (Raman spectra) from the elastically scattered (Rayleigh spectra). Therefore, a filter must be applied to separate both the Rayleigh and the Raman spectrum. In the spectrometer, the scattered photons are separated by wavelength before they are transmitted to a collector. A so-called charge-coupled device (CCD) detector recollects the number of photons, and therefore the intensity, and plots its wavelength against the number of counts to recreate the Raman spectrum, which would be analyzed afterwards. The only spectrum that is analyzed is the Stokes signal, since the anti-Stokes spectrum has precisely the identical pattern but its intensity is much weaker. Typically, the Raman spectra are represented in a diagram, where the Raman shift (in  $\text{cm}^{-1}$ ) is plotted on the horizontal axis and the intensity (in counts) on the vertical axis. The Raman spectrum includes numerous peaks, which considering their position and intensity, correspond to a specific molecular bond vibration. This chemical fingerprint can be used to identify the analyzed material by comparing it with a Raman spectral library, where it is contrasted with numerous spectra in order to find a match and, thus provide a chemical identification [104]. The observed wavelength is case-dependent and goes typically from  $100 \text{ cm}^{-1}$  until  $3000 \text{ cm}^{-1}$ . Depending on the expected spectrum of the sample, different regions are analyzed. For example, the region below  $1500 \text{ cm}^{-1}$  is characteristic for complex pattern of carbon-carbon or nitrogen-carbon vibrations is generally referred to as the Fingerprint region. Vibrational modes found below  $650 \text{ cm}^{-1}$  are explained by the presence of inorganic compounds, metal-organic compounds, or lattice vibrations [29].

The hexagonal structure from all MAX phases belong to the space group  $P63/mmc$  [76]. In line with the international symbol notation system, the first symbol ( $6$  in this case) denotes the symmetry along the major axis, the second ( $3$ ) along axes of secondary importance. Following the explanation, the first  $m$  indicates the mirror plane perpendicular to the  $c$ -axis (as Figure 2.7a shows), the second  $m$  indicates the mirror planes parallel to the  $c$ -axis (Figure 2.7b), and the  $c$  indicates the glide planes (Figure 2.7c) [41].

When taking a closer look at the  $\text{Ti}_2\text{AlC}$  MAX phases, a total of 4 modes out of the




 Figure 2.7 Crystal structure of  $P63/mmc$  space [105]

initial 24 modes known in this phase are Raman active, of which three ( $A_{1g} + 2E_{2g}$ ) are only Raman active modes [56]. When observing the  $Ti_3AlC_2$  MAX phases, seven Raman active modes ( $2A_{1g} + 2E_{1g} + 3E_{2g}$ ) can be identified.

Figure 2.8 shows a schematic representation of the atomic vibrational modes corresponding to the Raman active modes for both 211 and 312 MAX phases.

The literature values of the individual vibrational modes in the MAX phases are shown in Table 2.1 and Table 2.2

 Table 2.1 Raman shift ( $cm^{-1}$ ) of the Raman mode of the 211 MAX phases

$\omega_1[E_{2g}]$	$\omega_2[E_{2g}]$	$\omega_3[E_{1g}]$	$\omega_4[E_{2g}]$	Comments
153.3	260	270.3	358.7	Experimental from Reference [76]
149.9	262.1	268.1	365.1	Experimental from Reference [88]
149	262	248	387	Calculated from Reference [88]
151	256	270	366	Calculated from Reference [56]
146	265	266	365	Calculated from Reference [76]

 Table 2.2 Raman shift ( $cm^{-1}$ ) of the Raman mode of the 312 MAX phases

$\omega_1[E_{2g}]$	$\omega_2[E_{1g}]$	$\omega_3[E_{2g}]$	$\omega_4[A_{1g}]$	$\omega_5[E_{1g} \text{ and } E_{2g}]$	$\omega_6[A_{1g}]$	Comments
/	183.4	201.5	270.2	632.2	663.2	Exp. from Ref.[76]
125	182	197	268	620 and 621	655	Calc. from Ref.[76]

$Ti_3C_2$ , as well as its precursor  $Ti_3AlC_2$ , belongs to the group  $D3d$  [80]. Their vibrational modes are described as:  $4E_g + 2A_{1g} + 4E_u + 2A_{2u}$ , where  $E_g$  and  $A_{1g}$  correspond to Raman active modes. The  $E_g$  correspond to an in-plane vibration of Ti and C atoms and  $A_{1g}$  to the out-of-plane vibration of Ti and C atoms [73].

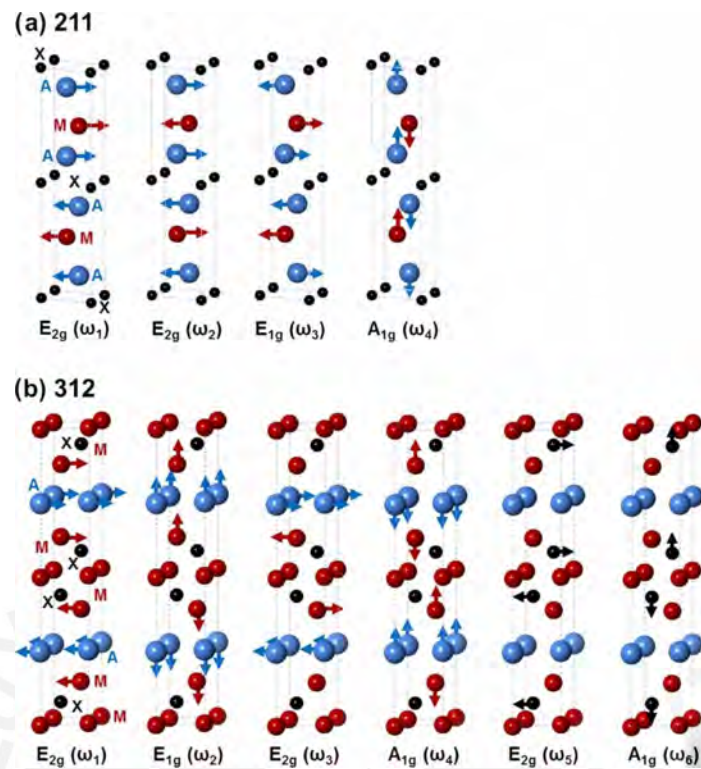


Figure 2.8 Schematic representation of the vibrational modes of MAX phases depending on its stoichiometry a) 211 and b) 312 [76]

When surface groups (-O, -F) are added e.g., by selective etching, the total amount of atoms in the unit cell increases, therefore the number of vibrations increases accordingly. Therefore, the unit cell, in which the surface terminations were added, distorts. The labelling to the  $D3d$  group is not accurate because of the intercalation and adsorption of surface terminations, which affect the lattice vibrations and distort the crystalline structure. This unit cell alteration result in peak shifting and broadening. For this concrete example, Hsiu-Wen et al. (2016) refer to the resulting lattice as “*pseudo-P63/mmc*” [101].

To analyze the structural properties of the MAX phases as well as the resulting MXenes, a confocal Raman spectrometer (inVia<sup>TM</sup> by Renishaw) equipped with a frequency doubled helium-neon laser ( $\lambda_{\text{exc}} = 633 \text{ nm}$ ) with an average power density of  $7.72 \text{ mW/cm}^2$  and a 100x objective was used. The spectrometer was also equipped with a 1200 grooves/mm diffraction grating and the Raman spectra were collected at ambient temperatures and analyze using the data analysis program WiRE.

## 2.4 X-Ray Diffraction XRD

X-ray diffraction (XRD) is a non-destructive analysis technique used for the identification of the crystallinity of materials. By means of XRD analysis it is possible to deliver information about unit cell dimensions, phases, average grain size and crystal defects [18]. This method allows to determine d-spacing of a crystalline material with a high accuracy. XRD is based on the constructive interference of monochromatic X-rays when they interact with a crystalline sample. X-rays from the source are lead towards the sample and if Brags law is fulfilled (Equation 2.1).

$$2d \sin \theta = n \lambda \quad (2.1)$$

where  $d$  describes the interplanar distance,  $n$  is a positive cipher,  $\lambda$  is the wavelength of the incident monochromatic X-rays, and  $\theta$  the angle formed between the incoming X-ray and the interplanar distance  $d$ . Figure 2.9 shows the geometrical relation between these parameters.

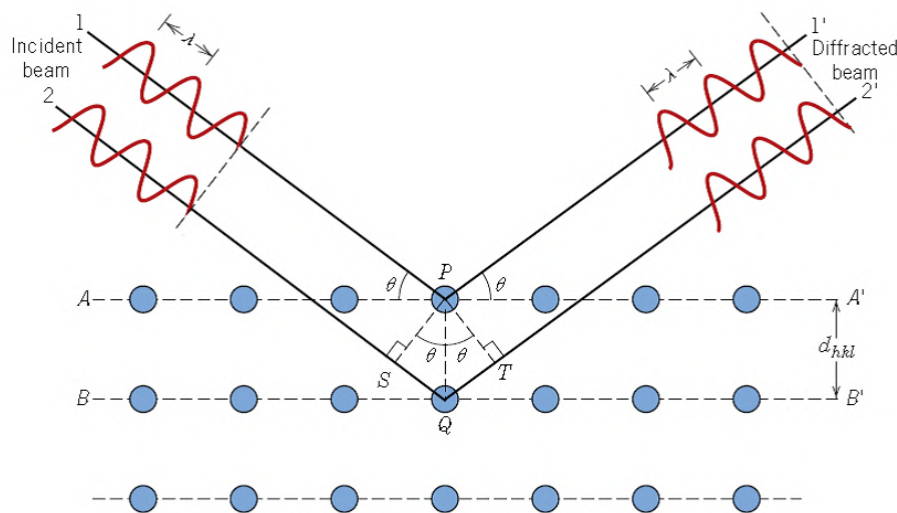


Figure 2.9 Constructive interference described by Bragg's law [107]

Using Bragg's law, the angle where constructive interference from X-rays scattered by parallel planes produce a diffraction reflex is measured, and therefore the interplanar distance is calculated. A crystalline plane causes a diffraction reflex at a specific angle  $2\theta$ . By scanning the sample through a range of  $2\theta$  angles, all diffraction peaks are recorded. The position and intensity of these peaks are determined by the composition and crystalline phase of the material. Therefore, from the XRD diffractogram, it

is possible to conclude the interplanar distance  $d_{hkl}$ . The interplanar distance gives information about the average spacings between the crystalline layers, as well as the orientation of small crystalline regions.

Two configurations can be differentiated to obtain the XRD diffractogram of a material, Bragg Brentano (BB) and Grazing Incidence (GI) XRD as Figure 2.10 exhibits.

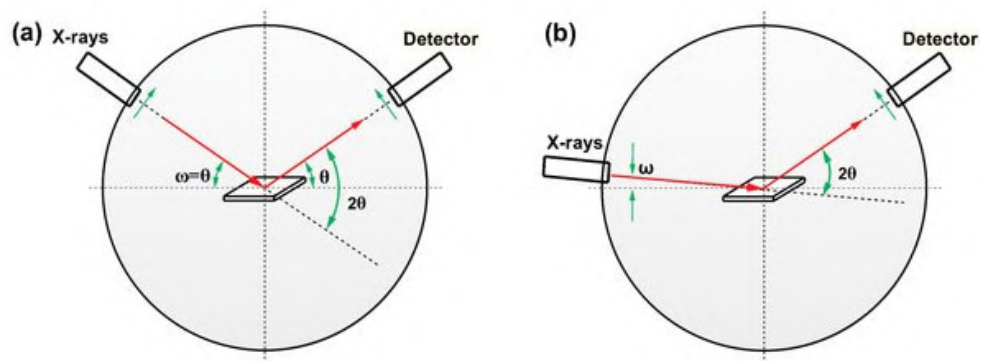


Figure 2.10 Schematic representation of X-Ray diffraction (XRD) a) in Bragg-Brentano configuration, where both the X-Ray source and the detector move, and b) in grazing incidence configurations, where only the detector is able to move [23]

In the Bragg-Brentano configuration, shown in Figure 2.10a), both the X-ray source and the detector change their position and decide the incident angle ( $\omega$ ), defined between the X-ray source and the sample. The diffraction angle ( $2\theta$ ) is defined between the incident beam and the detector, and is two times the incident angle. In this configuration, the incidence angle equals the angle of the diffracted beam with respect to the inspected sample surface. This configuration produces weak signals from the thin films and more signals from the substrate. Since both the X-ray source and the detector move, the depth of analysis varies during the measurement. In the Bragg Brentano configuration, the atomic planes which are parallel to the surface orientation fulfill Bragg's equation and show a reflex.

In XRD at grazing angle configuration, shown in Figure 2.10b) the X-ray source remains unmoved, where the incidence angle is fixed at a relatively small angle (commonly between  $1^\circ$  and  $3^\circ$ ), which exceeds the critical angle of total reflection. The angle between the incident beam and the diffracted beam varies by rotating the detector. With decreasing incident angle, the depth of analysis decreases. The depth of the analysis is set by the X-ray incident angle and it is independent from the  $\theta$  angle, therefore it remains constant during the measurement. Because of this variation of the analysis depth, this configuration is commonly used for analysis and characterization of thin films. The main components of a diffractometer are shown in Figure 2.11.

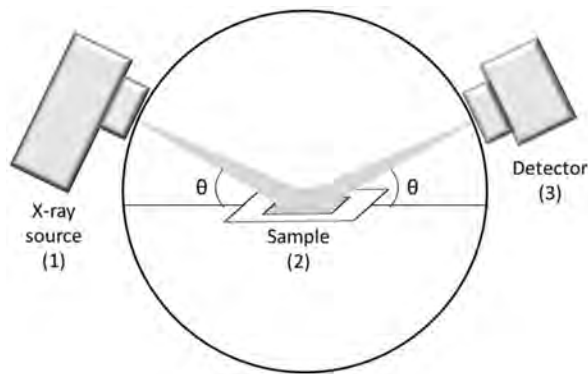


Figure 2.11 Schematical setup of a diffractometer [98]

The measuring process goes as follows: firstly, the X-ray source (1) produces the X-rays which irradiate the sample (2) at a defined angle. Then, when the Bragg's law is fulfilled, a characteristic reflex is created. The detector (3) records the scattered X-rays and a diffraction pattern is imaged.

When conducting a diffraction experiment, the main goal is primarily to obtain more information about the microstructure of the sample. Figure 2.12 shows the obtainable and derivable information from a diffraction experiment as well as further correlations between the gained values.

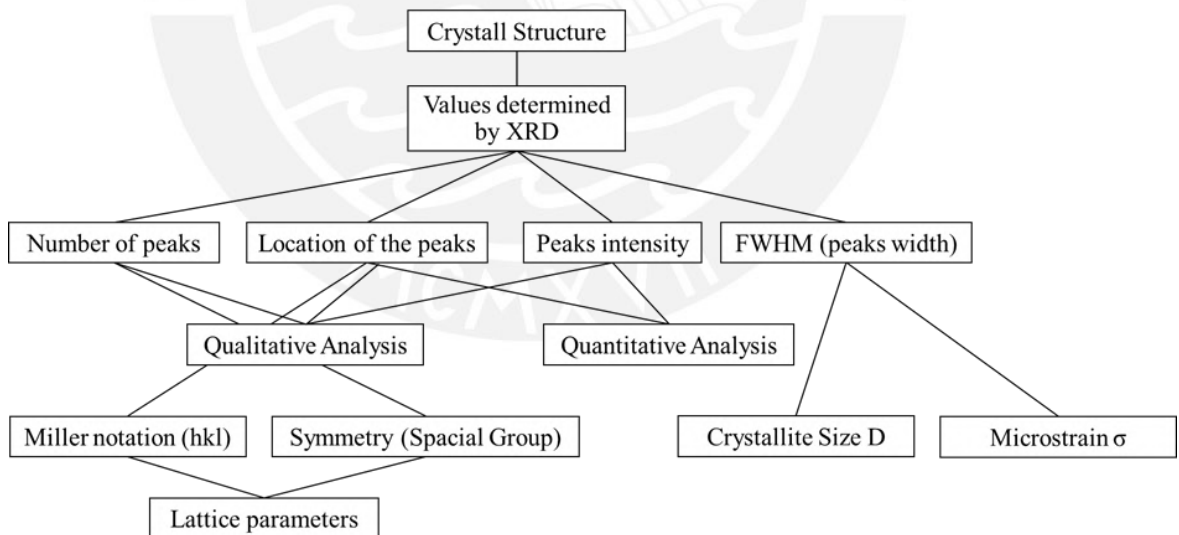


Figure 2.12 Information obtainable and derivable from diffraction experiments (Reprinted from Reference [89])

The first step to understand the diffraction pattern would be to differentiate between amorphous and crystalline samples. If single and very sharp diffraction interferences occur, a single crystal can be present and the crystal system can be determined. On

the other hand, if no diffraction interferences occur, there are no diffractive network planes within the penetration range of the radiation and an X-ray amorphous sample can be present.

The determination of the crystalline phase in a sample is referred to as qualitative phase analysis. This is called the “fingerprint method” because different crystal structures of all elements and compounds are associated to characteristic diffraction patterns, which have been extensively studied and documented. Therefore, by comparing the measured diffraction pattern with the documented pattern, a correlation can be established and an unknown sample can be identified. This relies on the fact that each individual diffraction interference can - more or less difficult - be assigned to a net plane ( $hkl$ ). Important information can be obtained by analyzing the number, location, and intensity of the peaks. The determination of the cell parameters, the atomic distribution and the symmetry in the atomic order is called crystal structure analysis.

Additionally, the full width at half maximum ( $FWHM$ ) calculation broadens the information obtained from a diffractogram. The difference between the right-hand angle and the left-hand angle at half the net is called half width  $HB$ ,  $HWB$  or  $FWHM$ , and in many cases is assumed to be the width of the diffraction peak. Real diffraction interferences often have an asymmetrical course and offshoots, in which further physical information is contained. From the area of under the peak, a rectangle with the same area and the height is formed. The width of this rectangle is the integral width  $IW$ . Employing this  $FWHM$  value, the crystallite size  $D_{hkl}$  and microstrains can be calculated. This determination of particle sizes is also part of the quantitative analysis. For this goal, the relationship between  $FWHM$  and the crystallite size, also known as Scherrer equation [45] (Equation 2.2)

$$D_{hkl} = \frac{K\lambda}{FWHM \cos \theta_{hkl}} \quad (2.2)$$

where  $K$  is a constant called shape factor, whose values can vary from 0.89 to 1.39 [45], and takes into consideration the crystallite shape e.g., for spherical crystallites the value is set to 0.94. However, since the shape of the crystallite is unknown, an approximation of  $K = 0.89$  is generally accepted [89] and used.  $\lambda$  is the wavelength of the monochromatic radiation and  $\theta_{(hkl)}$  is the diffraction angle of the interference peak.

In this work, X-ray diffraction analysis was conducted to characterize the crystallinity of the as-deposited and vacuum-annealed thin films using a Bruker D8 diffractometer with  $\text{CuK}_\alpha$  radiation source ( $\lambda_{\text{Cu}} = 1.54 \text{ \AA}$ ) with an acceleration voltage of 40 kV and



a filament current of 40 mA using Bragg Brentano (BB) and Grazing Incidence (GI) configurations. The classical  $\theta$ - $2\theta$  diffraction experiment was performed in the range of 5 to 80° with a scan speed of 3 s/° and a step size of 0.02°. In the GI measurements, the angle  $\theta$  was held constant at 2° and a Goebel mirror was necessary to parallelize the incident beam.

## 2.5 Scanning Electron Microscopy SEM and Energy Dispersive X-Ray EDX

The Energy Dispersive X-ray (EDX) is a technique of elemental analysis based on the emission of characteristic X-rays generated when high-energy electrons bombard a sample revealing its chemical composition [51] [82]. Figure 2.13 shows its schematical principle.

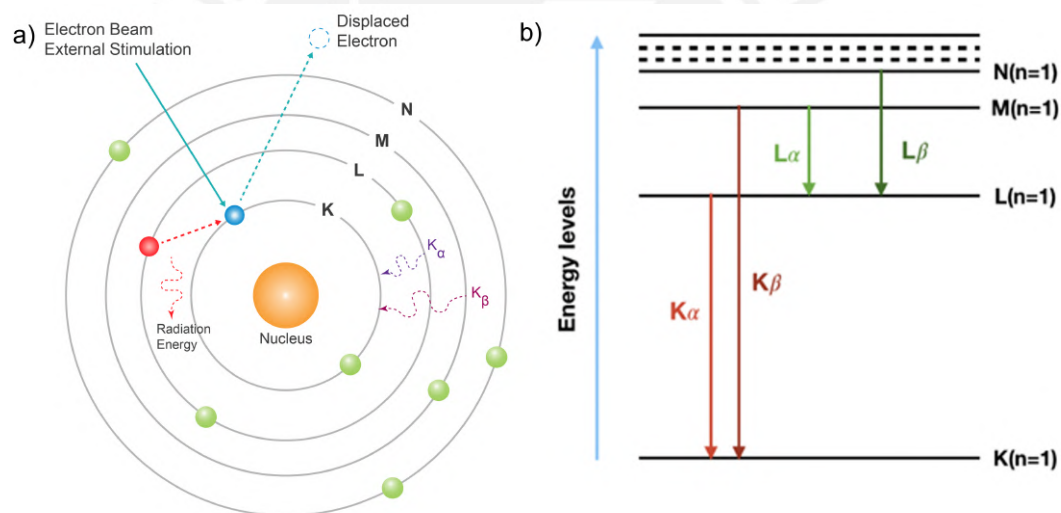


Figure 2.13 a) Schematic representation of EDX principle [49]; b) Possible electron transitions and their atomic orbital notation [54]

The displacement of an electron in the inner shell of the atom because of a collision with a (primary) external electron, causes the creation of an ion in an excited state. An electron from the outer shell falls into the vacancy to reestablish the charge balance and the ion returns to its ground state by emitting an X-Ray photon. Because each element has a unique energy difference between the outer and inner electron, the detected radiation allows an identification of the element. In the notation for the characteristic X-rays, the principal quantum number  $n = 1, 2, 3, 4$  is denoted by a letter K, L, M, N. The radiation energy is named according to the shell in which the displaced electron is

expelled, followed by an index that indicated the shell from which an electron drops to fill that vacancy [16]. Figure 2.13 shows a few examples of such notation.

An EDX system is placed typically in a scanning electron microscope (SEM), as Figure 2.14b) shows. When the focused electron beam from the source interacts with the surface, multiple signals are released as a result of the change of the kinetic energy of the electrons within the sample.

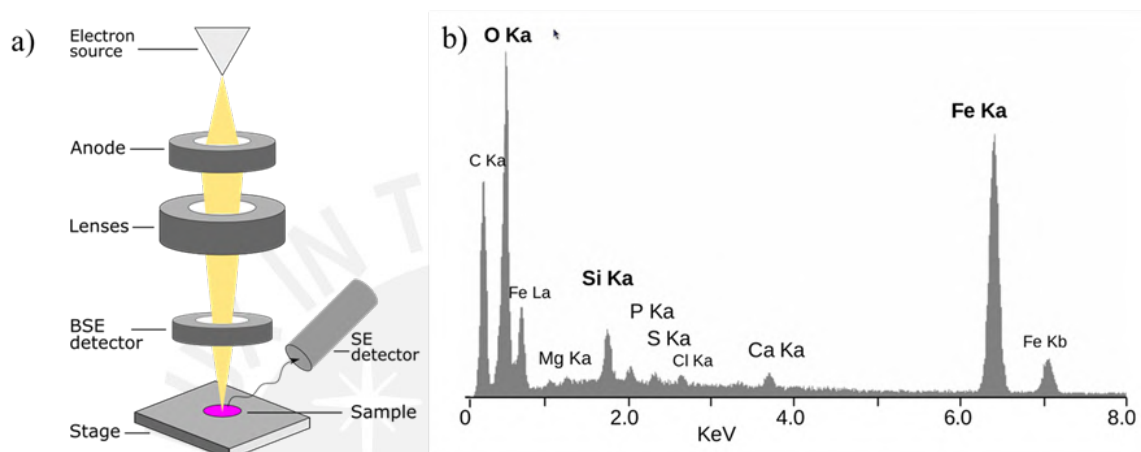


Figure 2.14 a) SEM functional principle [8]; b) EDX spectrum [21]

This analysis method implies some limitations in elemental analysis. Firstly, it is only possible to detect those elements with atomic number larger than  $Z = 10$  with a minimal elemental concentration of 10 ppm [1] since an inferior amount of characteristic X-ray signals are generated by light elements since they present less orbiting electrons, whereas spatial resolution ranges from about 10 nm to a few micrometers. For light elements (minimum detection limits  $< 1\%$ ), the relative precision decreases from  $\sim 4\%$  to  $2\%$ .

To unravel the elemental composition of the samples, an EDAX Octane Pro EDX detector mounted on a scanning electron microscope FEI Quanta 650 was used. The acceleration voltage was set to 5 kV in order to guarantee the detection of lighter elements such as carbon and oxygen, which adds valuable information to the analysis of the samples. By correctly choosing the acceleration voltage of the electron beam, the penetration depth in the sample decreased. Since the thin film thickness is  $\sim 500$  nm, by analyzing the sample with 5 kV the penetration depth corresponds to  $\sim 350$  nm, ignoring the substrate and analyzing solely the thin film. Different magnifications (15kx, 30kx and 50kx) were employed to display the details of the surface depending on the desired point.



## 2.6 4-point probes method

The main purpose for this analysis is to measure the electrical properties of the thin film and, by comparing the theoretical and experimental values, identify the resulting thin film after the selective etching. In order to do so, four electrical probes or electrodes are positioned touching the sample surface in a square configuration, as Figure 2.15 shows.

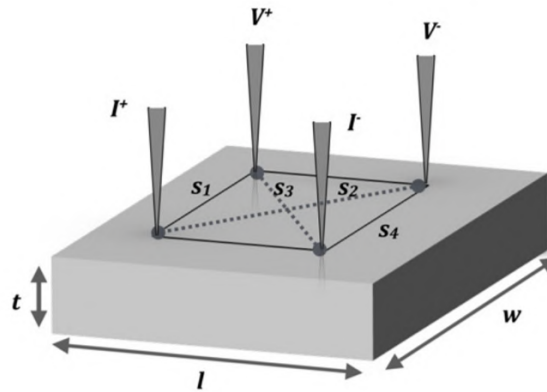


Figure 2.15 Schematic of a square 4P probe configuration where the space between the contacts can be described with  $s_1 = s_4 = s$  and  $s_3 = s_2 = \sqrt{2}s$  [67]

The main advantage of this method over the linear 4P array, where the electrical contacts are arranged forming a straight line, is the slightly higher sensitivity of the measurement. During the measurement, a constant electric current  $I$  passes through the outer probes inducing a voltage drop  $\Delta V$  in the inner probes. Resistivity is determined using Equation 2.3

$$\rho = \frac{2\pi V}{\ln 2 I} \quad (2.3)$$

For the characterization of the electrical properties of the thin films, a current  $I = \pm 1$  mA was applied, measuring the voltage in steps of 0.1 mA at room temperature.

## 2.7 Variable Angle Spectroscopic Ellipsometry VASE

Spectroscopic Ellipsometry (SE) is an effective, well-established, non-destructive characterization technique which allows the determination of several thin film properties simultaneously. Depending on the optical properties of the analyzed material, spectroscopic ellipsometry can measure thickness from a few Å to tens of microns [69]: The penetration depth of the light in the material depends on its absorption coefficient ( $\alpha$ ). In opaque materials e.g., metal thin films with a thickness higher than 50 nm [74],

this characterization technique only determines optical properties of the sample and a thickness measurement is not possible. This result is explained by the reflecting nature of metals, hence a relatively small depth of light penetration is observed. In the case of transparent samples, the maximum analyzable thickness depends on the spectral resolution of the instrument.

Figure 2.16 shows the schematic diagram of a spectroscopic ellipsometry system.

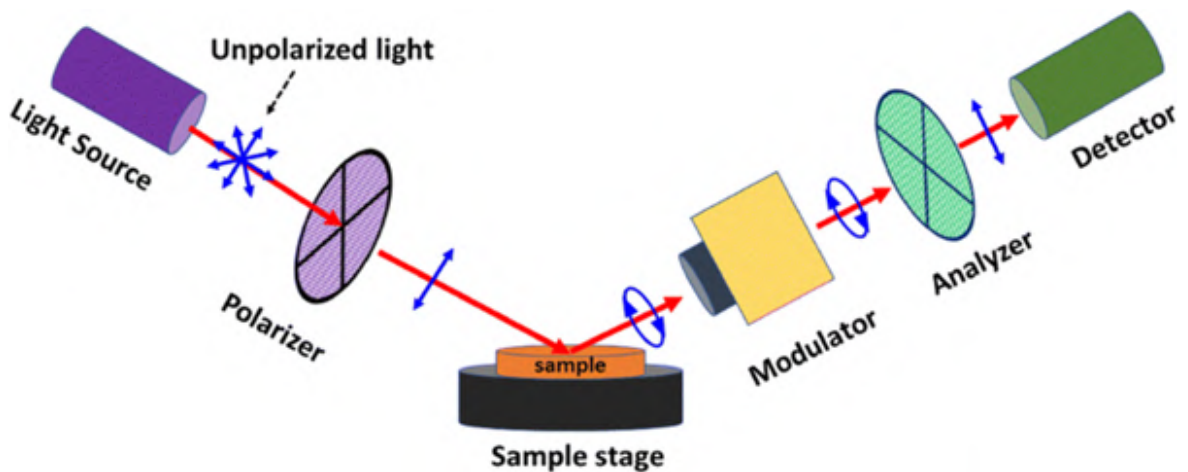


Figure 2.16 Schematic diagram of spectroscopic ellipsometry system [66]

Spectroscopic ellipsometers make use of polarized light to characterize samples. Light emitted from a source goes through a polarizer, is reflected at a grazing angle by the analyzed sample, returns through a modulator and an analyzer, and is collected by the detector. This detector measures the polarization state of the light reflected from the sample. The complex refractive index  $n(\lambda)$  of material describes this interaction of light with the sample material surface. In this complex refractive index, a real (refractive index  $n$ ) describes the change in light speed when penetrating the material, and imaginary part (absorption or extinction coefficient  $k$ ), which describes the way the light is either scattered or absorbed, as Equation 2.4 shows.

$$n(\lambda) = n - ik \quad (2.4)$$

When describing the change of polarization of light, a reference plane of incidence has to be established. This plane of incidence is perpendicular to the surface of the sample and is defined by the incident light beam and the direction normal to the surface. Figure 2.17 shows the direction of the light electric field vectors which expands in the plane of incidence and is referred to as  $E_p$ , and the amplitude of the electric field of the wave which waves perpendicular to the plane of incidence known as  $E_s$ . These waves

are referred to as p-wave and s-wave (labels refer to parallel and perpendicular).

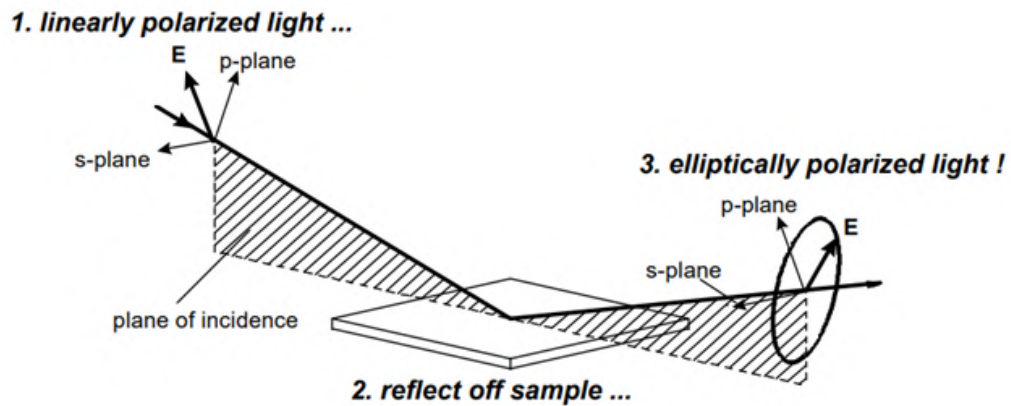


Figure 2.17 Schematic of interaction of linearly polarized light with a sample [47]

By calculating the ratio  $\phi$  between the reflectivity for p-polarized light ( $r_p$ ) and reflectivity for s-polarized light ( $r_s$ ), a polarization change can be defined. The mathematical description for this phenomenon is based on the Fresnel reflection equations (Equation 2.5).

$$\tan \psi e^{i\Delta} = \frac{r_p}{r_s} = \rho \quad (2.5)$$

This equation is often used in term of ellipsometry parameters  $\psi$  (Psi) and  $\Delta$  (Delta), where  $\psi$  is explained above, and  $\Delta$  defines the difference of the phase between reflected p- and s- polarized light. Often, spectroscopic ellipsometry measures the complex ratio  $\rho$  as a function of wavelength. Variable Angle Spectroscopic Ellipsometry (VASE) performs the above measurement as a function of both wavelength and angle of incidence [108]. In addition, a reference material is not necessary since this characterization technique calculates the ratio of two optical properties.

Since this technique does not directly measure film thickness or optical constants, an analysis of the obtained data is necessary to characterize the samples and gain useful information. Ellipsometry collects  $\psi$  and  $\Delta$  data at the desired spectral range for different angles of incidence. A simulation of the material optical properties has to be constructed and compared with the obtained measurements e.g., a model of the sample thin films with an approximate thickness on the established substrate is assumed. The model is then analyzed and compared with the measured data, until a good fitting is established. The obtained data undergoes an analysis process called data fitting, where a simulation replicates the experiment parameters with variable

parameters to find the best fit between the measured and the simulated data. The two fit parameters which are normally simulated are the film thickness and optical constants [108] and the most commonly used algorithm to fit and analyze spectroscopy data is the Marquardt-Levenberg algorithm [106].

By analyzing the optical properties at different wavelengths, useful information can be obtained from the different regions. The near infrared-region gives an insight about the material thickness, which is specially helpful for thicker samples, and describes with great accuracy the optical properties of the material. On the opposite side of the spectrum, the Far Ultraviolet (FUV) region helps to characterize the band gap of the material, as well as the crystalline structure, chemical composition of materials such as dielectrics and materials with lower conductivity properties. By analyzing the reflected light in the NIR spectrum, the thickness can be determined due to the reflection of the incident light. With increasing thin film thickness, the delay of the reflected light caused by the optical properties of the layer increases, as Figure 2.18 shows.

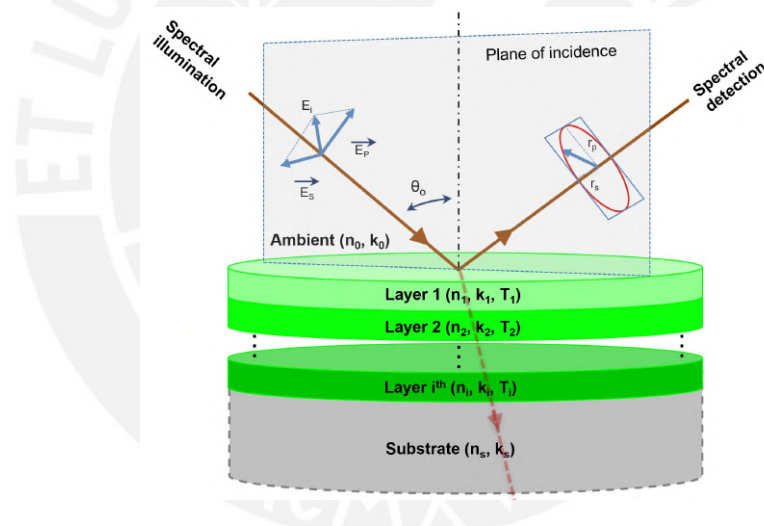


Figure 2.18 Schematic of effect to determine thin film thickness with spectroscopic ellipsometry in a multilayer system [12]

Both the physical thickness  $d$  and the index of refraction  $n$  create a phase delay. Thus, spectroscopic ellipsometry measurements contain the information to accurately measure both thickness and index. In the provided data, the position and the number of oscillations give information about the thickness. Generally, as the thickness  $d$  of the thin film increases, the oscillations created by the interference are deviated to longer wavelengths [47].

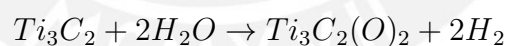
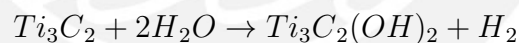
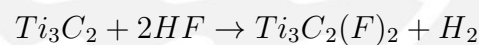
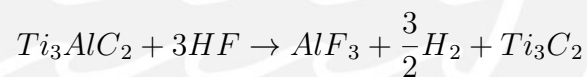
For this work, the optical properties ( $\psi$  and  $\Delta$ ) of the samples were measured using a SENresearch 4.0 Spectroscopic Ellipsometer by Sentech from 190 nm to 3500 nm.

The angle of incidence was varied from 50° to 70° in 5° steps. The software chosen to analyze the collected data was SpectraRay4 comprehensive ellipsometry software.

## 2.8 Etching Method to synthesize MXenes

In 2011, Gogotsi and Barsoum et al. [15] discovered a new and revolutionary method to synthesize MXenes out of MAX phases by simply removing the A atomic layers. The selective etching with HF is possible due to the high reactivity between the aluminum atoms and the fluor ions.

The bonds between the early transition metal M and the X atom show a covalent nature with an ionic percentage in some cases with high binding strength. In contrast, the bond between the early transition metal M and the A atom bonds are metallic bonds, which is normally referred to as a relatively weak binding strength. Thus, the removing of the A layers from the MAX phase is possible by simply employing specific etchants containing fluor such as LiF, HF etc [103]. By removing the A atoms, the sheet surfaces get occupied by terminating reactive groups initially from the etchant such as e.g., O, (OH) and F. The etching process of  $Ti_3AlC_2$  to synthesize  $Ti_3C_2$  takes place as follows



These ion exchanges result in weak 2-dimensional sheets with a MXT composition, where T indicates the surface termination obtained from the etchant. Depending on the T atom, the material properties vary and can be tailored through the choice of etching solution. This selective etching has as a result an accordion-shaped two-dimensional carbide with Van der Waals forces holding it together. By employing delamination strategies, 2-dimensional nanosheets are synthesized. Additionally, intercalation agents can be used to increase the interlayer spacing of these sheets and therefore facilitate this process. Various chemical and physical routes has been intensively researched. However, the dominant method thus far still remains the usage of hydrofluoric acid, HF, or fluoride salts and hydrochloric acid, HCl [6]. Figure 2.19 shows this synthesis

process.

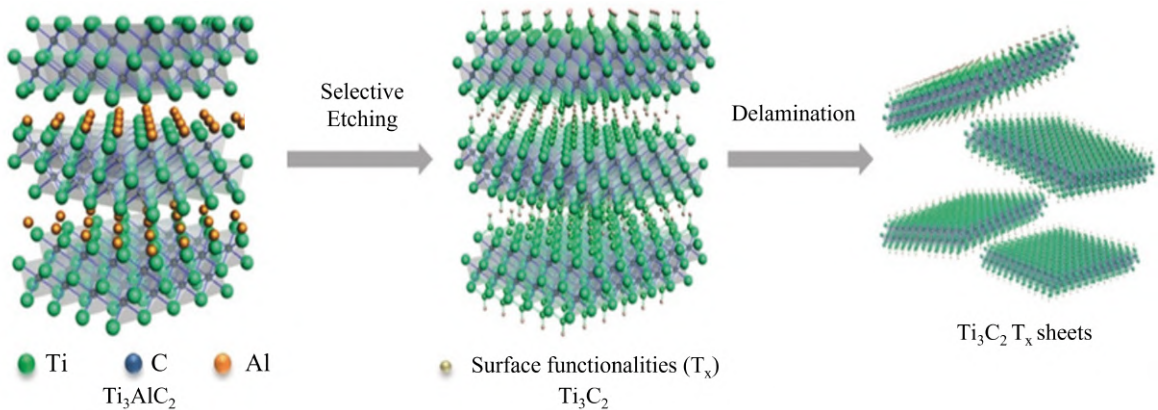


Figure 2.19 Schematic principle of synthesis of MXenes nanosheets [111]

In this work, the selective etching of Al atoms from the MAX phases  $\text{Ti}_2\text{AlC}$  and  $\text{Ti}_3\text{AlC}_2$  was carried out with 1% hydrofluoric acid HF solution at room temperature for different amount of time as Figure 2.20 shows.



Figure 2.20 Etching process with 1% HF by using a Teflon protective mask (indicated in yellow)

Firstly, the surface of the sample was cleaned by using isopropyl alcohol. Since the MAX phase was already deposited on the substrate, this step had to be carried with extreme precaution not to damage the surface and therefore influence the etching process. Subsequently, a protective mask covered with polytetrafluoroethylene (PTFE) tape, also known as its commercial name Teflon, was placed and fixed in order to prevent the leakage of the liquid HF to the sides. This way, the etching process will only take place on the surface of the MAX phase and the etching from the edges of the MAX phase will be avoided. This method is based on the hydrophilic character of HF by Teflon and constitutes an economical and convenient method of control direction of the etching process in the sample. After the etching process the protective mask was removed and the surface was again cleaned carefully with isopropyl alcohol. This process was repeated for 30 minutes periods until the delamination of the sample.



## 3 Deposition of the ternary system Ti-Al-C

### 3.1 Determination of the deposition rate

Since the deposition rates for all three elements (Ti, Al, and C) were unknown for the sputtering system at PUCP at first, a previous experiment was necessary to determine the deposition parameters. For that matter, titanium, aluminum, and carbon monolayers were deposited by RF magnetron sputtering using high purity elemental targets, as specified in Table 3.1. Its thickness was determined by X-ray Reflectometry (XRR) and Variable-Angle Spectroscopic Ellipsometry (VASE).

Because of the thickness limitation that the XRR technique presents ( $d < 150$  nm) [109], a thickness of around 50 nm was pursued for all 3 monolayers by fixing the deposition time and power to 20 minutes and 60 W each. The films were deposited on a n-doped silicon substrate Si (100), which was placed at a target-to-substrate distance of 50 mm with active cooling. The argon gas flow rate during deposition processes was held constant at 30 sccm. Carbon might present adhesion problems when deposited as monolayer. By depositing a thin titanium layer on the air/film interface of around 5 nm, the delamination of the carbon thin film can be avoided. Further deposition details can be found in Table 3.1

Table 3.1 Sputtering conditions of titanium, aluminum, and carbon monolayers

	Titanium (Ti)	Aluminium (Al)	Carbon (C)
Target	99.99 %	99.99 % (Able Targets)	99.99 % (Plasmaterials)
Base pressure	$1.2 \times 10^{-6}$ mbar	$5.7 \times 10^{-7}$ mbar	$8.99 \times 10^{-7}$ mbar
RF power	60 W	60 W	60 W (+ 90 W Ti)
Deposition time	20 min	20 min	20 min (+ 3 min Ti)

To corroborate the homogeneity of the monolayers, top-view SEM images were taken as Figure 3.1 shows.

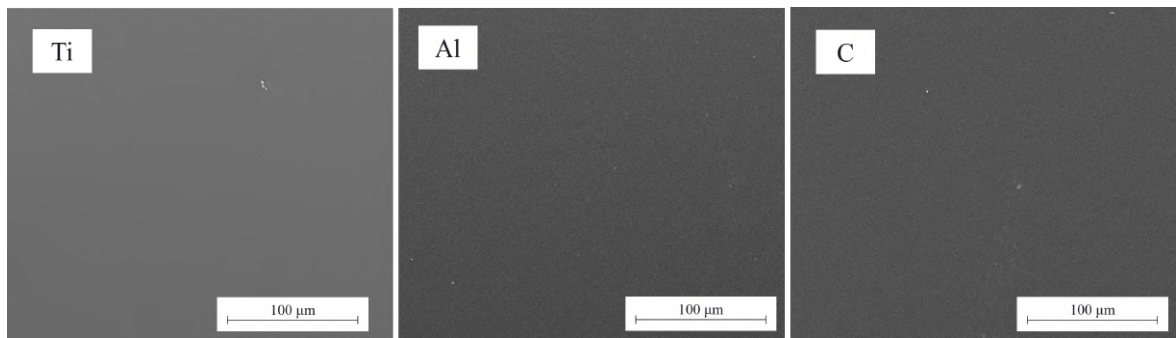


Figure 3.1 SEM top-view image of the Ti, Al and C monolayers as deposited

The monolayers show a closed, uniform layer with no apparent damage of the surface, which indicate a successful deposition. To determine the chemical composition of the monolayers, an EDX analysis was performed, as Figure 3.2 shows.

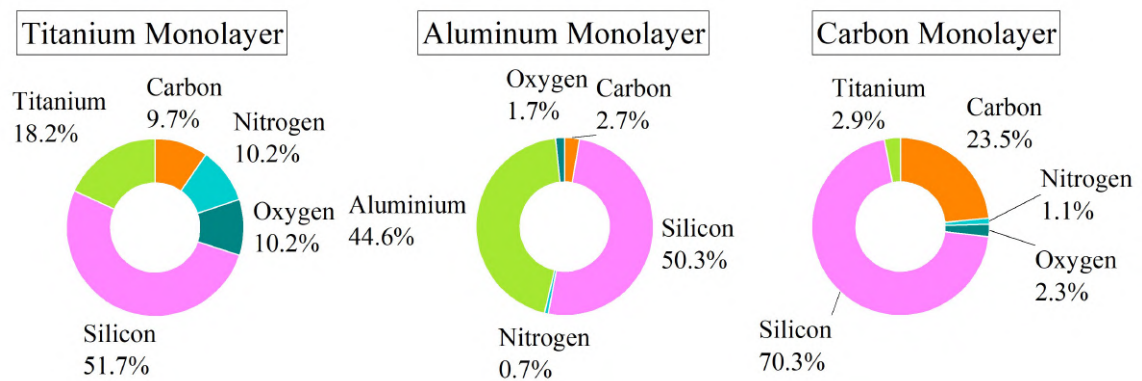


Figure 3.2 EDX results in at% of the as deposited titanium, aluminum, and carbon monolayers. Further details of the measurement as well as the corresponding EDX spectra can be found in the annex

The EDX analysis shows the expected chemical composition of the monolayers and corroborates the homogeneity of the deposition. Remnants of oxygen and nitrogen are habitual due to the deposition process, and can be excluded from the analysis. All three analysis were performed using 5 kV as acceleration voltage. Because the minimum acceleration voltage for titanium lies between 5 kV and 10 kV ( $K_{\alpha, Ti} = 4.508$  kV [75]), the concentration of titanium in its monolayer does not correspond the reality and has to be considered carefully.

Structural parameters such as thickness, density and interface roughness of each film were determined non-destructively by X-ray Reflectometry (XRR) using monochromatized  $CuK_{\alpha}$  radiation in a grazing incident ( $0.5^{\circ} - 3^{\circ}$ ) configuration. These X-ray reflectivity measurements were analyzed by fitting to the measured data a simulated curve calculated using the Levenberg-Marquardt method and simplex method in Leptos.



Figure 3.3 shows the reflection intensity (reflectivity) based on the incident angle  $\theta$  with respect to the thin film surface.

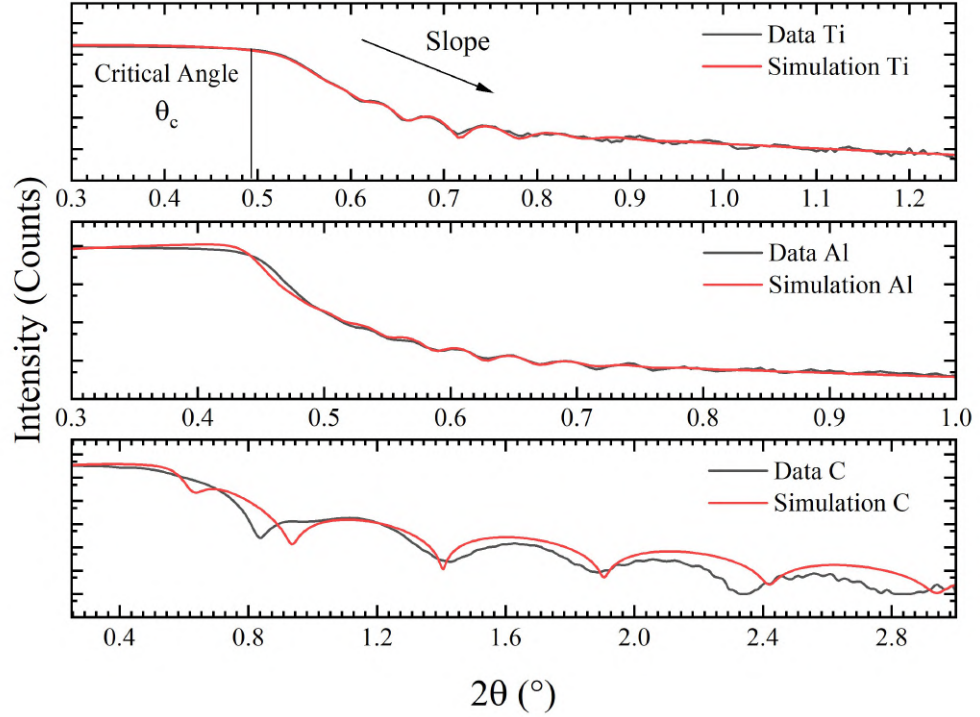


Figure 3.3 X-ray Reflectivity curves (black) of Ti, Al, and C (+ Ti) monolayers deposited on silicon substrates and simulated fitting curves (red) obtained by Leptos. Notice that the values in the x-axis are different for each graph

When X-Rays are incident on the surface of a material with a refractive index slightly smaller than 1, they are reflected off it. In case the incidence angle is smaller than the critical angle for total reflection ( $\theta_c$ ), the X-Ray undergo total reflection and do not penetrate into the material, which can be observed as a plateau in the reflectivity curve. While increasing the incident angle ( $\theta > \theta_c$ ), X-ray reflectivity decreases since a fraction of it penetrates into the material by refraction whereas the rest of them are reflected. The penetrated X-Rays are incident on the film/substrate interface are as well reflected when reaching the film/substrate interface. Interference occurs between the X-Rays reflected from the surface and the film/substrate interface. These interference causes oscillations or fringes in the reflectivity curve, which depend on the thickness of the film. The thicker the film, the shorter the period of the oscillations. Following Equation 3.1, the film thickness  $D$  can be calculated using the observed angle of fringe  $\theta_i$

$$m\lambda = 2D\sqrt{\sin^2 \theta_i - \sin^2 \theta_c} \quad (3.1)$$

where  $m$  stands for integer number of fringe; and  $\lambda$  for the wavelength of the X-Ray.

Additional information can be subtracted from the reflectivity curve e.g., thin film density. The oscillations amplitude depends directly from the density difference thin films/substrate. The greater this density difference, the higher the amplitude of the oscillation [68]. To obtain information about the surface roughness, the curve slope has to be analyzed. The rougher the thin films surface, the more pronounced is the decrease of the reflectivity. By analyzing the reflectivity curves for all three monolayers, we obtain the thickness, roughness and density as summarized in Table 3.2.

Table 3.2 Obtained values (thickness, roughness and density) of the titanium, aluminum and carbon monolayers obtained by X-Rax refraction (XRR)

Element	Thickness (nm)	Roughness ( $\mu\text{m}$ )	Density ( $\text{g}/\text{cm}^3$ )
Titanium	$93.943 \pm 0.711$	$5.593 \pm 0.059$	$3.743 \pm 0.007$
Silicon	/	1.648	2.329
Aluminum	$149.169 \pm 5.686$	$7.610 \pm 0.189$	$2.339 \pm 0.008$
Silicon	/	$2.817 \pm 0.185$	2.329
Titanium	$14.369 \pm 0.409$	$3.347 \pm 0.245$	$4.226 \pm 0.109$
Carbon	$16.853 \pm 0.786$	$1.695 \pm 0.318$	$2.339 \pm 0.100$
Silicon	/	$1.463 \pm 0.366$	2.329

To corroborate the obtained thickness values, a variable-angle spectroscopic ellipsometry (VASE) measurement was performed. For that purpose,  $\psi$  (psi) and  $\delta$  (delta) values were measured with different angles ( $50^\circ - 70^\circ$ ) for a spectral range between 190 nm and 3500 nm. The acquired curves can be found in annex. The thickness values of the three monolayers deposited at 60 W for 20 minutes each are summed up in Table 3.3.

Table 3.3 Measured thickness values of titanium, aluminum, and carbon monolayers by variable-angle spectroscopic ellipsometry (VASE) and X-Ray reflectometry (XRR)

Monolayer	Ellipsometry	X-Ray Reflectometry	Deposition Rate
Titanium	$91.66 \pm 0.10$ nm	$93.94 \pm 0.74$ nm	4.6 nm/min
Aluminum	/	$149.16 \pm 5.69$ nm	7.46 nm/min
Carbon	$13.54 \pm 0.10$ nm	$16.85 \pm 0.79$ nm	0.76 nm/min

From these values, future deposition parameters such as deposition time and deposition power can be planned in order to obtain the desired stoichiometrically necessary thicknesses for the synthesis of the desired Ti-Al-C MAX phases.

### 3.2 Co-sputtering of Ti-Al-C thin films

The term “co-sputtering” describes the deposition process of two or more target materials to produce thin films which are customizable in chemical composition and morphology. In the deposition from e.g., two targets, the material flux results from two different material sources (Figure 3.4a), whereas the center of the substrate receives an equal amount of both materials. The composition of the resulting thin film can be tailored by adjusting the deposition parameters of the different targets, as well as the geometrical position inside the chamber. Figure 3.4b) shows the deposition with an alloy target with a fixed composition. The Ti, Al and C atoms, eroded because of the collision of argon ions from the target, reach the substrate condensing in a thin film that is a combination of the three materials. In the so-called mosaic target (Figure 3.4c), two or more elements are placed forming a mosaic in the same target.

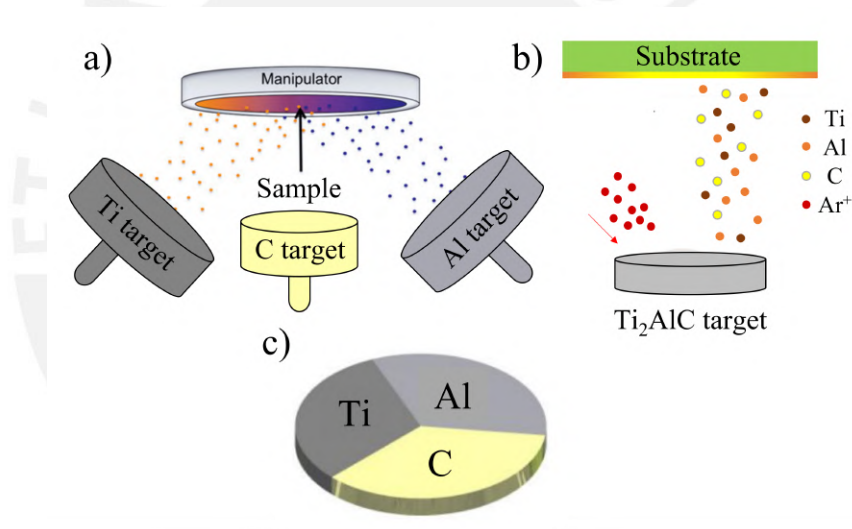


Figure 3.4 a) Schematic of co-deposition with elemental Ti, Al and C targets (Adapted from Ref. [97]) b) Schematic of co-deposition with a  $\text{Ti}_2\text{AlC}$  target (Adapted from Ref. [114]) c) Schematic of mosaic target of Ti, Al and C (Adapted from Ref. [17])

When depositing from one target, the deposition parameters are more challenging to control since the deposition power remains constant for the target. Therefore, the stoichiometric control of the thin film resides only in the form or concentration gradient of the single elements in within the target. For this reason, the co-deposition from different targets presents an advantage with respect of a co-deposition with a mixed target and will be employed in this work.

Using multiple pure elements targets, the deposition can take place either simultaneously (co-deposition) or sequentially as a multilayer system. The possibility of

depositing from one or more targets allows the creation of pure thin films as well as alloy and other composites.

In simultaneous co-sputtering of titanium, aluminum and carbon, the stoichiometry of the resulting thin film is controlled by optimizing the power and geometrical position of each target separately inside the chamber. In the multilayer system, the periodic structures depend on the sputtering time and power. A subsequent ex-situ annealing process in an inert gas converts the as-deposited thin films in the desired MAX phase films. The stoichiometry of the resulting MAX phase thin film is related to the stoichiometry of the as deposited thin films.

In the presented work,  $\text{Ti}_2\text{AlC}$  and  $\text{Ti}_3\text{AlC}_2$  MAX phases are studied because of their remarkable characteristics as protective coatings [92]. The focus remains on these MAX phases from both the Ti-Al-C precursor as multilayer system and as co-sputtered thin film based on a Ti:Al:C ratio of both 2:1:1 and 3:1:2. Therefore the number of atoms in the precursor thin film has to correspond with this correlation. However, various authors deposit larger amounts of aluminum in order to ensure the formation of the MAX phase since titanium has a higher affinity to create TiC rather than TiAl [30][92][13]. An aluminum saturated compound will increase the possibilities for the MAX phase, as the phase diagram for Ti-Al-C in Figure 3.5 shows.

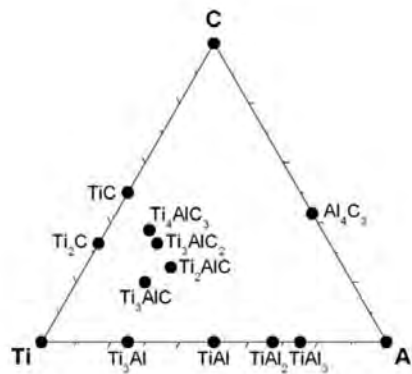


Figure 3.5 Phase diagram for Ti-Al-C [22]

In the multilayer system, the thickness of the monolayers, and therefore the stoichiometry of the resulting thin film, has to be adjusted by regulating the time and power of each layer individually. For all three elements, the power was adjusted to its maximum capacity (90 W) to reduce the deposition time. The necessary time for the individual thicknesses, determined by means of the calculated deposition rate aforementioned, is summarized in Table 3.4.

Table 3.4 Deposition parameters for Ti-Al-C multilayer system to achieve the necessary stoichiometry of the MAX phase

Target	Required Thickness	Power	Deposition Time
Titanium	14 nm	90 W	2 min 4 s
Aluminum	6 nm	90 W	35 s
Carbon	3.5 nm	90 W	2 min 55 s

The Ti-Al-C cycle was repeated 7 times resulting in a total layer thickness of 150 nm as Figure 3.6 shows.

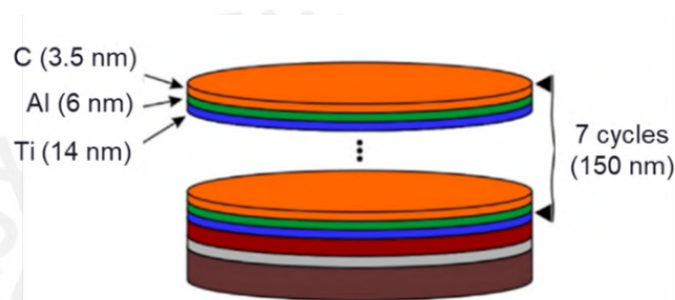


Figure 3.6 Schematic representation of the deposition of Ti-Al-C multilayer system (Reprinted from Reference [96])

For the co-deposition from different targets, the stoichiometry was ensured by adjusting the deposition powers for each target individually. For a total time of 30 minutes and 37 seconds, the powers of Ti, Al and C were established to 41 W, 11 W and 90 W respectively.

The thin films were deposited on a silicon (111) substrate coated with a 50 nm silicon nitride ( $\text{Si}_3\text{N}_4$ ) amorphous top-layer. This coating prevents the interdiffusion of silicon and the Ti-Al-C multilayer system [37]. Before the RF sputtering processes, the substrates were cleaned in acetone, isopropyl alcohol, and distilled water for 10 min in an ultrasonic cleaning device. The sputtering chamber was vacuumed up to the base pressure of  $1 \times 10^{-7}$  mbar using both a mechanical and a turbomolecular pump. A highly pure (99.9999%) argon environment was established with a gas flow of 30 sccm. Then, the titanium, aluminum and carbon targets specified in Table 3.1 were pre-sputtered to clean the target surface and the chamber for 15 min at the maximal power of 90 W. The target-to-substrate distance was fixed for all depositions at 5 cm.

To investigate the role of the temperature in the morphology of the as-deposited co-sputtered and multilayered thin films, active heating during deposition was turned on with two lamps and established at 100 °C. Henceforth, the samples will be desig-

nated firstly as the deposition technique (multilayer or co-sputtering) followed by the deposition temperature. Notwithstanding the fact that the temperature inside the chamber while depositing without active heating was not measured, the designation for these samples will remain “room temperature” (RT). A subsequent heating process was carried for all samples under vacuum with help of an inert gas (Ar) at various temperatures (600 °C, 700 °C, 800 °C, 900 °C and 1000 °C) making use of a tubular alumina oven.

For reference, a multilayer system at normal configuration (0°) was deposited in order to compare the properties of both deposition configurations. Henceforward, these samples will be addressed as Reference Multilayer System.

Although the exact synthesis process of MAX phase thin film is still unknown, the generally accepted theory is the intercalation of the aluminum atoms in the titanium carbide hexagonal structure. Firstly, titanium and carbon react to TiC forming a hexagonal structure. Thereafter, aluminum intercalates in this hexagonal structure, creating the MAX phase. Knowing this, an aluminum excess can optimize the synthesis process and guarantee the formation of a stoichiometric accurate MAX phase. Nonetheless, a disproportionate excess of Al interferes by creating TiAl intermetallic phases, as Figure 3.5 implies. Taking this into account, the optimal ratio Ti:Al can be established to be around 1.2 as an approximate reference. Additionally, the concentration of carbon varies considerably depending on the deposition configuration. This can be explained by the difference in density between the carbon layer deposited by magnetron sputtering and the graphite, whose value was chosen to calculate the deposition parameters. Furthermore, one of the limitations of the EDX analysis is its difficulty to analyze light elements with an atomic number lower than  $Z = 11$  such as carbon [34]. Therefore, the concentration of this element has to be carefully analyzed and questioned at all times.

The elemental composition of the as deposited thin films on silicon substrate obtained by EDX analysis are sum up in Figure 3.7. Overall, this result indicates that the composition of the thin films is very close to the theoretical ideal stoichiometry of Ti:Al:C (2:1:1). However, except for the multilayer system deposited at room temperature, which has an aluminum abundance, the deposited thin films Ti:Al ratio are distant from the referential necessary  $\sim 1.2$  ratio for creating a MAX phase. This result insinuates that only the multilayer thin films deposited at room temperature are a suitable candidate for the formation of MAX phase regarding the chemical composition.

Sample	Ratio Ti:Al
Multilayer at room temperature	1.38
Multilayer with active heating	2.84
Co-sputtering at room temperature	2.89
Co-sputtering with active heating	2.00
Reference Multilayer System	1.20

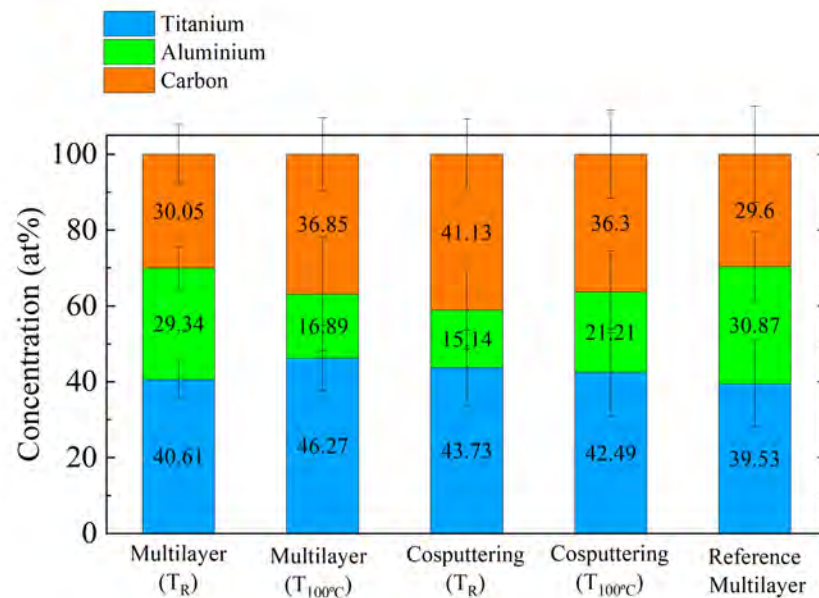


Figure 3.7 Chemical composition of thin films with various deposition configurations as deposited and its corresponding Ti:Al ratio

Figure 3.8 shows the evolution in the composition of the thin films as a function of the annealing temperature. The composition remains relatively constant for all thin films at all annealing temperatures. Only in the multilayer system deposited at room temperature ( $M_{RT}$ ) the composition varies at higher annealing temperatures. Concentrating on that sample, at an annealing temperature of 800 °C the aluminum and carbon concentration equal each other ( $c_{Al} = 29.66 \pm 5.65 \text{ at}\%$ ,  $c_C = 29.67 \pm 7.78 \text{ at}\%$ ). The ideal 1.2 ratio of Ti and Al is almost achieved ( $c_{Ti} = 40.67 \pm 4.97 \text{ at}\%$ ) and therefore still suitable for the creation of MAX phase. At 1000 °C, the concentration of both elements aluminum and carbon equals each other again ( $c_{Al} = 25.95 \pm 5.85 \text{ at}\%$ ,  $c_C = 23.45 \pm 7.66 \text{ at}\%$ ). This time, the ideal ratio of Ti:Al is accomplished ( $c_{Ti} = 50.63 \pm 4.75 \text{ at}\%$ ) with a slight aluminum excess. The fact that this sample still fits the chemical concentration requirements at higher temperatures indicates the possible formation of MAX phases after annealing processes.



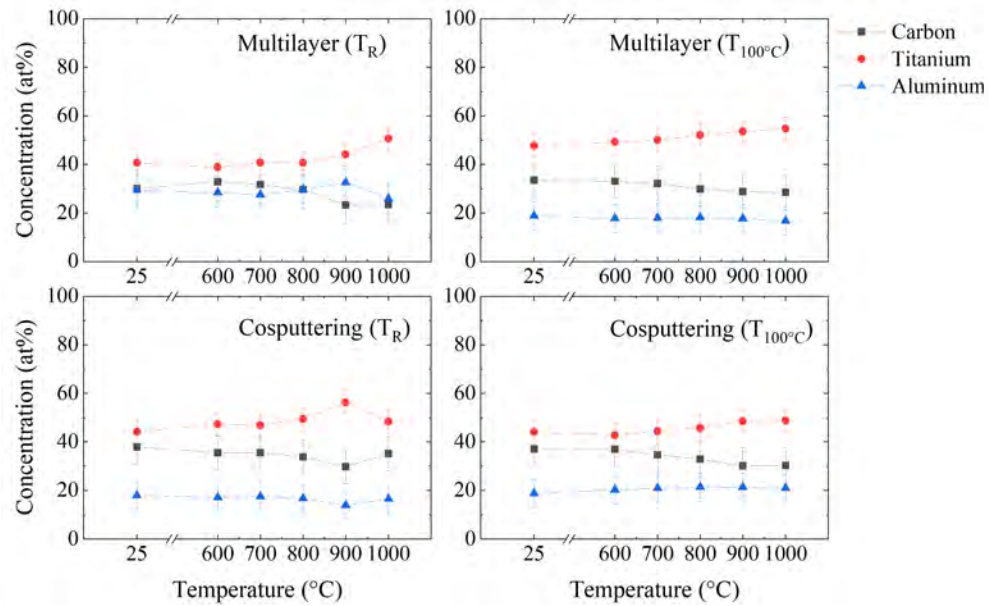


Figure 3.8 EDX analysis of titanium, aluminum and carbon in thin films deposited at different configurations as deposited and after annealing processes using the tubular alumina oven (600 °C, 700 °C, 800 °C, 900 °C and 1000 °C) taking into account only the above mentioned elements. Notice that the lines drawn between the data were not measured and are only included to guide the eye.

When observing not only titanium, aluminum, and carbon, but all elements detected on the thin film, as Figure 3.9 shows, an increase in oxygen becomes noticeable. This can be explained by the annealing method, and can be attributed to residual oxygen in the oven, and the exposure of the samples to the ambient. Again, the limitation for light element analysis via EDX could be also a reason for this increase in composition.



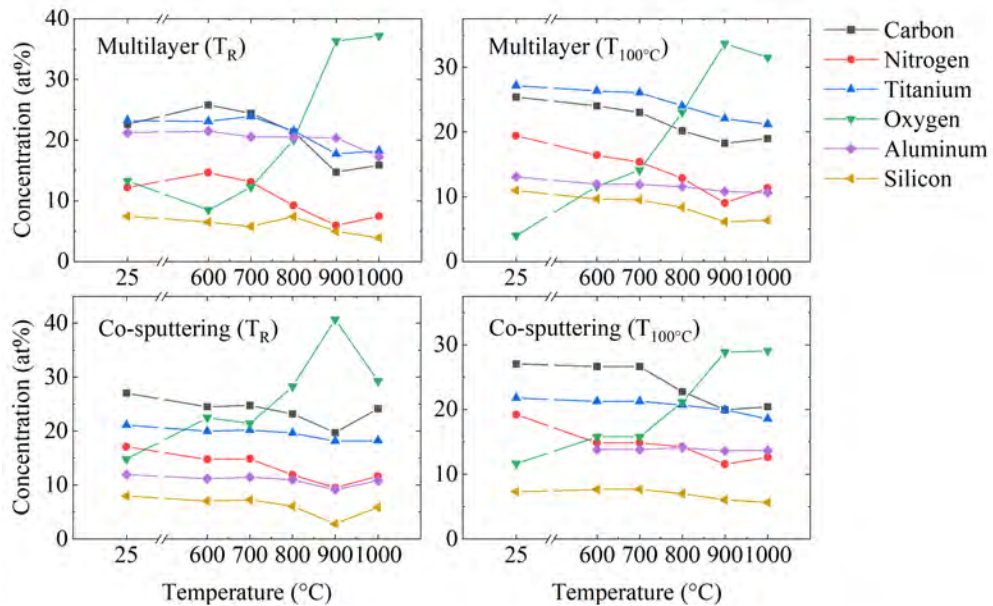


Figure 3.9 EDX analysis of thin films deposited at different configurations as deposited and after annealing processes using the tubular alumina oven (600 °C, 700 °C, 800 °C, 900 °C and 1000 °C) taking into account all elements. Notice that the lines drawn between the dots were not measured and are only included to guide the eye.

To unravel the possible morphology changes of the thin films depending on the deposition configuration and the annealing temperature, an XRD analysis was conducted. Figure 3.10 presents the X-Ray diffraction patterns of the as deposited and annealed Ti-Al-C thin films in the configurations explained above for different annealing temperatures (800 °C and 1000 °C) using a tubular alumina oven.

A broad peak is often observed around  $\sim 14^\circ$  which corresponds to the silicon wafer escape peak. Escape peaks are produced from the photoelectric interaction of the incident radiation with the detector material atoms and the subsequent escape from the crystal of its characteristic X-ray [53]. This effect can be avoided by rotating the sample around its axis ( $\phi$ ) until this effect is mitigated [78] or by lowering the high-voltage on the X-ray tube [58]. For this reason, some patterns exhibit this broad peak yet others were in the correct position, avoiding this effect. Further peaks can be found at  $\sim 33^\circ$  and at  $\sim 58.9^\circ$ , and correspond to the forbidden silicon (200) peaks due to multiple diffraction, also known for its German name “Umweganregung” [78].

The lack of additional diffraction peaks demonstrates that the titanium and aluminum thin films were grown amorphous. Carbon thin films, as expected, are grown likewise amorphous. After the annealing processes, the XRD patterns do not show any significant

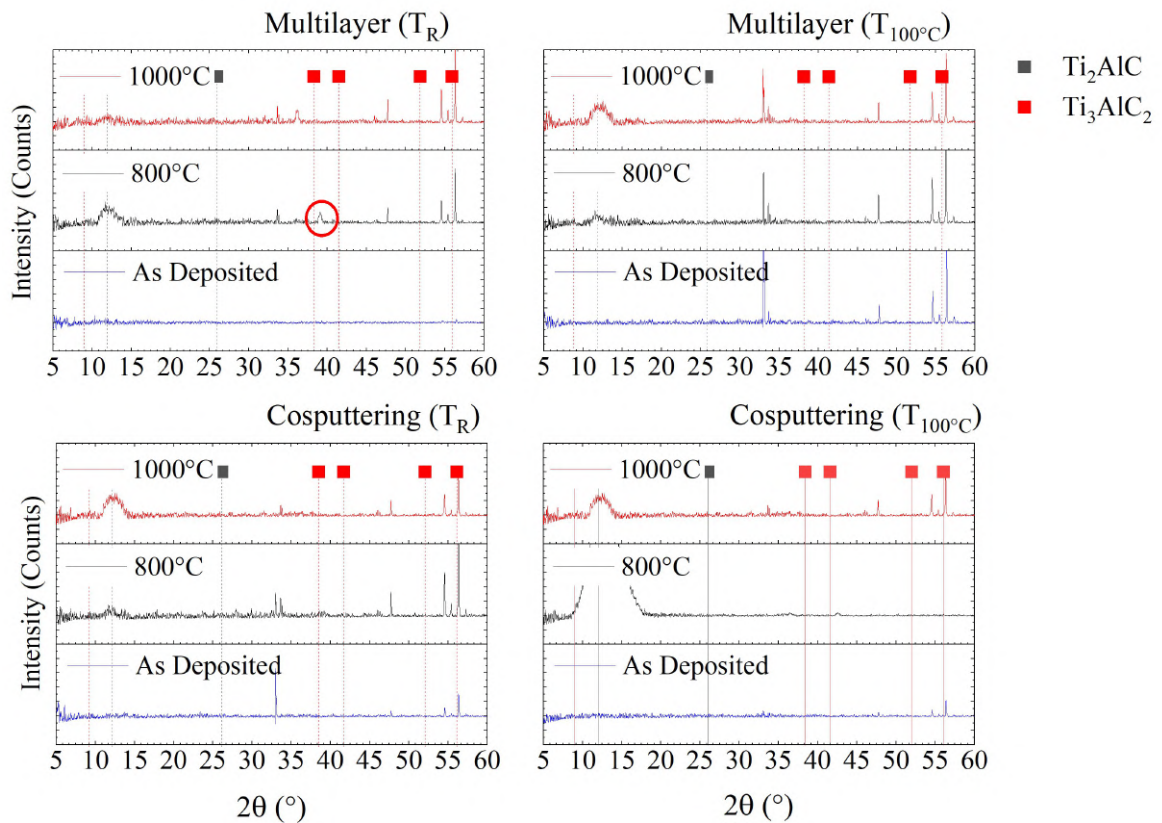


Figure 3.10 BB-XRD patterns of Ti-Al-C co-deposited thin films deposited at different configurations as deposited and after annealing processes using a tubular alumina oven (800 °C and 1000 °C)

changes. However, for the multilayer system deposited at room temperature ( $M_{RT}$ ) and annealed at 800 °C, a peak at  $\sim 39^\circ$  indicated with a red circle reveals the possibility of the formation of  $Ti_3AlC_2$  compound. By further annealing this sample at 1000 °C, the peak moves to  $37^\circ$  in which the titanium carbide  $TiC$  peak is characteristic.

To further analyze the structural properties of the thin films, Raman spectroscopy analyses were performed. Figure 3.11 shows the Raman spectra of the thin films in different configurations as deposited and after annealing processes at various temperatures annealed with the tubular alumina oven (600°C, 700°C, 800°C, 900°C and 1000°C).

The peak observed at  $\omega_{Si} = 520 \text{ cm}^{-1}$  is related to crystalline silicon from the substrate. The Raman spectra of the as deposited thin films show no relevant peaks beyond this characteristic silicon peak, which implies that the thin films were deposited amorphous, matching the previous XRD result. This result relies on the fact that the pure metal nanolayers are not related to polarizability changes caused by lattice vibrations [96]. The carbon peaks corresponding to the D- and G-band can be found at around  $1300 \text{ cm}^{-1}$  and  $1590 \text{ cm}^{-1}$  [87] respectively for all patterns.

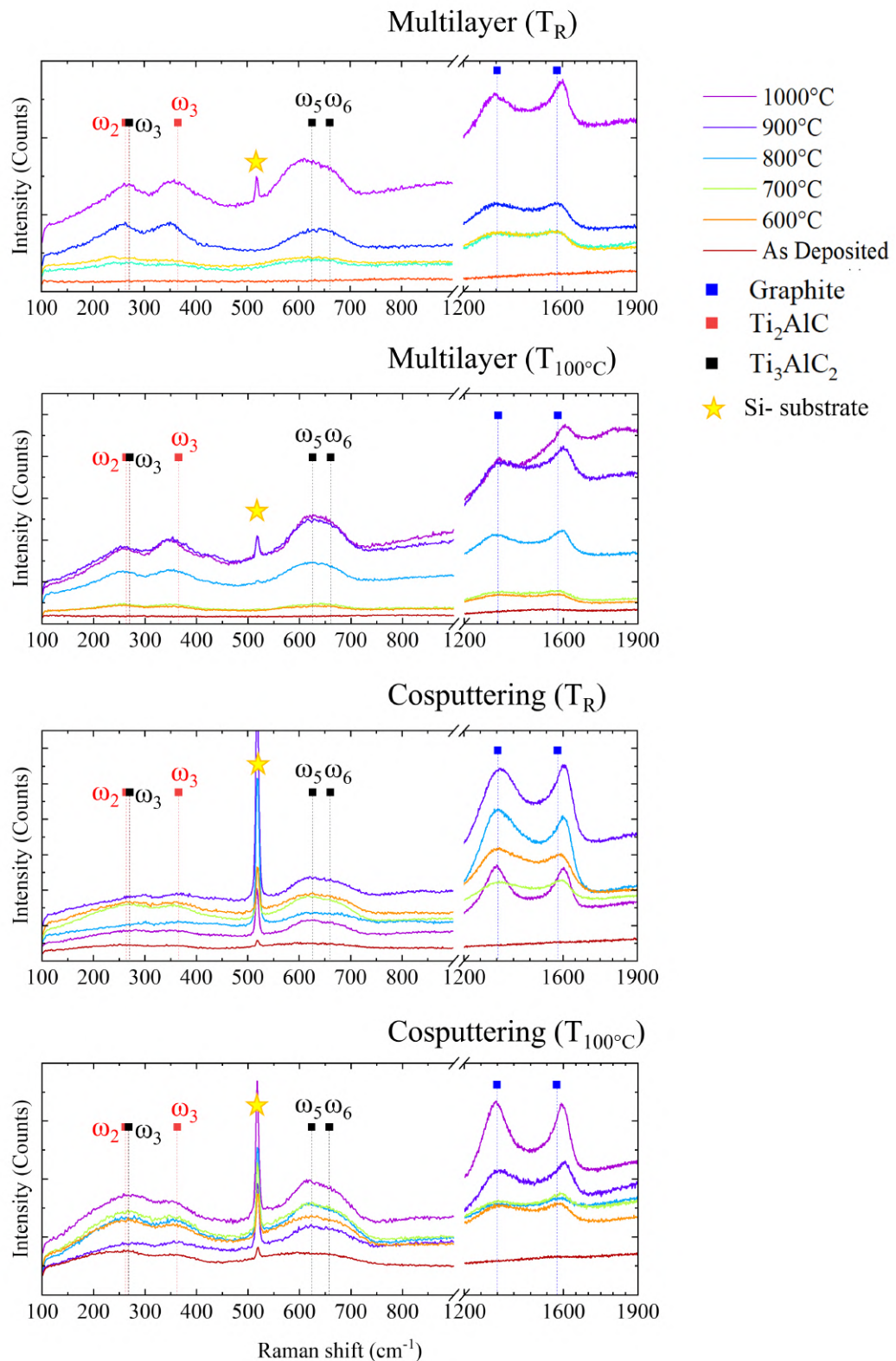


Figure 3.11 Raman spectra of Ti-Al-C co-sputtered thin films deposited at different configurations as deposited and after annealing processes using a tubular alumina oven (600 °C, 700 °C, 800 °C, 900 °C and 1000 °C)

With increasing annealing temperatures, the patterns start showing broad peaks at around  $\omega_1 = 280 \text{ cm}^{-1}$ ,  $\omega_2 = 360 \text{ cm}^{-1}$ , and  $\omega_3 = 620 \text{ cm}^{-1}$ . This evolution towards the vibrational modes of  $\text{Ti}_2\text{AlC}$  and  $\text{Ti}_3\text{AlC}_2$  implies the reorganization of atoms due to increasing temperature. Moreover, the peaks related to the Ti-Al vibrations reported in the literature at  $\omega = 185 \text{ cm}^{-1}$  and  $\omega = 272 \text{ cm}^{-1}$  [100] are not observed. Likewise, the peaks corresponding to the Ti-C vibrations found at  $\omega = 154 \text{ cm}^{-1}$ ,  $\omega = 204 \text{ cm}^{-1}$ , and  $\omega = 623 \text{ cm}^{-1}$  are not noticeable. However, as mentioned before, the multilayer system deposited at room temperature shows a positive evolution toward the  $\text{Ti}_3\text{AlC}_2$  compound, showed in the narrow peaks matching its theoretical peaks [92][9][30]. By this means, by adjusting the annealing parameters the creation of MAX phase from the different deposition configurations could be achieved.

### 3.3 Influential parameters in the deposition of thin films via sputtering

To understand the morphology of the sputtered thin films, the individual steps of the thin film growth have to be understood. In the first step, also called nucleation, the vapor above the substrate experiences a phase transition to a solid on the surface of the substrate. This condensation process sets the starting point to the formation of the thin film. Its atomistical configuration on the surface depends on the energetical preferences of the atoms.

If the incident atoms are adsorbed by the material surface, many microscopic processes can take place: the adsorbed atoms can form a nucleus by joining together, whereas independent atoms can adjoin already adsorbed nuclei. If the atom is not adsorbed by the surface, it can be repulsed from the surface [39]. The dominating process is determined by energetic requisites e.g., the surface kinetics, the interface and the atoms to be condensed.

Three-dimensional nuclei can be adsorbed if atoms interact between them instead of with the substrate, which is called island or Volmer-Weber growth (Figure 3.12a). A monolayer is formed in case the adsorbed atoms are energetically bound to the material substrate between them. This growth mode is named layer or Frank-van der Merwe growth (Figure 3.12b). When combining both growth modes, the so-called layer plus island or Stranski-Krastanov growth (Figure 3.12c) takes place. Because of strong interaction of the atoms with the substrate, they will first cover the surface in layers. After several layers and because of the decrease in surface energy, islanding will occur

[39].

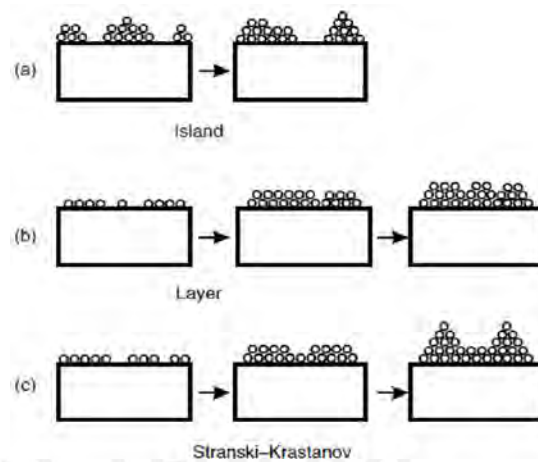


Figure 3.12 Modes of growth of thin films: (a) Volmer–Weber island growth (b) Frank–van der Merwe layer growth and (c) Stranski–Krastanov layer plus island growth [38]

Experiments carried by J.A. Thornton (1977) [94] explain the morphology of the sputtered thin films as a function of the substrate temperature, normed to the melting temperature of the material, and the inert gas pressure (in mbar). The results are summed up in its homonymous model: the Thornton structure zone model, as Figure 3.13 shows. In this model, the three basic zones provides helpful information about the film growth and therefore its morphology in sputtered thin films. This morphology depends on various parameters such as substrate temperature, inert gas pressure and the application of a small negative potentiation to the substrate, also known as bias [83].



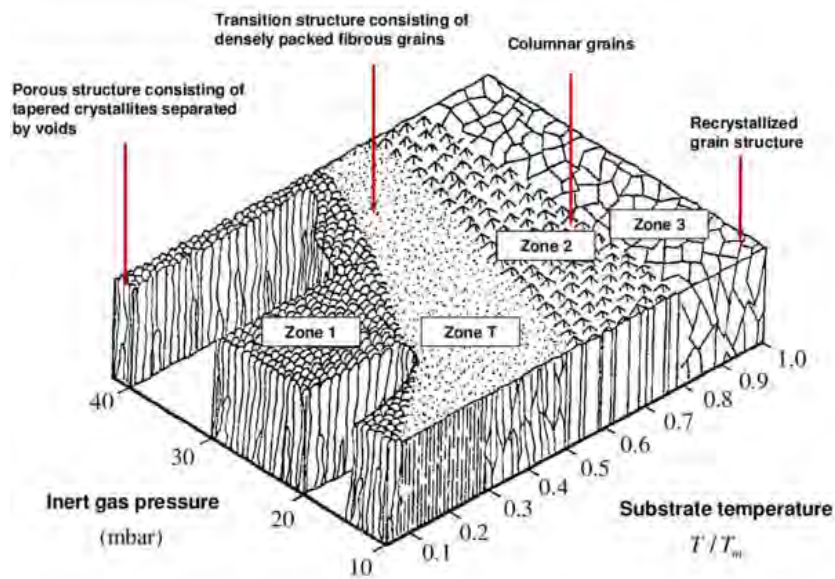


Figure 3.13 Thornton structure zone model [94]

After the nucleation process, the continuous flowing vapor atoms deposit onto the surface. Atomistic diffusion plays a crucial role into the growth of the thin films. This diffusion depends on temperature, in this case substrate temperature  $T$ . By analyzing the morphology as a function of substrate temperature  $T$  and gas pressure  $p$ , three differentiated zones can be appreciated: Zone 1 occurs at relatively low substrates temperatures, where there is not enough thermal energy to activate the diffusion. In this zone, the microstructure is composed of narrowed columns with domed upper section separated by voids. When temperature increases, the columns diameter increases. A higher density with less porosity and more defined columnar structure is characteristic for this zone. As a result of higher diffusion processes, the column diameter increases as the temperature increases (Zone 2). At higher temperatures, recrystallization processes start occurring and the energy is sufficient for bulk diffusion. Therefore, the characteristic morphology of this zone consists of equiaxed grains (Zone 3). This growing mechanism plays a crucial role in the deposition of thin films not only at normal configurations, but also at off-normal configurations, like at oblique angle deposition.

### 3.4 Oblique Angle Deposition of the ternary system Ti-Al-C

Thin films fabricated by MS are normally deposited in substrates placed perpendicular to the material flux, resulting in compact thin films. Innovative nanostructural possibilities are being explored in recent years by taking advantage of the deposition at oblique angles. By placing the substrate at a defined angle respect to the targets as Figure 3.14 shows, shadowing-driven nanostructuration processes induce the development of highly porous structures [7].

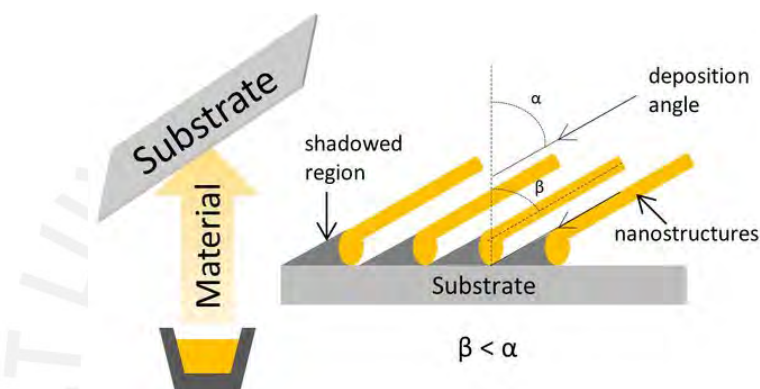


Figure 3.14 Scheme of oblique angle deposition (OAD) outlining the influence of the deposition angle  $\alpha$  in the resultant angle  $\beta$  due to atomic self-shadowing effect [20]

The OAD growth is explained as follows: the initial arrival of depositing material produces a random distribution of nuclei on the surface of the substrate. These nuclei grow, casting shadows across the substrate in the direction of the material flux giving rise to nanocolumns. The columns develop shadowing smaller neighbors behind them and hindering their growth. If the mobility of the atoms on the surface is limited, there is no growth in the shadowed regions. This results in the growth of porous tilted nanocolumns. In the direction perpendicular to the vapor flux, this shadowing effect does not take place and the columns gather forming bundles. This is known as “bundling association” and leads to an anisotropic distribution of material that is characteristic of this kind of growth [63].

For this work, a Ti-Al-C multilayer approach deposited at oblique angle deposition was adopted at TU Ilmenau. The necessary time and power were calculated according to the stoichiometric ratio of these three elements in  $\text{Ti}_2\text{AlC}$  and  $\text{Ti}_3\text{AlC}_2$  MAX phases, also considering their theoretical densities. The power was set to 50 W each target and the sputtering time was set to  $t_{\text{Ti}} = 1 \text{ min } 25 \text{ s}$ ,  $t_{\text{Al}} = 24 \text{ s}$  and  $t_{\text{C}} = 1 \text{ min } 25 \text{ s}$  for each



cycle. The periodical Ti-Al-C cycle has been repeated 22 times resulting in a total thickness of  $\sim 500$  nm. During the multiplayer deposition, a stop-and-go mode was followed [92], meaning the sample holder rotated from one target position to another one and stayed for the necessary amount of time at each individual target position. To prevent the contamination of the sample with the fellow elements in the multilayer system, a shutter was installed inside the deposition chamber, placed between the magnetrons and the rotating substrate holder.

The Ti-Al-C thin films were deposited by non-reactive magnetron sputtering from three 9 cm diameter elemental Ti, Al, and C targets. Out of the 9 cm of diameter, the sputtering ring-shaped material source diameter was calculated to 6 cm. In order to simplify the calculation of the deposition angles, the sputtering ring was observed as two-dimensional, simplifying two material source points out of it, as Figure 3.15 shows. By using L-shaped substrate holder, the substrates  $\beta$ ,  $\gamma$  and  $\delta$  were placed at an off-normal configuration respect to the material source. Furthermore, the index  $i$  or  $o$  indicates the position of the substrates in the L-shaped substrate holder: inside or outside, as Figure 3.15 shows.

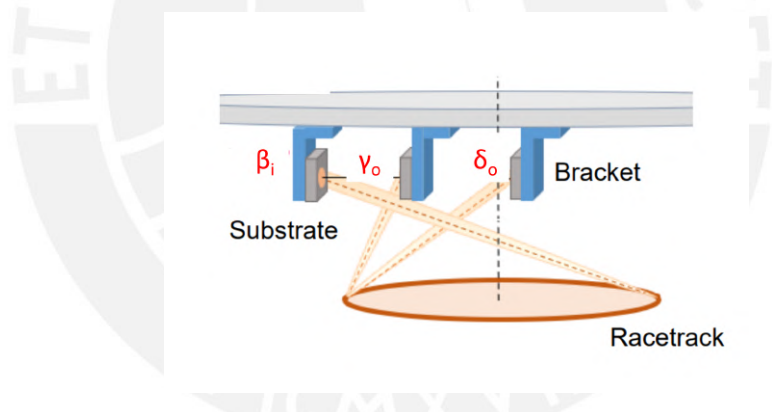


Figure 3.15 Schematic of the L-shaped substrate holder employed in this work. Notice that the material flux arriving from the target is simplified as two points to ease the angle calculation

From the incident vapor angle  $\alpha$ , the columns tilt angle  $\beta$  can be described by two different models: the known as “tangent rule”, as Equation 3.2 shows

$$\tan \alpha = 2 \tan \beta \quad (3.2)$$

which is accurate for incident vapor angles  $\alpha < 40^\circ$  [46], and the model based on geometrical considerations from two-dimensional growth simulation assuming ballistic mode and is accurate for incident angles  $\alpha > 40^\circ$  [91], often referred to as "cosine rule"

$$\beta = \alpha - \sin^{-1} \left( \frac{1 - \cos \alpha}{2} \right) \quad (3.3)$$

Although these rules can approximate the expected behavior of  $\beta$ , the actual behavior of OAD films can be disparate from the theoretical values due to several factors: By increasing e.g., the temperature or the deposition rate, the atomistic behavior of the deposited atom changes. Differences in the crystallinity of the materials can also have a significant effect on the final morphology of the nanocolumns, as well as the interaction between substrate and deposited film [113]. The base pressure of the chamber was in the mid  $10^{-6}$  mbar range and the distance substrate-to-target 5 cm. A pre-sputtering of 3 minutes with a sputtering power of 50 W was performed on each target to eliminate the oxidation and possible contamination of the surfaces of the targets. The argon flow was established at 80 sccm. The resulting time of the titanium and carbon targets were set as 1 minute and 25 seconds each. The necessary time for aluminum was set at 24 seconds. After the deposition process, the samples underwent an annealing process in pure argon atmosphere in atmospheric pressure. The heating and cooling rates were fixed at 10 K/s and 5 K/s and the holding time was 5 minutes.

Cross-section SEM images of the as deposited samples on silicon substrate produced at oblique angle deposition are exhibited in Figure 3.16. The columnar growth of the thin film is clearly distinguishable. From these cross-sectional SEM images, valuable information about the morphology can be derived, as well as the resulting thickness of the thin film. As indicated earlier, the expected thickness was 500 nm. However, the atom reorganization due to the off-normal configuration results in thinner thin films, which depend on the arrival of material on the substrate and is intricately related to the deposition angle.

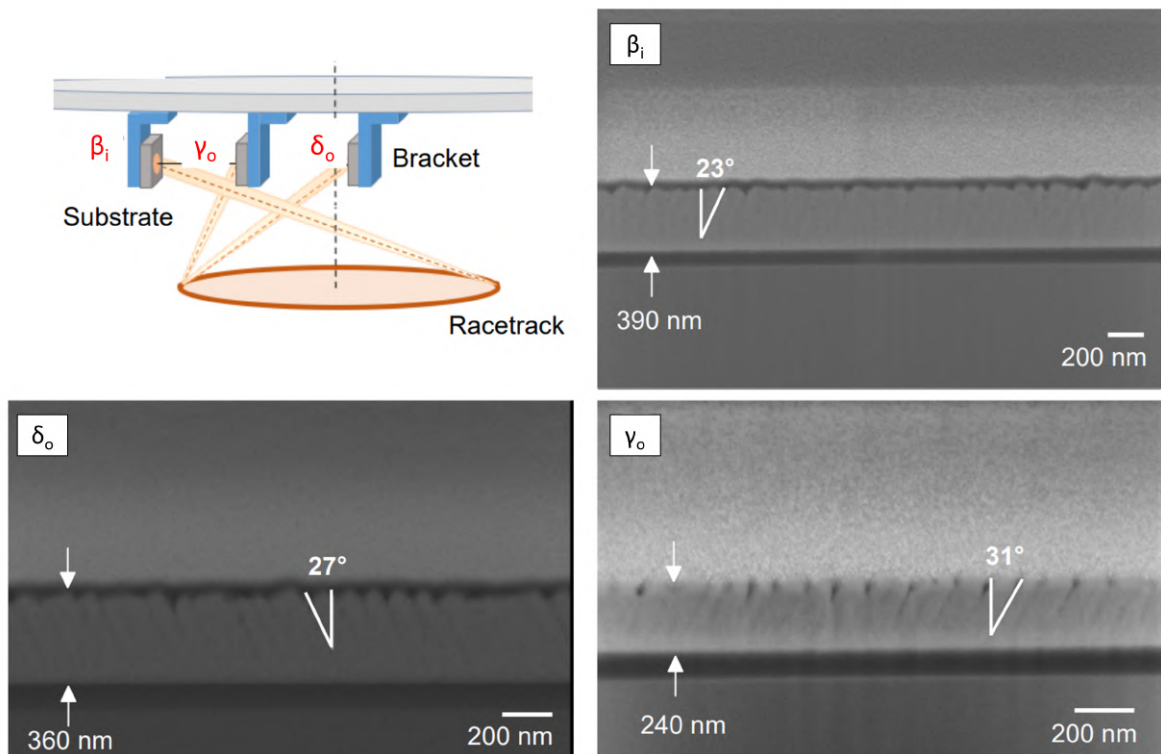


Figure 3.16 Schematic of sample holder and SEM cross-section images of samples deposited at OAD as prepared [95]

Table 3.5 shows the measured incident vapor angle  $\alpha$  and the calculated column tilt angle  $\beta$ .

Table 3.5 Incident vapor angle  $\alpha$ , theoretical and experimental tilt angle  $\beta$  of the as deposited thin films

Sample	Incident Vapor tilt angle $\alpha$	Theor. column tilt angle $\beta$ (Tangent rule)	Theor. column tilt angle $\beta$ (Cosine rule)	Exp. column tilt angle $\beta$ (in Fig. 3.16)
$\beta_i$	$36^\circ$	$19^\circ$	$29^\circ$	$23^\circ$
$\gamma_o$	$60^\circ$	$40^\circ$	$45^\circ$	$31^\circ$
$\delta_o$	$55^\circ$	$35^\circ$	$42^\circ$	$27^\circ$

Comparing both theoretical values it can be observed that the one calculated by the tangent rule approximates more to the experimental value than the one taking into consideration the ballistic mode. However, a considerable variation of the expected value is observed for all three samples.

Figure 3.17 shows SEM top-view images of the as deposited samples on silicon

substrate produced at OAD. The so-called bundling association of the nanocolumns can be clearly distinguished. With increasing column tilt angle  $\beta$ , the porosity of the thin film increases. Therefore, the connection of the nanocolumns also decreases, until the formation of a closed and uniform thin film at  $0^\circ$  (normal configuration) is achieved (Figure 3.17a).

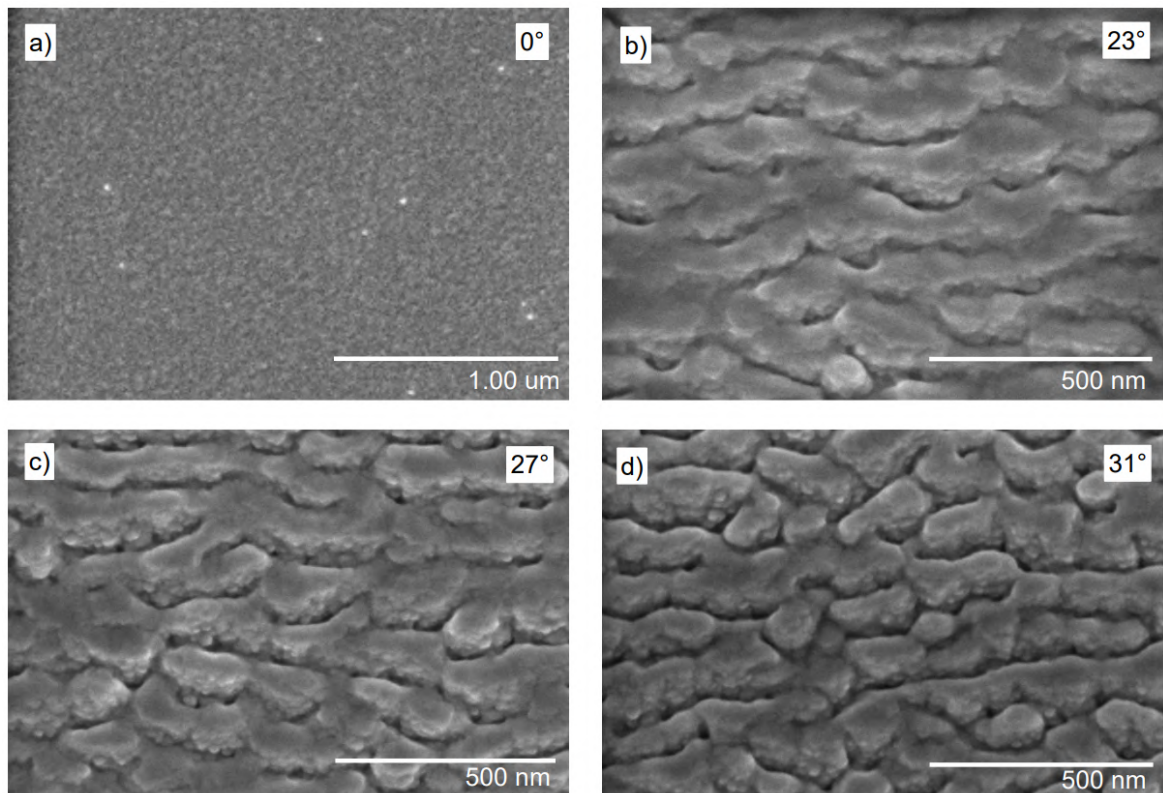


Figure 3.17 Top-view SEM images of a) MAX phase thin film deposited at normal-configuration, and b-d) OAD deposited thin films with different column tilt angle as prepared [95]

In order to gain a closer insights into the morphological evolution of the thin films during heat treatment, the annealed coating were also characterized by SEM top-view images. Figure 3.18 shows top-view SEM images of the OAD deposited samples at different annealing temperatures.

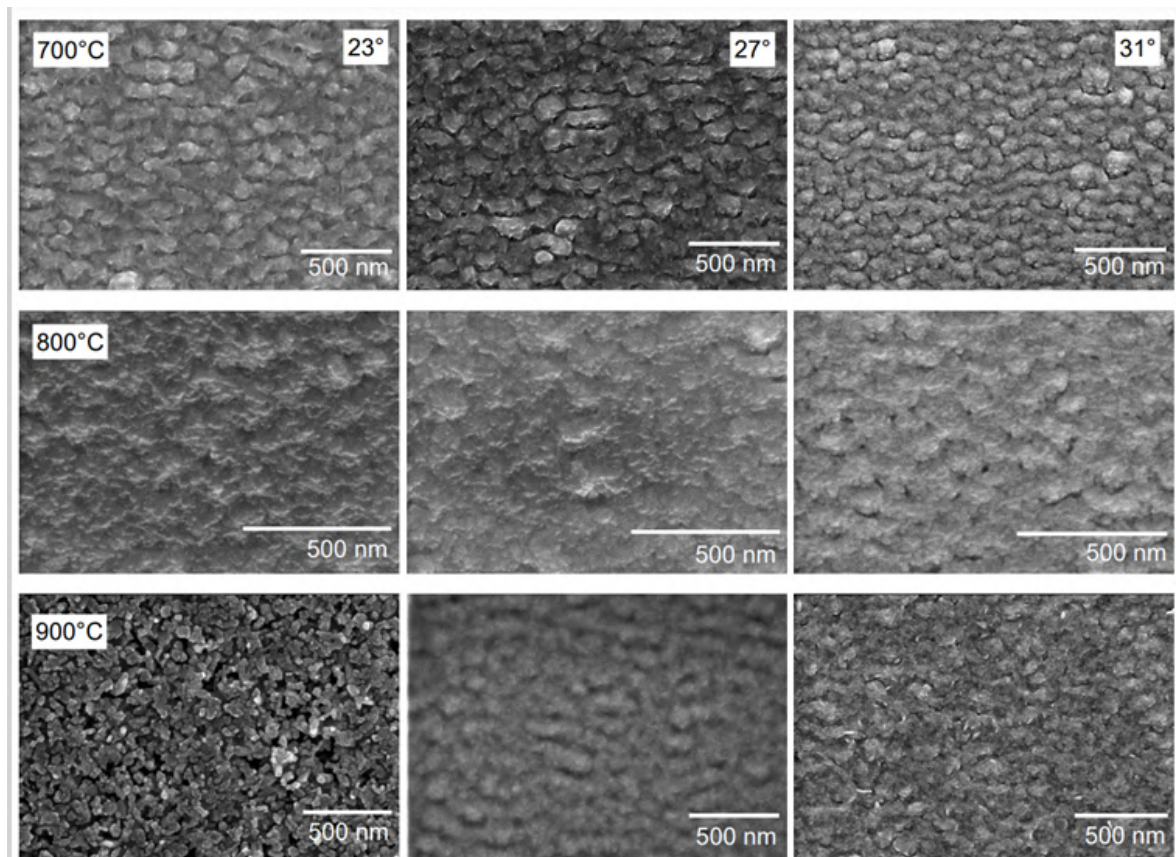


Figure 3.18 Top-view SEM images of OAD deposited thin films with different column tilt angles at different annealing temperatures using a RTP oven [95]

The morphological evolution of the columnar structure and the development of the bundling association is clearly perceived. As shown, after annealing the thin films show a completely different nanostructure with a granular and rougher shape. As the annealing temperature increases, the columnar morphology converts into a more granular shape. When annealed at 700 °C, the samples still exhibit a columnar nanostructure with shaped bundling and differentiable chapter. At 800 °C the defined nanocolumns combine and a phase transformation can be intuit. At 900 °C, the columnar morphology is not noticeable since diffusion processes reorganize the atoms and creates the  $Ti_3AlC_2$  MAX phase. The chemical composition of the oblique angle deposited thin films was examined by EDX for several angles of incidence and annealing temperatures, as Figure 3.19 and Table 3.6 show.



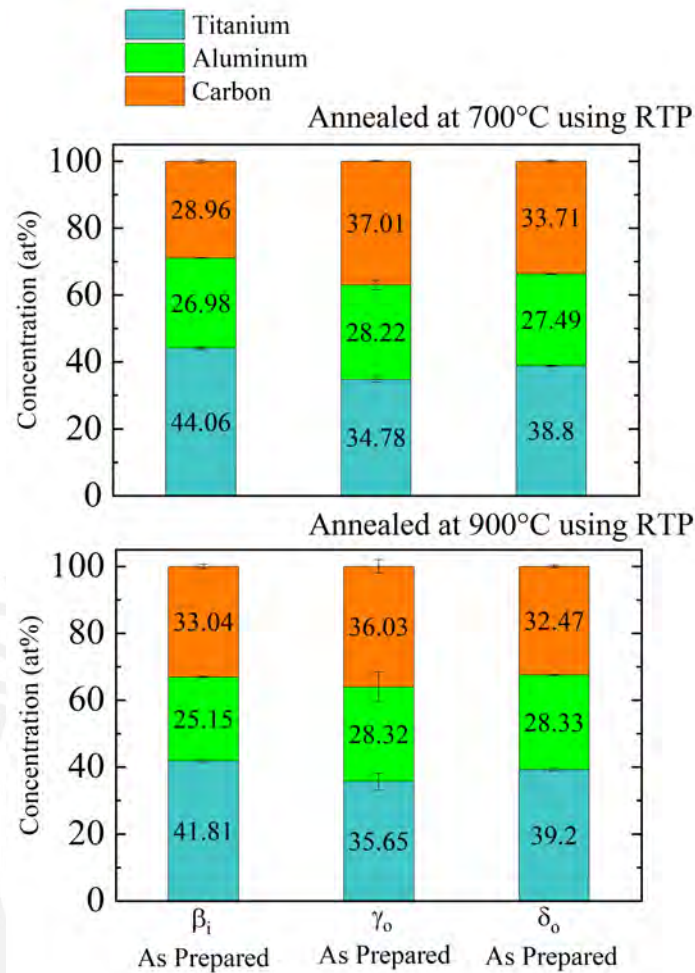


Figure 3.19 Chemical composition of MAX phases deposited at oblique angle configuration ( $\beta \sim 23^\circ$ ,  $\gamma \sim 31^\circ$  and  $\delta \sim 27^\circ$ ) and annealed at 700 °C and 900 °C by RTP process

Table 3.6 Ti:Al ratio of nanostructured MAX phases as prepared

Sample	Nanostructured MAX phase annealed at 700 °C RTP (Ti <sub>2</sub> AlC)	Nanostructured MAX phase annealed at 900 °C RTP (Ti <sub>2</sub> AlC and Ti <sub>3</sub> AlC <sub>2</sub> )
$\beta_i$ (23°)	1.63	1.66
$\gamma_o$ (31°)	1.41	1.38
$\delta_o$ (27°)	1.23	1.26

For all angles, the stoichiometric relation between the three elements coincides with the required composition for the formation of MAX phase, including the aluminum excess pointed above. The sample with the highest column tilt angle shows the lowest

Ti:Al ratio for both temperatures. This effect can be explained by the geometrical position of the sample in the deposition chamber. Since the sample labelled as  $\beta$  was placed on the inside of the substrate holder, the material flux arrives more homogenic than on the outer side of the L-shaped substrate holder (samples  $\delta$  and  $\gamma$ ). Therefore, material flux arrives with a similar behavior than the one theoretically calculated. The lower the incident vapor angle, the lower the Ti:Al ratio, which implies the inhomogeneity of the material arrival on the sample and the difference between the theoretical and the expected chemical composition.

The microstructure of the samples deposited a different incident vapor angles is shown in Figure 3.20 by the XRD spectra.

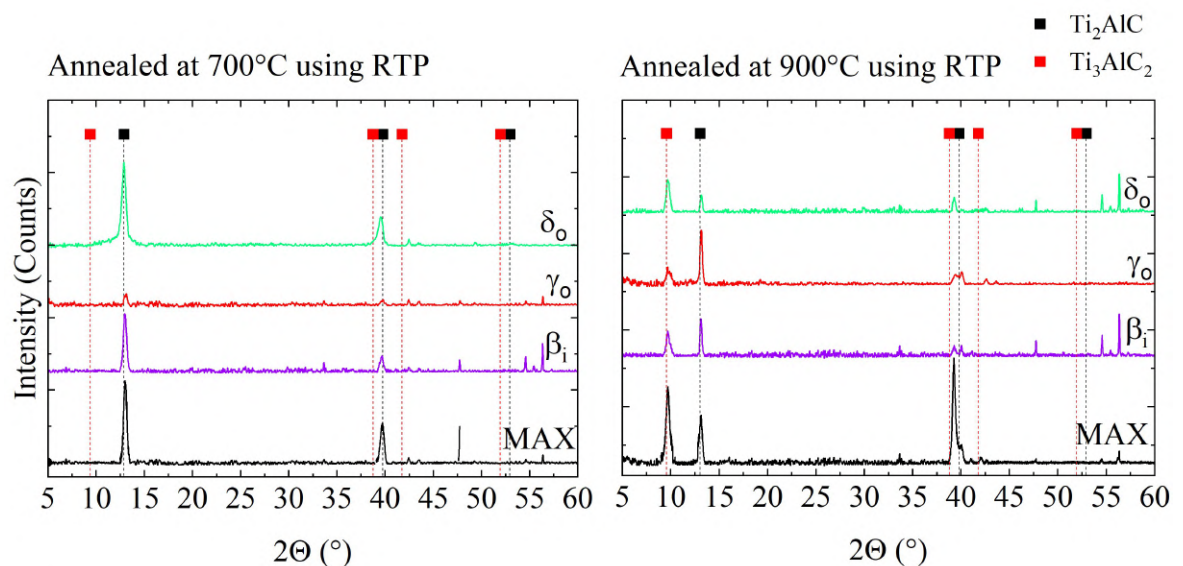


Figure 3.20 BB-XRD diffractograms of oblique angle deposited MAX phase thin films ( $\beta \sim 23^\circ$ ,  $\gamma \sim 31^\circ$  and  $\delta \sim 27^\circ$ ) and reference MAX phase sample annealed at different temperatures using RTP

When annealed at  $700^\circ\text{C}$ , the nanostructured samples exhibit its characteristic peaks at  $13^\circ$  (002) and  $39^\circ$  (103), which indicate the presence of  $\text{Ti}_2\text{AlC}$  MAX phase (PDF 29-0095). For  $900^\circ\text{C}$ , the characteristic (002) peak of MAX phase  $\text{Ti}_2\text{AlC}$  at  $13^\circ$  can be still appreciated, but with an inferior intensity, which traduces in a lower FWHM value (0.250). This decrease in the FWHM value implies a phase transformation of  $\text{Ti}_2\text{AlC}$  to  $\text{Ti}_3\text{AlC}_2$  phase, which (002) peak can be found at around  $9^\circ$  (PDF 52-08759), due to the increasing temperature. As it can be observed, both MAX phases coexist when annealing at  $900^\circ\text{C}$ , whereas at  $700^\circ\text{C}$  only the  $\text{Ti}_2\text{AlC}$  MAX phase is formed.

Raman spectroscopy analysis was performed to corroborate the microstructure and phase evolution of  $\text{Ti}_2\text{AlC}$  MAX phase to  $\text{Ti}_3\text{AlC}_2$  phase as Figure 3.21 shows.



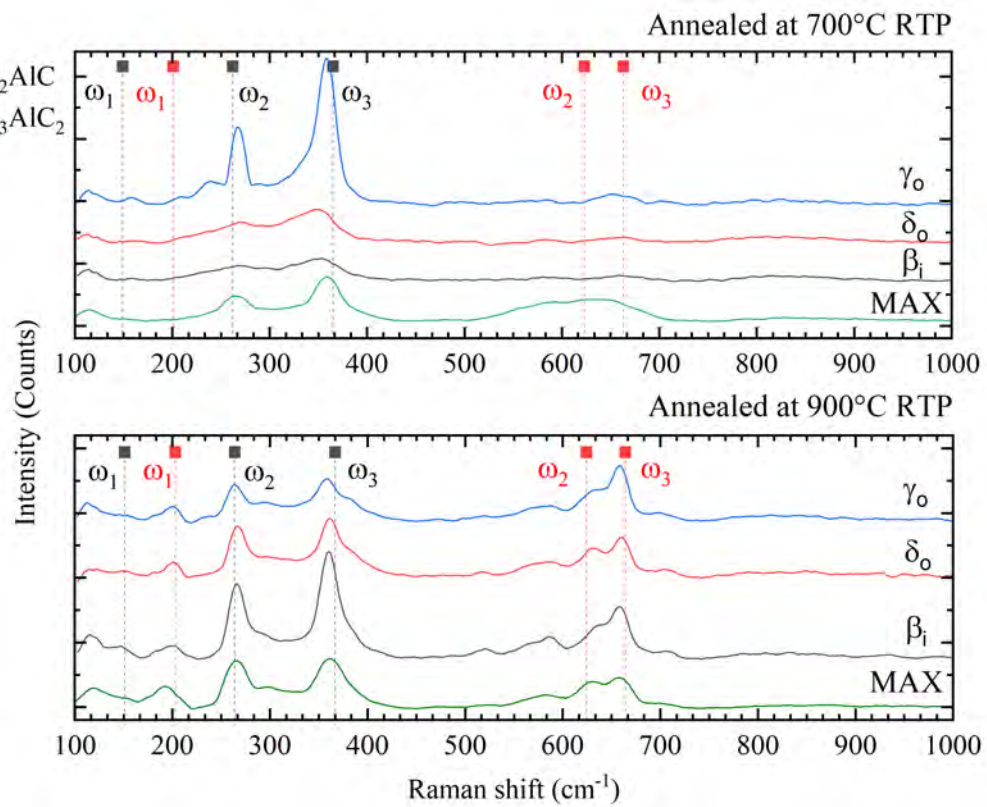


Figure 3.21 Raman spectra of oblique angle deposited thin films ( $\beta \sim 23^\circ$ ,  $\gamma \sim 31^\circ$  and  $\delta \sim 27^\circ$ ) annealed at  $700^\circ\text{C}$  and  $900^\circ\text{C}$  using RTP process

The spectrum of  $\text{Ti}_2\text{AlC}$  thin film annealed at  $700^\circ\text{C}$  by RTP is consistent with the previous results, where the Raman vibration modes  $E_{1g}$ ,  $E_{2g}$  and  $A_{1g}$  are located at  $\omega_2 = 258.1\text{ cm}^{-1}$  and  $\omega_3 = 348.7\text{ cm}^{-1}$  respectively. The Raman active modes of the  $\text{Ti}_3\text{AlC}_2$  MAX phase at  $\omega_2 = 654\text{ cm}^{-1}$  begin to become visible in the  $900^\circ\text{C}$  annealed sample. Both MAX phases can be observed, whereas the phase shift from the  $\text{Ti}_2\text{AlC}$  MAX phase to  $\text{Ti}_3\text{AlC}_2$  is fulfilled at temperatures above  $900^\circ\text{C}$ .

## 4 Selective HF Etching for MXenes synthesis

### 4.1 HF Etching of MAX phase thin films

Before further analyzing the nanostructured MAX phases deposited at OAD with various column tilt angles, and their reaction to selective HF wet etching, referential MAX phases deposited at normal-configuration ( $0^\circ$ ) and annealed at  $700^\circ\text{C}$  and  $900^\circ\text{C}$  using RTP were etched under the same conditions and examined. These analysis gets an insight about the etching mechanism independently from the deposition angle and tries to explain the formation mechanism of MXenes.

The samples deposited as Section 3.2 explains were immersed in 1% HF solution for 2 hours, as Section 2.8 indicates, and characterized using various methods including SEM, EDX to analyze the chemical composition, as well as XRD and Raman spectroscopy, to unravel the possible morphology changes in the thin films. During the etching process, whenever the MAX thin films came in touch with aqueous HF etchant, bubbles, presumably  $\text{H}_2$ , were observed. After 2 hours immersed in HF etching solution, both samples rupture and delaminate from the substrate. This delamination was a result of the various cracking of the surface, as observed in Figure 4.1, where a SEM top-view image of samples annealed at  $900^\circ\text{C}$  after 2 h HF etching is shown.

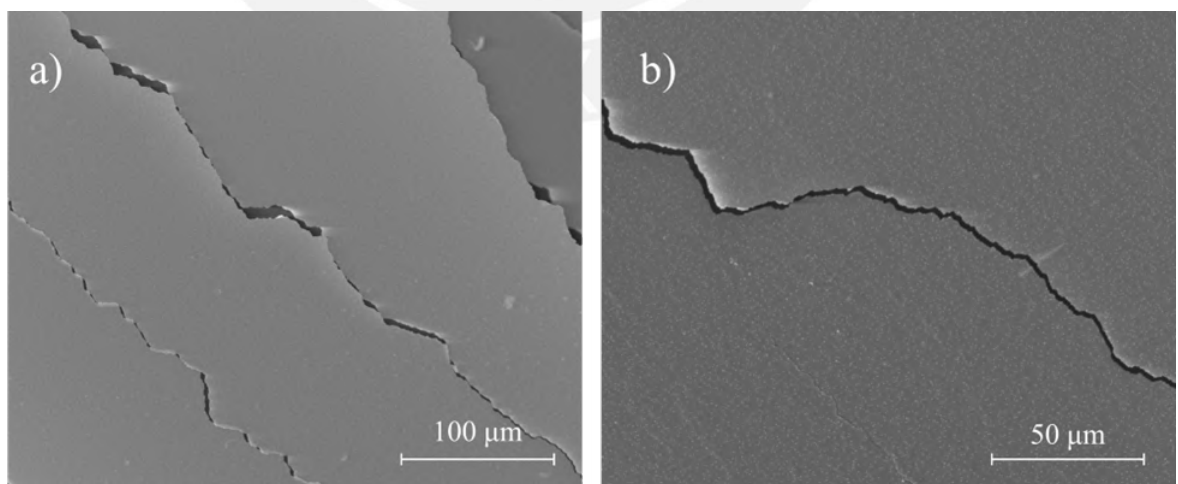


Figure 4.1 Top-view SEM images of surface of MAX phase ( $\text{Ti}_2\text{AlC}$  and  $\text{Ti}_3\text{AlC}_2$ ) deposited at normal configuration and annealed at  $900^\circ\text{C}$  by RTP process after 2 h selective etching a) at 800x b) at 1600x

This delamination process can be explained by the  $\text{Si}_3\text{N}_4$  protective coating, which can be found in the interface between the substrate and the thin film to prevent the silicon atoms to diffuse into the MAX phase thin film [96], as well as the  $\text{SiO}_2$  thin film of the oxidized silicon substrate. Both  $\text{SiO}_2$  and  $\text{Si}_3\text{N}_4$  present low chemical stability towards HF etching [64]. When the HF etching solution arrives on the substrate surface, the protective  $\text{Si}_3\text{N}_4$  and the created  $\text{SiO}_2$  thin films get etched and the adhesion of the thin film onto the substrate is lost, delaminating it.

Taking a closer look at the surface of the sample after the selective HF etching, single drops scattered arbitrarily are observed. This spots are also found in the sample with MAX phase as deposited, as Figure 4.2 shows.

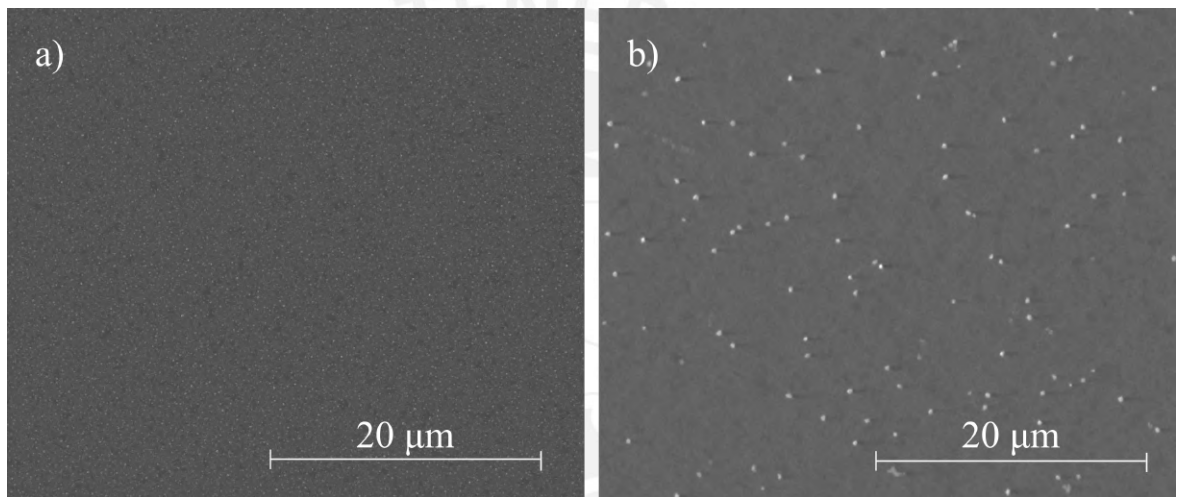
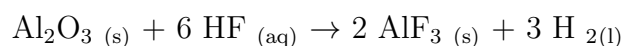


Figure 4.2 Top-view SEM image of MAX phase ( $\text{Ti}_2\text{AlC}$  and  $\text{Ti}_3\text{AlC}_2$ ) thin film surface annealed at  $900^\circ\text{C}$  by RTP process a) as deposited and b) after 2 hours HF selective etching

In the as deposited state, smaller single crystals can be found. Various authors [77] suggest the formation of  $\text{Al}_2\text{O}_3$  on the surface due to the aluminum excess internationally achieved by the deposition parameters, and its tendency to oxidize to alumina ( $\text{Al}_2\text{O}_3$ ). The  $\text{Al}_2\text{O}_3$  concentration generally increases at higher annealing temperatures ( $950^\circ\text{C}$ - $1000^\circ\text{C}$ ) from around 1 at% to 5-10 at% [96], and therefore can only be found in the samples annealed at  $900^\circ\text{C}$ , where  $\text{Ti}_3\text{AlC}_2$  MAX phase is created.

In the etched sample these spots considerably increase its size. Since  $\text{Al}_2\text{O}_3$  has a low stability towards HF etching, the creation of  $\text{AlF}_3$  crystals can be a plausible explanation for the presence of spots on the surface on the sample. The reaction [79], defined as a neutralization since  $\text{Al}_2\text{O}_3$  is a base and HF is an acid, is reported as



where  $AlF_3$  is reported as a white crystalline structures [4]. Furthermore, the etching mechanism has this by-product as a result of the  $Ti_2AlC$  etching with HF solution [103] thus the presence of this compound is expected. However, since an EDX analysis of the single dots is not possible due to the limited resolution of this characterization technique, the exact composition cannot be determined. Nevertheless, these crystalline structure on the substrate surface does not influence the etching process of the thin film whose morphology changes after the selective HF etching from MAX phase to MXene.

To analyze the aluminum concentration and the chemical composition, an EDX analysis of the thin films was performed, as Figure 4.3 shows, where the as deposited samples are compared with the after HF treated samples to unmask the concentration change derived from the HF etching. Table 4.1 shows the Ti:Al ratio for both samples as deposited and after 2 h HF etching.

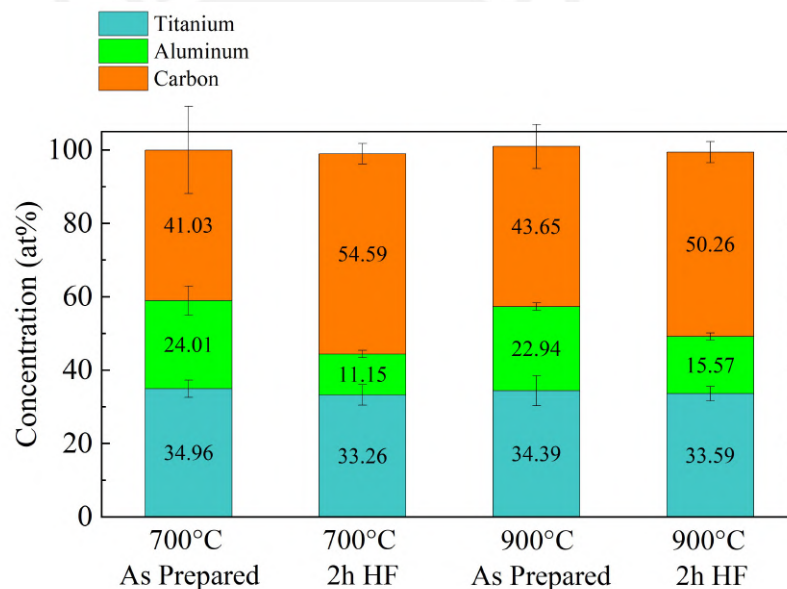


Figure 4.3 EDX analysis of MAX phases as deposited and after 2 hours selective HF etching. The ratio Ti:Al of both samples is indicated in the Table 4.1

Table 4.1 Ti:Al ratio of MAX phase thin film annealed at 700 °C and 900 °C by RTP process as prepared and after 2 h HF etching

Sample	Ti:Al ratio As Deposited	Ti:Al ratio After 2 h HF etching
MAX phase annealed at 700 °C ( $Ti_2AlC$ )	1.45	2.98
MAX phase annealed at 900 °C ( $Ti_2AlC$ and $Ti_3AlC_2$ )	1.50	2.16

The Ti:Al ratio decreases from the ideal ratio to creation MAX phases of  $\sim 1.2$  as deposited to  $\sim 3$  after etching, implicating a decrease in the aluminum concentration. However, the aluminum concentration still is excessive for the creation of pure MXene thin films. As a comparison, some authors report MXene powders produced from MAX precursors with an aluminum concentration of around 0.14 at% [52] whereas in the case of this work the concentration does not decrease lower than 10 at% in both samples. As a conclusion, the creation of pure MXenes is discarded. An incomplete etching of the MAX phases could result in a multilayer system, where an etched MXene film is located on top of the MAX thin film, which remains intact, as Figure 4.4 shows.

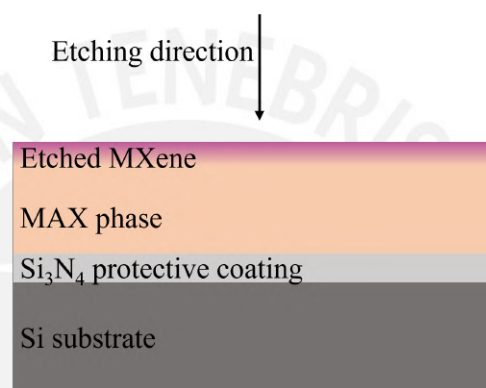


Figure 4.4 Schematic of resulting morphology of MAX thin film phases after HF selective etching. Notice that the  $\text{SiO}_2$  thin film is not depicted as it is not specified by the substrate producer

To confirm the hypothesis that the etching does not expand over the thickness of the MAX phase, but only the first nanometres transform into MXene, a GI-XRD analysis with variable X-Ray incidence angle  $\theta$  is performed. The higher the incidence angle  $\theta$ , the higher the penetration depth of the X-rays in the material [89]. By depicting the XRD diffractogram as a function of the incidence angle  $\theta$ , the evolution of the morphology over the thin film depth can be analyzed. Since the  $\text{Ti}_3\text{AlC}_2$  is less resistant to the HF etching than the  $\text{Ti}_2\text{AlC}$ , an analysis of its diffractogram brings to light the possible morphological changes. Furthermore, the  $\text{Ti}_2\text{AlC}$  diffractogram only presents one characteristic peak and therefore its analysis will be insufficient.

Every hexagonal MAX phase crystal structure possesses two defining lattice parameters  $a$  and  $c$ . The  $a$  lattice parameter is related to the width of the crystal and is determined by the (110) peak, which is located at  $\sim 49^\circ$ . The  $c$  lattice parameter is related to the height of the unit cell and is defined by the (002) peak, found between  $5^\circ$  and  $15^\circ$  depending on the MAX phase [84]. One of the main indicators for the successful etching of aluminum atoms from  $700^\circ\text{C}$  and  $900^\circ\text{C}$  annealed MAX phases is



the shifting of the (002) peak located at  $\sim 9^\circ$  ( $\text{Ti}_2\text{AlC}$ ) and  $\sim 13^\circ$  ( $\text{Ti}_3\text{AlC}_2$ ) respectively towards lower angles [88]. This effect can be explained by the removal of the aluminum atoms in the MAX phases hexagonal crystalline structure. The functional groups e.g., -F or -Cl in the etching solutions replace the aluminum atoms between the MXene sheets and increase the interlayer spacing [84]. This increase traduces into a lower peak angle (following Braggs equation). Figure 4.5 shows the characteristic peaks in the XRD spectra of the MAX phase annealed at  $900^\circ\text{C}$  ( $\text{Ti}_2\text{AlC}$  and  $\text{Ti}_3\text{AlC}_2$ ) as prepared and after HF etching.

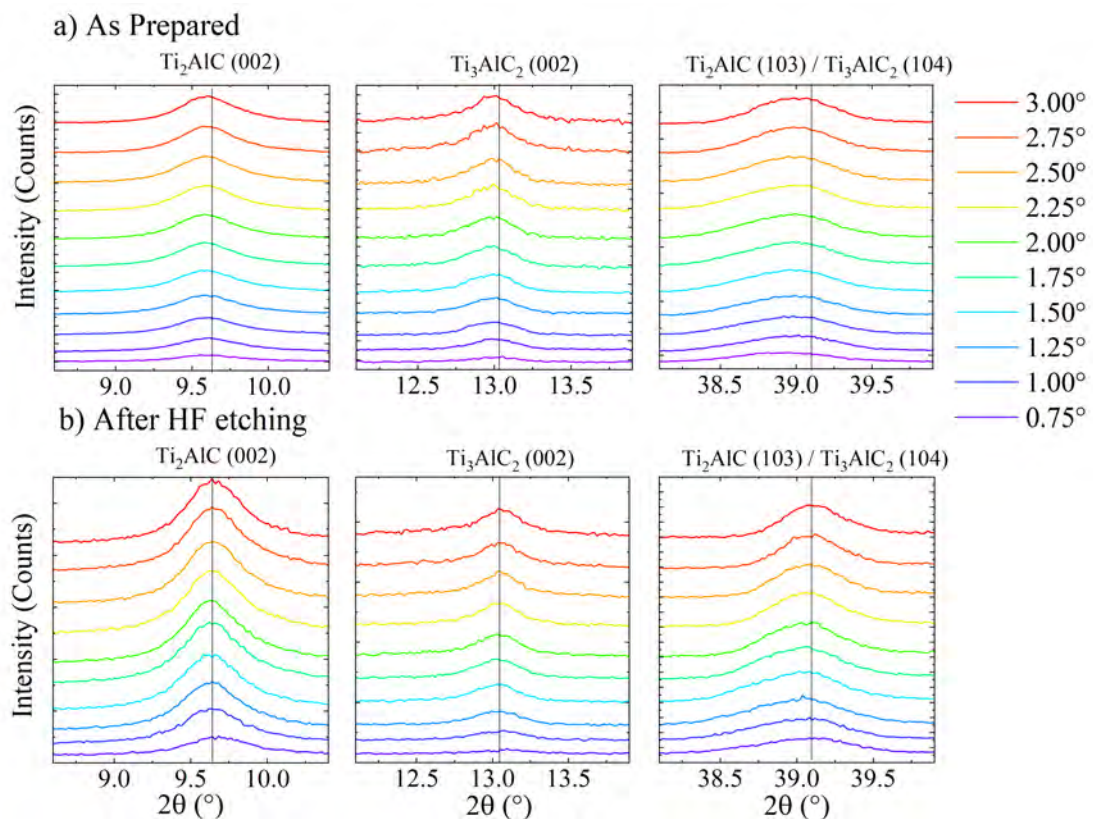


Figure 4.5 GI-XRD diffractogram sections of MAX phase thin film annealed at  $900^\circ\text{C}$  a) as prepared and b) after 2 hours HF etching with variable incident angle ( $0.75^\circ$  -  $3^\circ$ ). The diffractograms can be found in the annex.

Since the MAX phase is not completely etched to MXene, the partial downshifting of the (002) peak cannot be appreciated with bare eye. For this purpose, the FWHM value as a function of the incident angle  $\theta$  has to be analyzed. When etching the sample with HF, a percentage of the thin films transforms from MAX phase to MXene. The sample does not exhibit pure MAX phase anymore, but an overlapping of MXene on top of the MAX phase. When increasing the MXene share, the corresponding (002) peak shifts towards lower angles, increasing the width of the peak, since MAX phase

is still present and its peak remains immovable. As a result, with increasing MXene share, the FWHM value increases correspondingly. The FWHM value and the peak position of the spectra were analyzed, and depicted as a function of the incidence angle, as Figure 4.6 and Figure 4.7 shows.

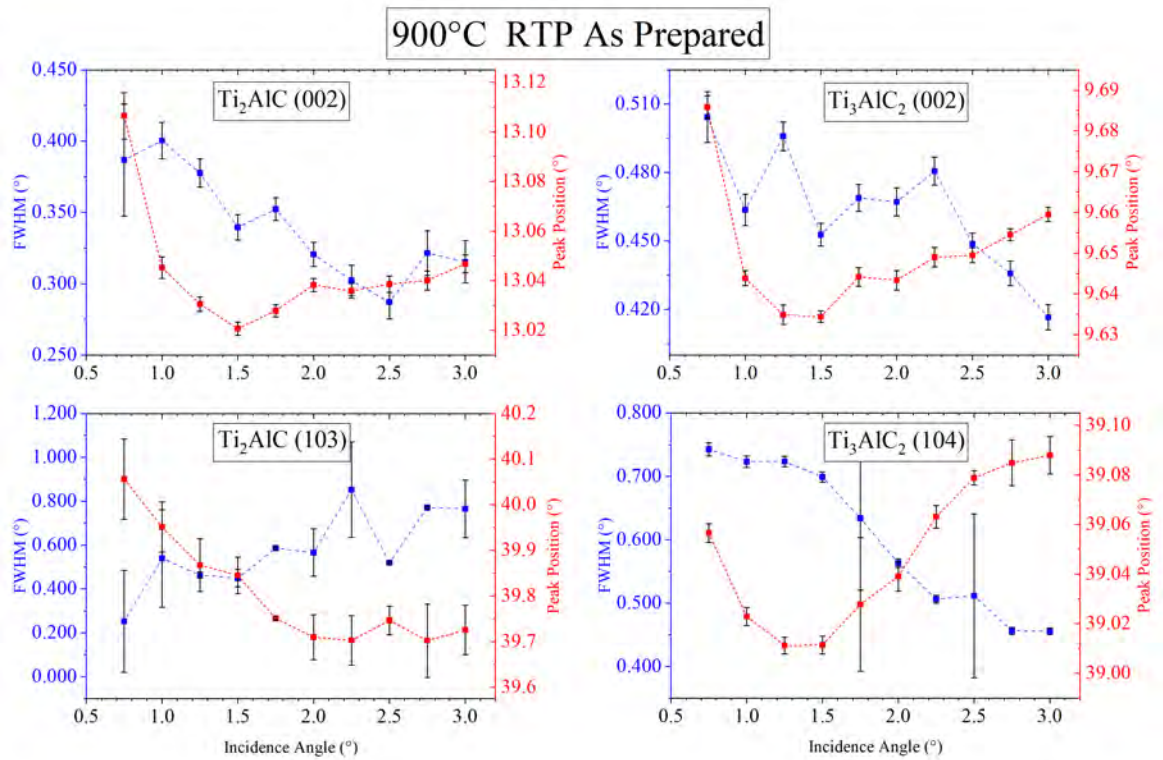


Figure 4.6 FWHM and peak position analysis of the XRD spectrum of MAX phases annealed at 900 °C as prepared with variable incident angle (0.5° - 3°)



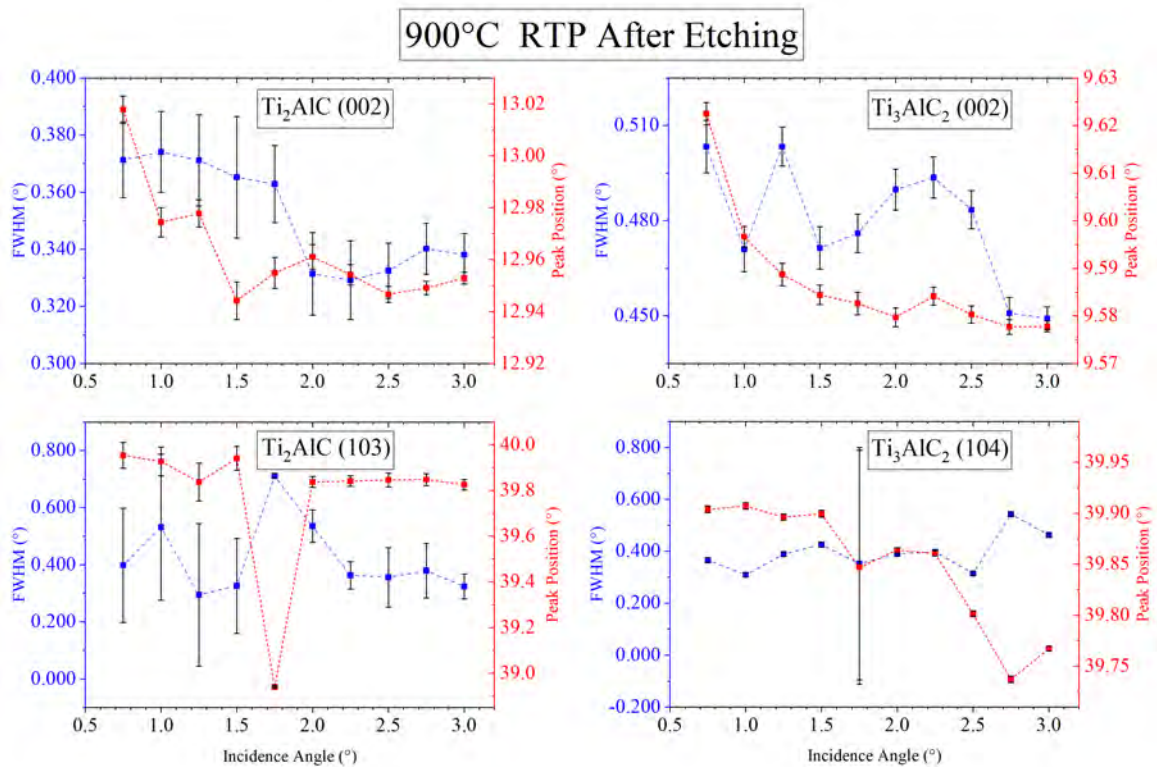


Figure 4.7 FWHM and peak position analysis of the XRD spectrum of MAX phases annealed at 900 °C after HF etching with variable incident angle (0.5° - 3°)

Notice that the peak found at  $\sim 39^\circ$  consists of two peaks from the two co-existing MAX phases  $\text{Ti}_2\text{AlC}$  (103) and  $\text{Ti}_3\text{AlC}_2$  (104). The results of this experiment are not conclusive due to several factors. Firstly, previous results show inhomogeneity of the sample when annealed at 900 °C [96]. When varying the incidence angle, the penetration depth changes accordingly. Since the sample is not homogeneous, the result has to be looked at carefully. Furthermore, the annealing RTP process at 900 °C with relatively fast heating and cooling rates, and the subsequent HF etching process could bring residual stress to the thin film, which has an influence on the peak position and FWHM value. Generally, when observing the stress course over the depth of a material, different points show different stress values, which could reflect in different FWHM values. A possible hypothesis could locate the spot with the highest residual stress in the depth of the minimum observed in Figures 4.6 and 4.7. Lastly, the deposition parameters position the sample in the Zone 1 in the Thornton model. In this zone, crystallites in the thin film/substrate interface tend to be smaller. This inhomogeneous columnar size growth could reflect in an inhomogeneous FWHM value and peak position over the penetration depth, like depicted in this Figures. To further analyze this effect and

establish a reliable hypothesis, a cross-section view of the sample would be necessary to observe the rearrangements of the atoms due to the annealing and etching processes. This cross-section could be carried by a Transmission Electron Microscope (TEM) and is listed in the outlook for further experiments.

One of the difficulties in this experiment is the delamination of the samples before completely etching the aluminum atoms from the MAX phase. Therefore, a further experiment was conducted in order to improve the adhesion from the thin film to the substrate. Before the etching, a sample annealed at 700 °C and a sample annealed at 900 °C using RTP at the TU Ilmenau were heated to 400 °C for 2 hours in vacuum using a tubular alumina oven. This additional thermal process could rearrange the atoms in the interface and improve the adhesion. Henceforth, this samples heated will be named after the annealing temperature to form the  $\text{Ti}_2\text{AlC}$  and  $\text{Ti}_3\text{AlC}_2$  MAX phases using an RTP oven (700 °C or 900 °C respectively) followed by the term @400 °C 2 h, which indicates the subsequent thermal process carried using the tubular oven.

To analyze the morphological changes of the etched samples and the possible influence of the previous annealing process at 400 °C, XRD analysis using Bragg Brentano configuration was conducted, as Figure 4.8 shows.

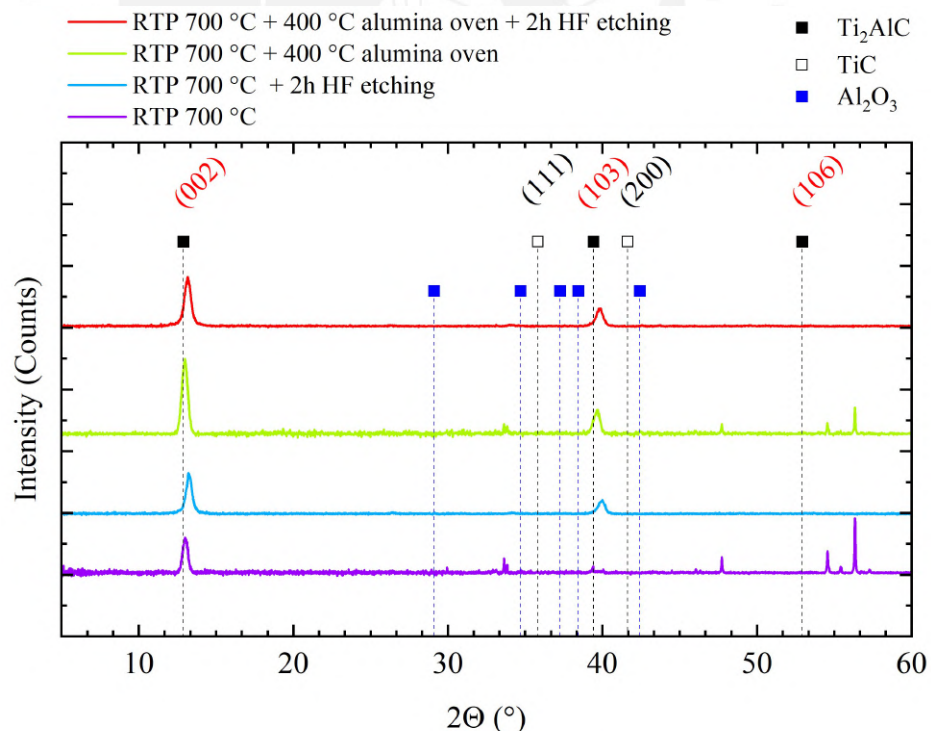


Figure 4.8 BB-XRD diffractogram of MAX phases annealed at 700 °C by RTP as deposited (violet) and after 2 hours HF etching (blue); and annealed at 700 °C with a subsequent 400 °C heat treatment (green) and after 2 hours HF etching (red)

Generally, one of the main indicators for the successful etching of aluminum atoms from MAX phases to pure MXenes is the disappearance of the diffraction peak located at  $39^\circ$ . However, the MXene thickness percentage in the total thin film could be seen as comparatively small when compared to the total thickness of the thin film. The remain of this peak after the etching mechanism does not implicate an unsuccessful etching process. An expected effect could be a decrease in its intensity due to the formation of MXene from the MAX phase.

Furthermore, the cleaning method of the resulting MXene plays a crucial role in the resulting morphology of the thin film [44][84]. When cleaning the sample after the HF etching process, functional groups found in the cleaning solution can additionally alter the morphology of the thin film [84]. Since this relationship is yet to be established, the fact that the peak at  $39^\circ$  does not disappear cannot be taken as an absolute indicator as explained before.

As mentioned aforehand, another indicator for this transformation is the down-shifting of the (002) peak to a lower angle [88] due to the increase of interlayer spacing of the MXene particles as a consequence of the intercalation of the functional groups. The lack of this shifting in our diffraction pattern shows that the aluminum atoms were not completely removed from the MAX phase, as indicated earlier, but only on the surface of the sample to create the MXene thin film. On the contrary, in Figure 4.8 an up-shifting of the (002) characteristic peaks can be observed. This effect is reported by various authors [60], as the MXene nanosheets decrease its distance due to the lack of aluminum atoms between them. Again, the subsequent MXene thin film treatment such as cleaning method [84][5], and even drying method [35] play an important role in the resulting morphology.

To further analyze the obtained diffractogram, Table 4.2 and Table 4.3 show the FWHM values and peak position of both characteristic peaks (002) located at  $13^\circ$  and (103) located at  $39^\circ$  of MAX phases annealed at  $700^\circ\text{C}$  by RTP process ( $\text{Ti}_2\text{AlC}$ ) and MAX phases annealed at  $700^\circ\text{C}$  by RTP process ( $\text{Ti}_2\text{AlC}$ ) with a subsequent thermal process at  $400^\circ\text{C}$  for 2 hours.

Table 4.2 Peak position of MAX phases annealed at 700 °C by RTP process and MAX phases annealed at 700 °C by RTP process with a subsequent thermal process at 400 °C for 2 hours, which peaks are located at  $2\theta \sim 13^\circ$  and  $2\theta \sim 39^\circ$  and obtained from Figure 4.8. Difference between the peak position as deposited and after HF etching

Sample	Peak Position As Prepared	Peak Position After Etching	Difference
700 °C RTP	$13.010^\circ \pm 0.426$	$13.259^\circ \pm 0.145$	0.249
	$39.701^\circ \pm 0.137$	$39.949^\circ \pm 0.967$	0.248
700 °C RTP 400 °C 2 h	$13.169^\circ \pm 0.263$	$13.637^\circ \pm 0.351$	0.468
	$39.630^\circ \pm 0.656$	$39.824^\circ \pm 0.54$	0.194

Table 4.3 FWHM of MAX phases annealed at 700 °C by RTP process and MAX phases annealed at 700 °C by RTP process with a subsequent thermal process at 400 °C for 2 hours, which peaks are located at  $2\theta \sim 13^\circ$  and  $2\theta \sim 39^\circ$  and obtained from Figure 4.8. Difference between the FWHM value as deposited and after HF etching

Sample	FWHM As Prepared	FWHM After Etching	$\Delta$ FWHM Difference
700 °C RTP	$0.403 \pm 0.025$	$0.425 \pm 0.058$	0.022
	$0.467 \pm 0.039$	$0.499 \pm 0.084$	0.032
700 °C RTP 400 °C 2 h	$0.450 \pm 0.097$	$0.472 \pm 0.095$	0.022
	$0.491 \pm 0.085$	$0.525 \pm 0.0874$	0.034

In both samples, the FWHM values increase after the etching process. This increase in the width of the peaks indicates a partial transformation of the MAX phase in MXene, as previously explained. An additional aspect to this widening of the peaks is the possibility of residual stress due to the HF etching process. As observed, the distances between the crystalline planes increase or decrease as a result of the removal of the aluminum atoms and hence stresses are induced in the material [89]. This residual stresses influence the diffraction patterns and have to be considered. Further experiments would be necessary to analyze this question, such as a Rietveld Refinement Analysis. However, in this thesis this property will not be further discussed.

A Raman analysis was conducted to analyze the morphological changes and the partial transformation of MAX phase in MXene. Figure 4.9 shows the Raman spectra of MAX phases annealed at 700 °C as prepared and after 2 hours HF etching. Since

only  $\text{Ti}_2\text{AlC}$  phase is stable at this annealing temperature, the indicated peaks refer only to  $\text{Ti}_2\text{AlC}$  and  $\text{Ti}_2\text{C}$  vibrational modes. Additionally, the  $\text{Al}_2\text{O}_3$  vibrational modes are depicted due to the identified phase in the SEM images.

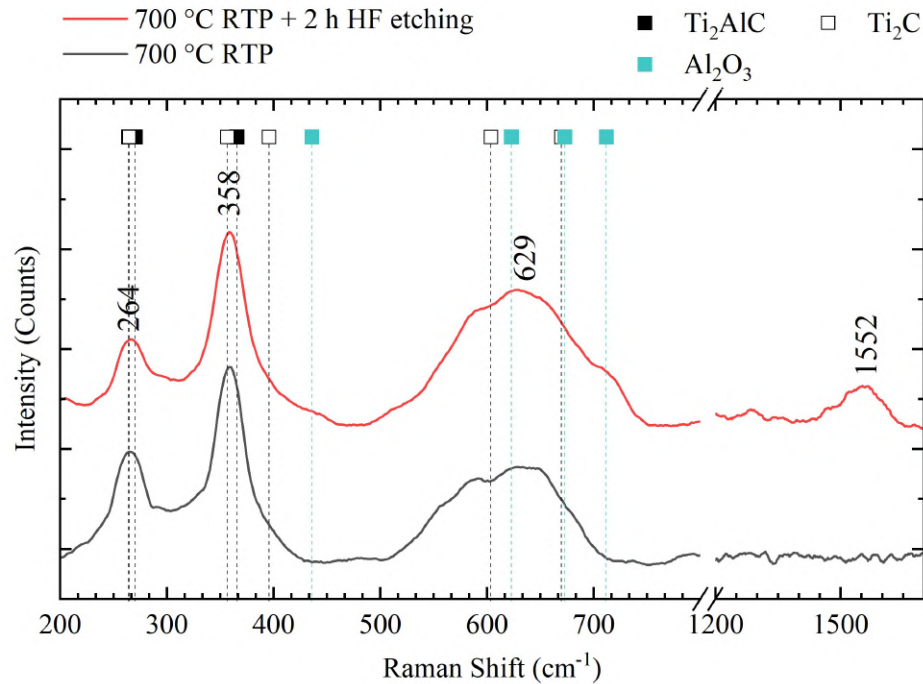


Figure 4.9 Raman spectra of MAX phases annealed at 700 °C RTP ( $\text{Ti}_2\text{AlC}$ ) as prepared and after 2 hours HF etching

The peaks found located at  $\omega_1 = 264 \text{ cm}^{-1}$  and  $\omega_2 = 358 \text{ cm}^{-1}$  correspond to the vibrational modes  $\omega_1(E_{1g})$  and  $\omega_2(A_{1g})$  of  $\text{Ti}_2\text{AlC}$  [76] respectively. This peaks are explained by the vibrations of the aluminum atoms in the thin films [24]. Since the etching process only partially attacks the sample, a large amount of thin film remains as MAX phase and therefore this peak remains mainly immovable. This implies that the  $\text{Ti}_2\text{AlC}$  phase is still present in the thin films and not completely etched. However, slight changes in the Raman spectra after the etching process reveal the start of the etching of the MAX phase to MXene on the surface of the sample. The broadening of the peaks calculated in Table 4.4 indicates a change in the composition of the sample.

Table 4.4 FWHM of characteristic peaks in Raman spectra (Figure 4.9) of MAX phases annealed at 700 °C (Ti<sub>2</sub>AlC) by RTP process as prepared and after 2 hours HF etching

Peak position	FWHM As Prepared	FWHM After Etching	Δ FWHM Difference
$\omega_1 = 264 \text{ cm}^{-1}$	$33.93 \pm 1.40$	$38.01 \pm 2.47$	4.08
$\omega_2 = 358 \text{ cm}^{-1}$	$33.93 \pm 1.40$	$38.01 \pm 2.47$	2.47
$\omega_3 = 629 \text{ cm}^{-1}$	$33.93 \pm 1.40$	$38.01 \pm 2.47$	15.98

The broadening of the peaks found at  $\omega = 358 \text{ cm}^{-1}$  towards the Ti<sub>2</sub>C peak reveals the transformation of a small amount of MAX phase Ti<sub>2</sub>AlC to its corresponding MXene Ti<sub>2</sub>C. Moreover, the peak found at  $\omega_3 = 621 \text{ cm}^{-1}$  corresponds to the Al<sub>2</sub>O<sub>3</sub> phase [55]. These Al<sub>2</sub>O<sub>3</sub> peak is visible in both samples, as prepared and after HF etching, which indicates the presence of this phase independently of the etching process. The SEM images shown previously confirm the presence of this compound only in the inner part of the sample and not on the surface.

It is noticed that one new weak peak at  $\omega_4 = 1552 \text{ cm}^{-1}$  appears in the etched sample. This peak is the in-phase vibration of the graphite (G-band), one of the two characteristic peaks of carbon-derivate compounds [31]. This effect is already reported by various authors [99][40][73]. Kaipoldayev et al. (2017) describes the structural decomposition of Ti<sub>3</sub>C<sub>2</sub> to TiO<sub>2</sub> and amorphous carbon C when adjusting the Raman laser power to higher values [73].

Figure 4.10 shows the Raman spectra of MAX phases annealed at 900 °C by RTP process as prepared and after 2 hours HF etching.



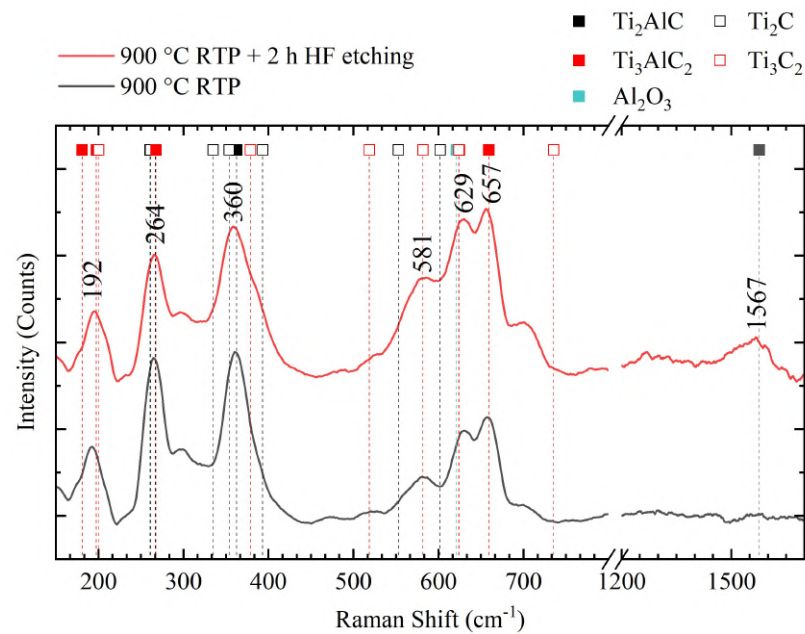


Figure 4.10 Raman spectra of MAX phases annealed at 900 °C ( $\text{Ti}_2\text{AlC}$  and  $\text{Ti}_3\text{AlC}_2$ ) by RTP process as prepared and after 2 hours HF etching

The expected  $\text{Ti}_3\text{AlC}_2$  and  $\text{Ti}_2\text{AlC}$  peaks are found in the sample as deposited. Comparing both Raman spectra,  $\text{Ti}_2\text{C}$  and  $\text{Ti}_3\text{C}_2$  peaks start to appear after the HF etching process. Taking a closer look at the peaks located at  $\omega_1 = 192 \text{ cm}^{-1}$  and  $\omega_2 = 260 \text{ cm}^{-1}$ , a narrowing of both peaks takes place. This can be a result of the overlapping vibrational modes of MAX and MXene in this wavelengths. With an increasing amount of MXene in the sample, the peak confines, since the neighboring  $\text{Ti}_3\text{C}_2$  found at  $\omega_1 = 192 \text{ cm}^{-1}$  starts to decrease its intensity. At the rest of the peaks, the already mentioned broadening takes place, which implicates that a percentage of the MAX phase transforms to MXene, as Table 4.5 shows.



Table 4.5 FWHM of characteristic peaks in Raman spectra (Figure 4.10) of MAX phases annealed at 900 °C ( $Ti_2AlC$  and  $Ti_3AlC_2$ ) by RTP process as prepared and after 2 hours HF etching.

Peak position	FWHM As Prepared	FWHM After Etching	$\Delta$ FWHM Difference
$\omega_1 = 192\text{ cm}^{-1}$	$20.35 \pm 0.80$	$19.27 \pm 1.36$	-1.08
$\omega_2 = 264\text{ cm}^{-1}$	$32.01 \pm 4.39$	$29.43 \pm 6.511$	-2.58
$\omega_3 = 360\text{ cm}^{-1}$	$31.66 \pm 0.78$	$40.58 \pm 1.33$	-8.92
$\omega_4 = 581\text{ cm}^{-1}$	$26.44 \pm 3.77$	$37.68 \pm 3.09$	11.24
$\omega_5 = 629\text{ cm}^{-1}$	$29.19 \pm 2.64$	$37.76 \pm 3.51$	8.57
$\omega_6 = 657\text{ cm}^{-1}$	$22.51 \pm 1.54$	$27.25 \pm 2.05$	1.74

To further confirm the explained hypothesis, a XRD of this sample was conducted to analyze this partial transformation of MAX phase into MXenes. Figure 4.11 shows XRD diffractogram of MAX phases annealed at 900 °C ( $Ti_2AlC$  and  $Ti_3AlC_2$ ) by RTP process as deposited and after 2 h HF etching.

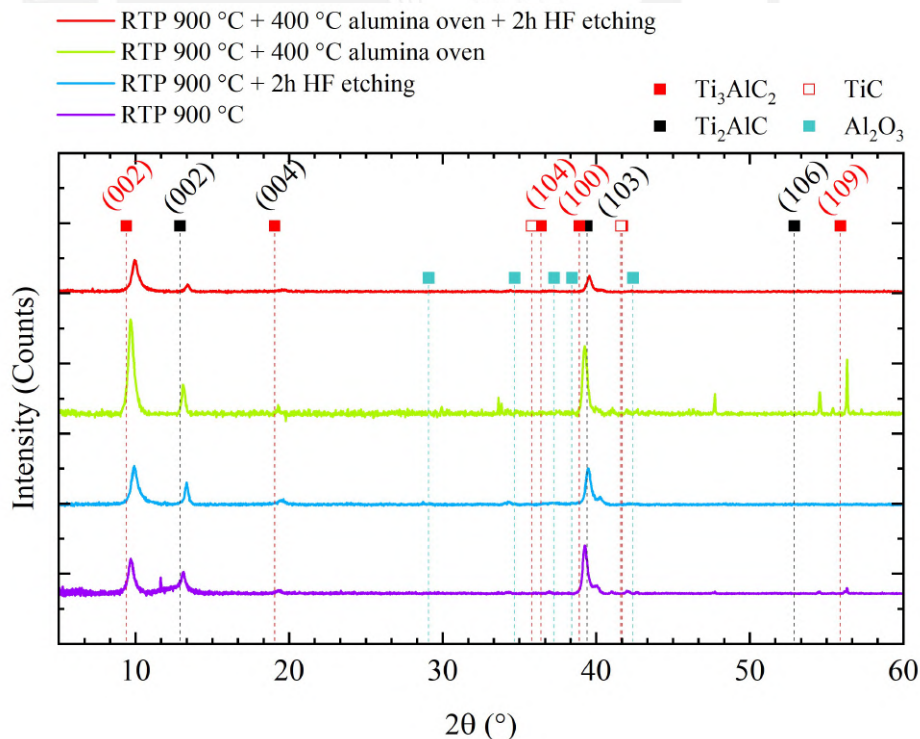


Figure 4.11 BB-XRD diffractogram of MAX phases annealed at 900 °C ( $Ti_2AlC$  and  $Ti_3AlC_2$ ) as deposited and after 2 h HF etching

As can be observed, a slight change in the  $13^\circ$  (002)  $\text{Ti}_2\text{AlC}$  peak as well as the  $9^\circ$  (002)  $\text{Ti}_3\text{AlC}_2$  towards higher angles is shown, which indicates the decrease in the interlayer spacing based on the Bragg equation. The decrease of interlayer spacing might be attributed to the dissolution of MAX phase and the formation of MXene on the surface of the sample. Further analysis of the diffractogram can be obtained by analyzing the FWHM values and therefore the crystal size, as Tables 4.6 and ?? show.

Table 4.6 Peak position of MAX phases annealed at  $900^\circ\text{C}$  by RTP process and MAX phases annealed at  $900^\circ\text{C}$  by RTP process with a subsequent thermal process at  $400^\circ\text{C}$  for 2 hours, obtained from Figure 4.11. Difference between the peak position as deposited and after HF etching

Peak	Peak Position As Prepared	Peak Position After Etching	Difference
(002) $\text{Ti}_3\text{AlC}_2$	$9.71^\circ \pm 0.25$	$9.93^\circ \pm 0.38$	0.02
(002) $\text{Ti}_2\text{AlC}$	$13.10^\circ \pm 0.05$	$13.33^\circ \pm 0.21$	0.23
(103) $\text{Ti}_2\text{AlC}$	$39.27^\circ \pm 0.09$	$39.49^\circ \pm 0.36$	0.22
(104) $\text{Ti}_3\text{AlC}_2$	$40.01^\circ \pm 0.10$	$40.20^\circ \pm 0.31$	0.19

Table 4.7 FWHM of MAX phases annealed at  $900^\circ\text{C}$  by RTP process and MAX phases annealed at  $900^\circ\text{C}$  by RTP process with a subsequent thermal process at  $400^\circ\text{C}$  for 2 hours, obtained from Figure 4.11. Difference between the FWHM values as deposited and after HF etching

Peak	FWHM As Prepared	FWHM After Etching	$\Delta$ FWHM Difference
(002) $\text{Ti}_3\text{AlC}_2$	$0.42 \pm 0.025$	$0.46 \pm 0.035$	0.04
(002) $\text{Ti}_2\text{AlC}$	$0.28 \pm 0.065$	$0.23 \pm 0.036$	-0.05
(103) $\text{Ti}_2\text{AlC}$	$0.31 \pm 0.039$	$0.37 \pm 0.09$	0.09
(104) $\text{Ti}_3\text{AlC}_2$	$0.49 \pm 0.064$	$0.52 \pm 0.036$	0.04

After a careful observation of the (002)  $\text{Ti}_3\text{AlC}_2$  diffraction peak at  $\sim 9^\circ$ , it can be seen that it widens after the etching process, implying a partial transformation of MAX phase into MXene, as explained before. Moreover, the strongest (104) peak of  $\text{Ti}_3\text{AlC}_2$  at  $39^\circ$  does not disappear. Therefore, the transformation of  $\text{Ti}_3\text{AlC}_2$  phase to  $\text{Ti}_3\text{C}_2$  MXene phase is only partial, as suggested before.

The electrical properties of the samples as prepared and after etching were determined, as Figure 4.12 shows.

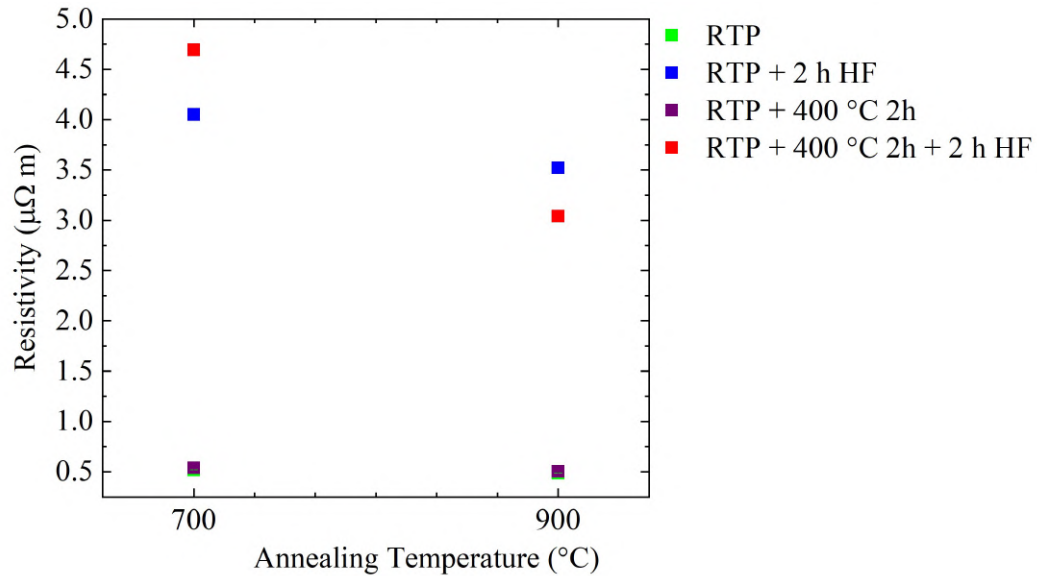


Figure 4.12 Electrical resistivity of MAX phase thin films as prepared and after 2 h HF etching. Notice that the error bars are comparatively small in comparison with the symbol and therefore not visible (to be found in the annex)

The values of the as deposited  $\text{Ti}_2\text{AlC}$  and  $\text{Ti}_3\text{AlC}_2$  are equivalent with the expected literature values ( $\rho_{\text{Ti}_2\text{AlC}} = 0.0344 \mu\Omega\text{m}$  [71],  $\rho_{\text{Ti}_3\text{AlC}_2} = 0.357 \mu\Omega\text{m}$  [110]). By etching the aluminum atoms from the thin films, the measured values increase to  $\rho_{700^\circ\text{C}} = 68 \mu\Omega\text{m}$  and  $\rho_{900^\circ\text{C}} = 5 \mu\Omega\text{m}$  respectively. These measured values correspond with the theoretical ones for the resulting MXene  $\text{Ti}_3\text{C}_2$ , which implies that the formation of the slight MXene obtained by the etching process corresponds to the  $\text{Ti}_3\text{C}_2$  phase.

## 4.2 Etching of nanostructured MAX phase thin films deposited at OAD

Nanostructured MAX phase thin films were likewise analyzed. The goal of this analysis is to unravel the relationship between the deposition angle  $\alpha$ , and by extension the column tilt angle  $\beta$ , and its response to the selective chemical etching by HF solution, as well as the analysis of the resultant MXenes and their morphology. For this goal, samples with different column tilt angles ( $\beta$  ( $23^\circ$ ),  $\gamma$  ( $31^\circ$ ) and  $\delta$  ( $27^\circ$ )) were HF etched as explained in Section 2.7. Table 4.8 shows the time in minutes the nanostructured MAX were in contact with HF etching solution before they delaminated.

Table 4.8 Etching time passed before delamination for MAX phases deposited at oblique angle deposition and annealed at 700 °C and 900 °C by RTP process

Sample	Annealed at 700 °C (Ti <sub>2</sub> AlC)	Annealed at 900 °C (Ti <sub>2</sub> AlC and Ti <sub>3</sub> AlC <sub>2</sub> )
$\beta_i$ (23°)	30 min	150 min
$\gamma_o$ (31°)	15 min	120 min
$\delta_o$ (27°)	15 min	120 min

As can be observed, the samples deposited at OAD and annealed at 700 °C via RTP do not withstand the etching process more than 30 minutes and delaminate quickly after starting the process. Since this samples are almost completely removed from the substrate surface, as Figure 4.13 shows, a posterior analysis is difficult to carry.

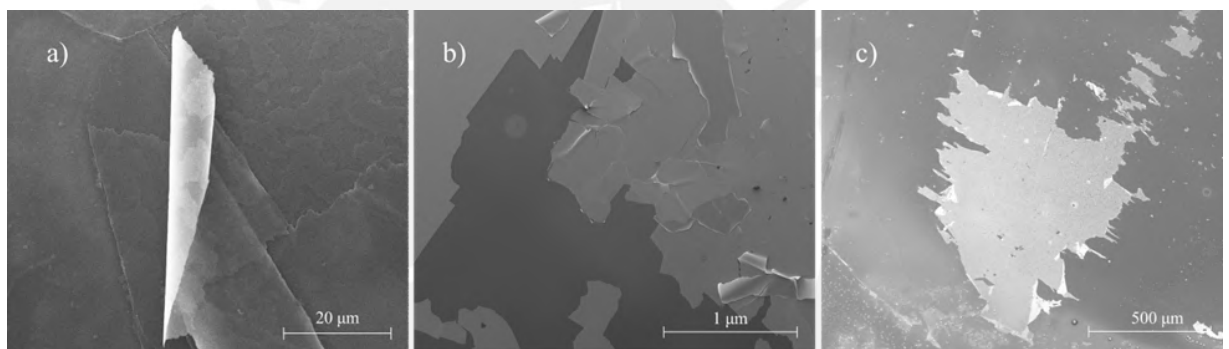


Figure 4.13 Top-view SEM images of nanostructured MAX phases deposited at OAD and annealed at 700 °C (Ti<sub>2</sub>AlC) by RTP process a)  $\beta$  (23°) after 30 min HF etching b)  $\gamma$  (31°) after 15 min HF etching c)  $\delta$  (27°) after 15 min HF etching

Characterization techniques like X-Ray Diffraction where the samples need to cover a certain amount of area on the substrate could not be carried out. However, a few points were analyzed with EDX analysis, as Figure 4.14 shows.

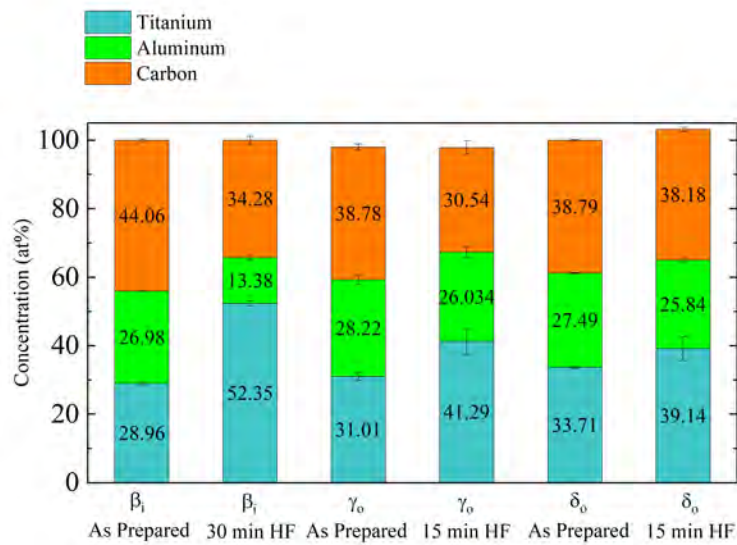


Figure 4.14 EDX analysis of nanostructured MAX phase deposited at OAD annealed at 700 °C via RTP as deposited and after various HF etching time

Table 4.9 Ti:Al ratio of MAX phases deposited at OAD and annealed at 700 °C ( $Ti_2AlC$ ) by RTP process as deposited and after HF etching

Ratio Ti:Al	Ti:Al ratio As Prepared	Ti:Al ratio After HF etching	Etching Time
$\beta_i$ (23°)	1.07	3.91	30 min
$\gamma_o$ (31°)	1.10	1.56	15 min
$\delta_o$ (27°)	1.23	1.51	15 min

When comparing the aluminum decrease as a function of the column tilt angle, it can be observed that the sample with the lowest column tilt angle  $\beta$  (23°) presents the highest aluminum removal.  $\beta$  shows an aluminum decrease of almost 50% in its chemical composition when compared with the samples as prepared.  $\gamma$  (31°) and  $\delta$  (27°) on the other hand only present a decrease in the aluminum concentration of about 7% with respect to the as prepared value. A high column tilt angle means a higher space between the nanocolumns and therefore an increasing porosity, as Figure 4.15 outlines. Correspondingly an increasing bundling effect is present, where the nanocolumns cluster perpendicularly to the material flux [14]. Since the etching was performed on the thin films surface, the porosity, and the assembling of the nanocolumns, play a crucial role in the penetration depth of the HF etching solution.

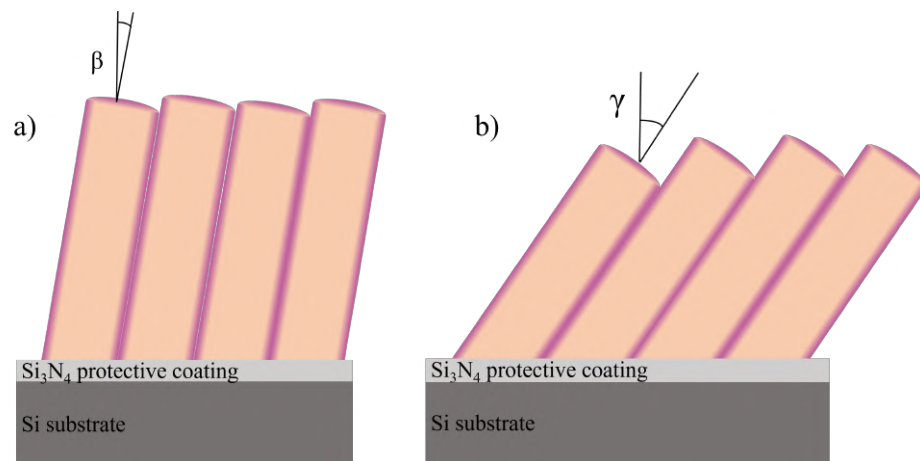


Figure 4.15 Schematic of resulting morphology of nanostructured MAX phases deposited at OAD after HF selective etching with different column tilt angle. Notice that the objects are not represented in real scale

The higher the columns tilt angle the bigger the canals formed, as shown previously in Figure 4.15, and the bigger the space for the HF to penetrate. This translates into the fastest penetration of the etching solution in the samples, which attacks the interface thin film/substrate and delaminates the sample faster. Therefore is responsible for the low etching time before delamination. As a result, the samples with the lower column tilt angle ( $\beta = 23^\circ$ ) have more time to be etched and therefore present a lower aluminum content.

The Ti:Al ratio for both samples with higher column tilt angles ( $\gamma$  ( $31^\circ$ ) and  $\delta$  ( $27^\circ$ )) remains almost the same, which indicates the HF etching solution did not attack successfully the thin films but etched the interface thin film/substrate rather than etching the aluminum atoms. To observe the possible creation of MXene in the surface of the sample, as well as in the grain boundaries between the nanocolumns, a XRD analysis of the residual sample  $\beta$  annealed at  $700^\circ\text{C}$  was performed, as depicted in Figure 4.16, since a small portion of the sample remained on the surface.



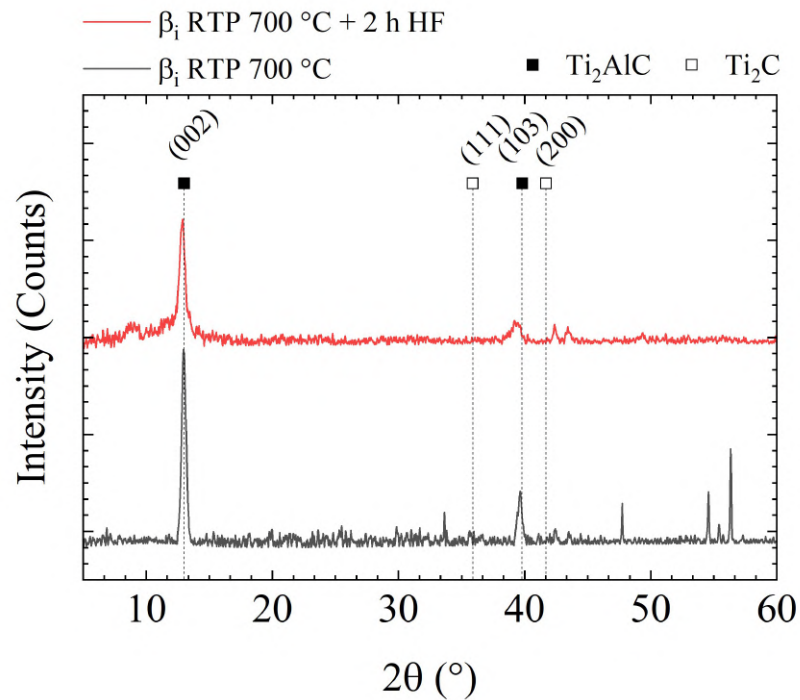


Figure 4.16 BB-XRD diffractogram of MAX phase deposited at OAD ( $\beta_1 \sim 23^\circ$ ) and annealed at  $700^\circ\text{C}$  by RTP process as prepared and after 30 min HF etching

As explained before, the characteristic changes in the diffractogram unravel the conversion of the MAX phase to its corresponding MXene [71]. In this case, an intensity decrease of the (103)  $\text{Ti}_2\text{AlC}$  peak at  $\sim 39^\circ$  is clearly observed. This characteristic peak in the sample as prepared can be found at  $2\theta = 39.378^\circ$  and after the etching process it shifts to  $2\theta = 39.192^\circ$ . To compare both diffractograms and quantify the intensity lost, the ratio between the intensity of the peak located at  $13^\circ$  against the intensity of the peak located at  $39^\circ$  was calculated. In the as deposited state, the ratio is  $\sim 2.35$ , whereas in the etched state it increases to  $\sim 4.32$ . This increase in the ratio between both peaks confirms the decrease in the peak located at  $39^\circ$ , which indicated a partial removal of the aluminum atoms. The FWHM of this characteristic peak decreases from 0.698 to 0.659 after the etching process.

Moreover, the crystallinity of the (002) peak decreases and the remaining peak is shifted to lower angles. This result combined with the previous EDX analysis indicates a partially successful etching of the sample deposited at OAD with a column tilt angle of  $\beta \sim 23^\circ$  after 30 minutes HF etching.

When taking a closer look using a SEM microscope at the samples annealed at  $900^\circ\text{C}$  by RTP process where both MAX phases ( $\text{Ti}_2\text{AlC}$  and  $\text{Ti}_3\text{AlC}_2$ ) are found, it can be observed that this samples do not completely delaminate, as Figure 4.17

shows. Independently of the columns tilt angle, all three samples show a cracking in the sample surface and between the nanocolumns, which expands through the surface of the substrate.

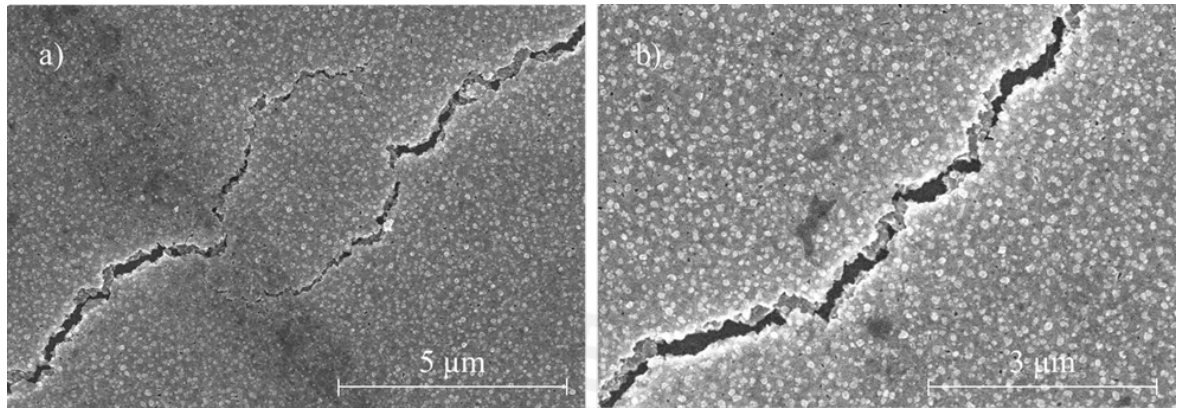


Figure 4.17 Top-view SEM images of MAX phases deposited at OAD and annealed at 900 °C ( $\text{Ti}_2\text{AlC}$  and  $\text{Ti}_3\text{AlC}_2$ ) by RTP process after 2 h HF etching process at different magnifications a) 10kx and b) 15kx

Figure 4.18 shows top-view SEM images of the MAX phase thin films deposited at different angles and therefore with different column tilt angles after HF etching. As can be observed, there are some etching attack points on the surface of the samples, which can be noticed as black spots. This are more common to see in sample  $\beta$  ( $23^\circ$ ) than in samples  $\gamma$  ( $31^\circ$ ) and  $\delta$  ( $27^\circ$ ). Again, this can be explained not only by the column tilt angle, but in this case by the chemical composition and phase distribution in the samples. When annealing the Ti-Al-C multilayer system deposited at OAD at 900 °C, both  $\text{Ti}_3\text{AlC}_2$  and  $\text{Ti}_2\text{AlC}$  phases are present [96] and coexist in the sample. A possible hypothesis can establish that this dark spots are a result of the etching of the  $\text{Ti}_2\text{AlC}$  phase and initiate the crack propagation in the sample. Since the sample annealed at 900 °C remained for a prologated time at higher temperatures in vacuum, the reorganization of the atoms is favored. The space between columns, and by extension the porosity of the sample, decrease with increasing temperature, which leads to a higher resistance to the crack propagation.

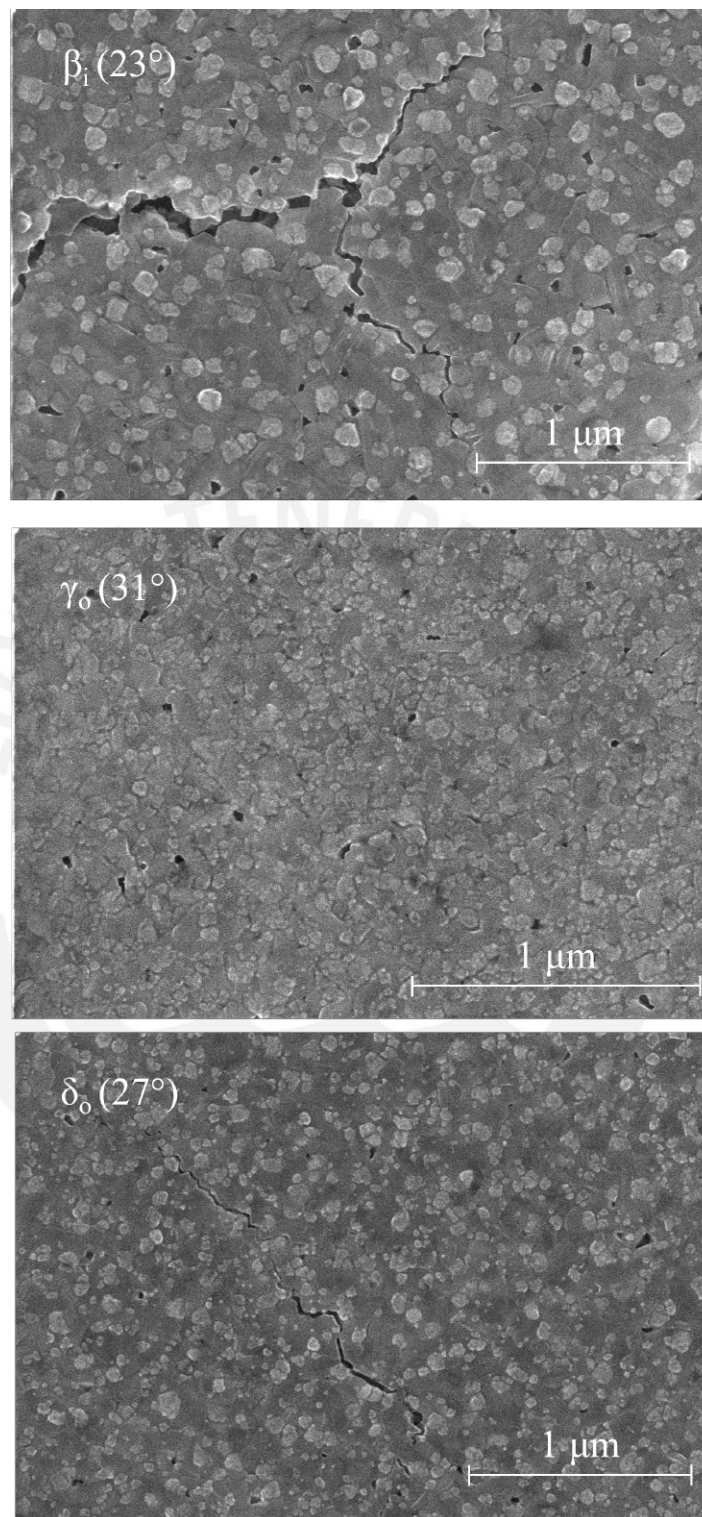


Figure 4.18 Top-view SEM images of MAX phases deposited at OAD and annealed at  $900^\circ\text{C}$  ( $\text{Ti}_2\text{AlC}$  and  $\text{Ti}_3\text{AlC}_2$ ) by RTP process after 2 h HF etching with different column tilt angles ( $\beta$  ( $23^\circ$ ),  $\gamma$  ( $31^\circ$ ) and  $\delta$  ( $27^\circ$ )). Notice that only sample  $\beta$  resisted until 150 minutes etching time, while the samples with the higher columns tilt angles ( $\delta$  and  $\gamma$ ) resisted a total time of 120 minutes

An EDX analysis of the samples were carried out to follow the compositional changes in the thin film through the etching process, as Figure 4.19 shows.

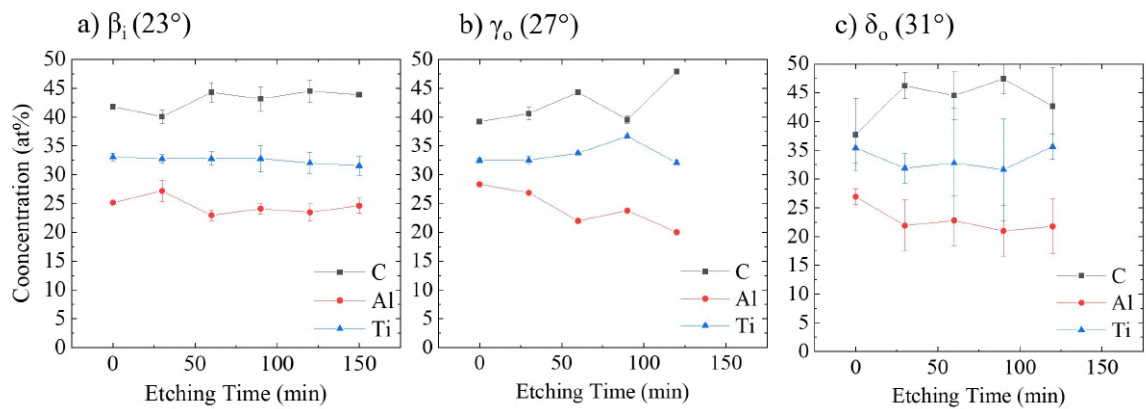


Figure 4.19 EDX analysis of nanostructured MAX phases deposited at OAD ( $\beta$  (23°),  $\gamma$  (31°) and  $\delta$  (27°)) and annealed at 900 °C ( $Ti_2AlC$  and  $Ti_3AlC_2$ ) by RTP process with different etching time. Notice that the lines draw between the dots were not measured and are only included to guide the eye

The chemical composition of the samples through the etching process does not vary dramatically. A constant decrease of the aluminum concentration is noticeable, but yet again the aluminum concentration after the etching process remains if compared with other authors too high to create pure MXene, as Figure 4.20 shows.

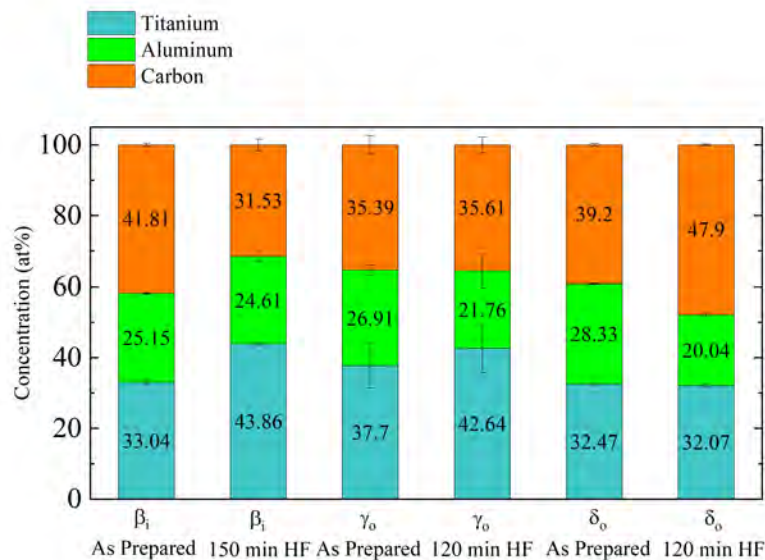


Figure 4.20 EDX analysis of nanostructured MAX phases deposited at OAD ( $\beta$  (23°),  $\gamma$  (31°) and  $\delta$  (27°)) and annealed at 900 °C ( $Ti_2AlC$  and  $Ti_3AlC_2$ ) by RTP process as prepared and after different etching time



Table 4.10 Ti:Al ratio of MAX phases deposited at OAD ( $\beta$  ( $23^\circ$ ),  $\gamma$  ( $31^\circ$ ) and  $\delta$  ( $27^\circ$ )) and annealed at  $900^\circ\text{C}$  ( $\text{Ti}_2\text{AlC}$  and  $\text{Ti}_3\text{AlC}_2$ ) by RTP process as deposited and after HF etching

Ratio Ti:Al	Ti:Al ratio As Prepared	Ti:Al ratio After HF etching	Etching Time
$\beta_i$ ( $23^\circ$ )	1.31	1.78	150 min
$\gamma_o$ ( $31^\circ$ )	1.23	1.60	120 min
$\delta_o$ ( $27^\circ$ )	1.40	2.00	120 min

The aluminum concentration in all three samples decreases, whereas its high concentration in the etched samples indicates that the MAX phase was not completely etched to MXenes, but only a few nanometers on the surface and between then nanocolumns were attacked by the HF solution.

Contrary on the effect observed in the nanostructured MAX phases annealed  $700^\circ\text{C}$ , where  $\beta$  ( $23^\circ$ ) presented the highest aluminum removal, in the samples annealed at  $900^\circ\text{C}$  with an increasing column tilt angle there is an increasing aluminum atoms removal. In sample  $\beta$  the decrease of the aluminum concentration is smaller ( $\sim 4\%$ ) than in the  $\gamma$  ( $\sim 20\%$ ) and  $\delta$  ( $\sim 30\%$ ) samples. This effect can be explained because the MAX phases annealed at  $900^\circ\text{C}$  withstand the delamination of the substrate better than the ones annealed at  $700^\circ\text{C}$ . Therefore, with an increasing etching time (150 minutes vs 30 minutes), the HF solution can properly etch the MAX phase. With an increasing column tilt angle and therefore porosity, the HF solution attacks the grain boundaries easily and removes a higher amount of aluminum atoms. Moreover, the defect density is higher in the grain boundaries between the columns, a higher effective surface is attacked by the HF solution when compared with the MAX phases deposited as a compact layer.

To give an idea about the proportion of the total MAX thin film that has been etched to MXene and determine therefore crystallographic changes in the surface after the HF etching process, a grazing incidence XRD analysis with an incident angle  $\theta = 3^\circ$  was performed. Figure 4.21 shows the characteristic (002) of  $\text{Ti}_2\text{AlC}$  and  $\text{Ti}_3\text{AlC}_2$ . For further analysis of the etching process as a function of the column tilt angle, only the (002)  $\text{Ti}_3\text{AlC}_2$  peak was analyzed.

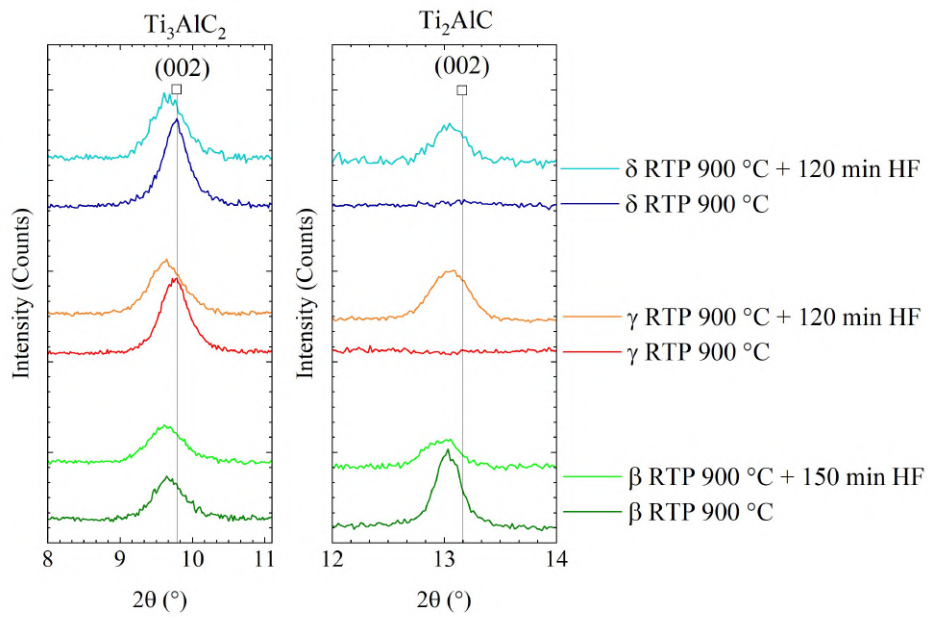


Figure 4.21 GI-XRD diffractogram of nanostructured MAX phases ( $\beta$  ( $23^\circ$ ),  $\gamma$  ( $31^\circ$ ) and  $\delta$  ( $27^\circ$ )) and annealed at  $900^\circ\text{C}$  ( $\text{Ti}_2\text{AlC}$  and  $\text{Ti}_3\text{AlC}_2$ ) by RTP process as prepared and after the etching process

Table 4.11 Peak position of peak located at  $2\theta \sim 9.5^\circ$ . Notice that the analysis of the diffraction peak (002)  $\text{Ti}_2\text{AlC}$  could not be carried out due to the lack of data as prepared. Difference between the peak position as deposited and after HF etching

Sample	Peak Position As Prepared	Peak Position After Etching	Difference
$\beta_i$ ( $23^\circ$ )	$9.663^\circ \pm 0.065$	$9.627^\circ \pm 0.213$	-0.037
$\gamma_o$ ( $31^\circ$ )	$9.751^\circ \pm 0.482$	$9.627^\circ \pm 0.125$	-0.102
$\delta_o$ ( $27^\circ$ )	$9.763^\circ \pm 0.324$	$9.662^\circ \pm 0.032$	-0.123

Table 4.12 FWHM of peak located at  $2\theta \sim 9.5^\circ$ . Notice that the analysis of the diffraction peak (002)  $\text{Ti}_2\text{AlC}$  could not be carried out due to the lack of data as prepared. Difference between the FWHM value as deposited and after HF etching

Sample	FWHM As Prepared	FWHM After Etching	$\Delta$ FWHM Difference
$\beta_i$ ( $23^\circ$ )	$0.382 \pm 0.035$	$0.536 \pm 0.038$	0.053
$\gamma_o$ ( $31^\circ$ )	$0.363 \pm 0.032$	$0.539 \pm 0.097$	0.086
$\delta_o$ ( $27^\circ$ )	$0.309 \pm 0.047$	$0.559 \pm 0.069$	0.150



The characteristic (002)  $\text{Ti}_3\text{AlC}_2$  peak is shifted to lower angles independently of the column tilt angle, as Figure 4.21 shows. This downshifting confirms the formation of MXene phase on the MAX thin film. When comparing the broadening of the peak with the column tilt angle,  $\beta$  ( $23^\circ$ ) shows the smallest broadening and down-shifting. Since the broadening of the peak and the down-shifting increases with increasing column tilt angle, it can be established that a higher amount of the thin film is converted from MAX phase to MXene due to the increasing porosity.

The peak found at  $39^\circ$  does not completely vanish which indicates the co-existence of both MAX phases and MXenes in the thin film. This result is in good accordance to the previous results and supports the explained hypothesis. The obvious downshifting of this peak when compared with the samples deposited at normal configuration suggests a higher transformation percentage of MAX phase into MXene. This can be explained by the fact that MAX phases deposited at OAD present a higher surface area than MAX phases deposited at normal configuration due to its columnar structure. A higher surface area translates into a higher contact area with the HF solution, as Figure 4.15 shows, which simultaneously implicates a higher superficial MAX phase etched into MXene.

Figure 4.22 shows the XRD diffractograms obtained in Bragg Brentano configuration of the OAD deposited MAX phases annealed at  $900^\circ\text{C}$  after different etching times for the segment  $5^\circ$  to  $20^\circ$ , where both (002)  $\text{Ti}_2\text{AlC}$  and  $\text{Ti}_3\text{AlC}_2$  characteristic peaks at  $2\theta \sim 9.5^\circ$  and  $2\theta \sim 13.7^\circ$  respectively can be found. Since the rest of the diffractogram does not suffer mentionable changes, the diffractogram over the range  $5^\circ$  to  $80^\circ$  can be found in the annex.

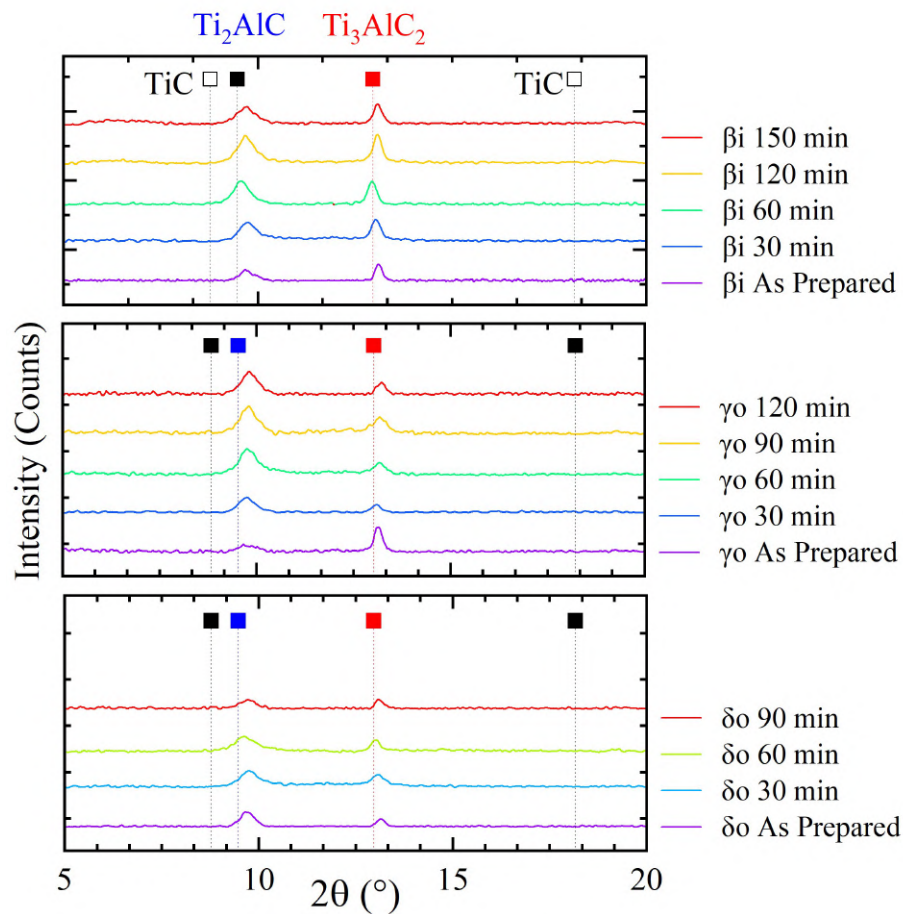


Figure 4.22 BB-XRD diffractogram of MAX phase deposited at OAD ( $\beta$  ( $23^\circ$ ),  $\gamma$  ( $31^\circ$ ) and  $\delta$  ( $27^\circ$ )) and annealed at  $900^\circ\text{C}$  ( $\text{Ti}_2\text{AlC}$  and  $\text{Ti}_3\text{AlC}_2$ ) by RTP process as prepared and after HF etching

Table 4.13 and Table 4.14 show the values obtained from these diffractograms, whereas they compare the peak position of the (002)  $\text{Ti}_3\text{AlC}_2$  found at  $\sim 9.5^\circ$  as well as the FWHM as prepared and after the HF etching.

Table 4.13 Peak position of the (002)  $\text{Ti}_3\text{AlC}_2$  peak as prepared and after HF etching of nanostructured MAX phase annealed at  $900^\circ\text{C}$  by RTP process, and calculated down-shifting

Sample	Peak Position As Prepared ( $^\circ$ )	Peak Position After Etching ( $^\circ$ )	Downshifting of peak (002)
$\beta_i$ ( $23^\circ$ )	$9.71 \pm 0.004$	$9.70 \pm 0.006$	0.01
$\gamma_o$ ( $31^\circ$ )	$9.75 \pm 0.030$	$9.62 \pm 0.070$	0.12
$\delta_o$ ( $27^\circ$ )	$9.72 \pm 0.02$	$9.683 \pm 0.001$	0.04

Table 4.14 Calculated difference between FWHM value as prepared and after HF etching for nanostructured MAX phases annealed at 900 °C by RTP process

Sample	FWHM As Prepared	FWHM After Etchng	Broadening of peak (002)
$\beta_i$ (23°)	$0.353 \pm 0.013$	$0.419 \pm 0.017$	0.065
$\gamma_o$ (31°)	$0.440 \pm 0.025$	$0.544 \pm 0,013$	0.104
$\delta_o$ (27°)	$0.424 \pm 0.009$	$0.564 \pm 0,019$	0.140

The characteristic (002) peak moves to lower angles for all samples. Again, the broadening of the peak gives an insight into the amount of MAX phase transformed into MXene. A higher difference in this value indicates a bigger broadening of the peak. Since the broadening is explained by a higher MXene percentage, the sample with the highest difference presents a broader peak. Sample  $\delta$  (27°) presents a relatively high column tilt angle, and therefore the HF solution easily penetrates into the sample, etching the nanocolumns limits, as Figure 4.23 depicts.

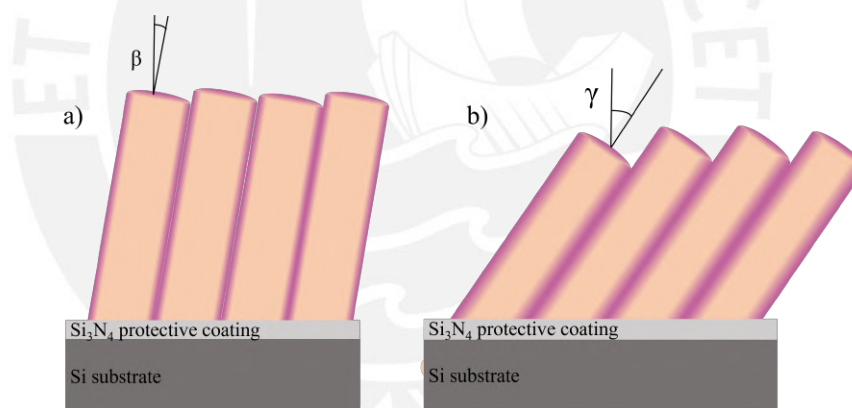


Figure 4.23 Corrected schematical of Figure 4.14 after analyzing the experiment results

To further confirm this theory, Raman spectroscopy of the nanostructured MAX phase samples annealed at 900 °C was performed, as Figure 4.24 shows. This analysis shows an evolution of the as prepared samples as a function of the etching time towards less defined Raman peaks.

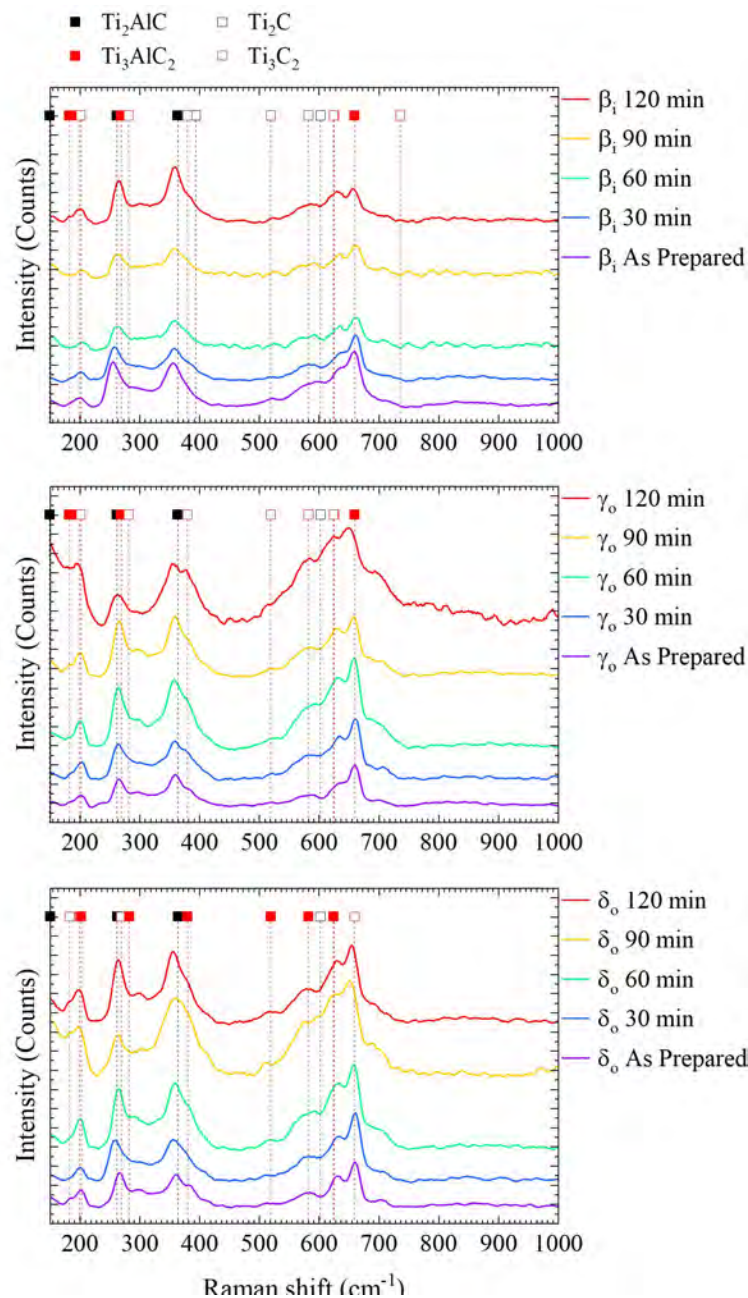


Figure 4.24 Raman spectra of MAX phases deposited at OAD ( $\beta$  (23°),  $\gamma$  (31°) and  $\delta$  (27°)) and annealed at 900 °C (Ti<sub>2</sub>AlC and Ti<sub>3</sub>AlC<sub>2</sub>) by RTP process as prepared and after several HF etching time

When taking a closer look at sample  $\beta$  (23°), a transformation of the Ti<sub>3</sub>AlC<sub>2</sub> peak at  $\omega = 680 \text{ cm}^{-1}$  towards the Ti<sub>3</sub>C<sub>2</sub> peak at  $\omega = 624 \text{ cm}^{-1}$  is clearly noticeable. This peak can be attributed to the  $E_g$  vibrations of the C atoms in the -OH MXene Ti<sub>3</sub>C<sub>2</sub> as the literature suggests [80]. Therefore, a small amount of the MAX phase is etched in MXene. In the sample  $\gamma$  (31°) it can be seen a general loss of crystallinity. Also, the

formation of peak at  $\omega = 380 \text{ cm}^{-1}$  and  $\omega = 582 \text{ cm}^{-1}$ , which in the literature is reported as to the O atoms in the  $E_g$  and  $A_{1g}$  vibrations in  $\text{Ti}_3\text{C}_2$  respectively, implies the slow conversion of MAX phase into MXene.

To compare the as deposited state and the resulting morphology after the etching process, Figure 4.25 shows the Raman spectra of the samples as a function of the column tilt angle.



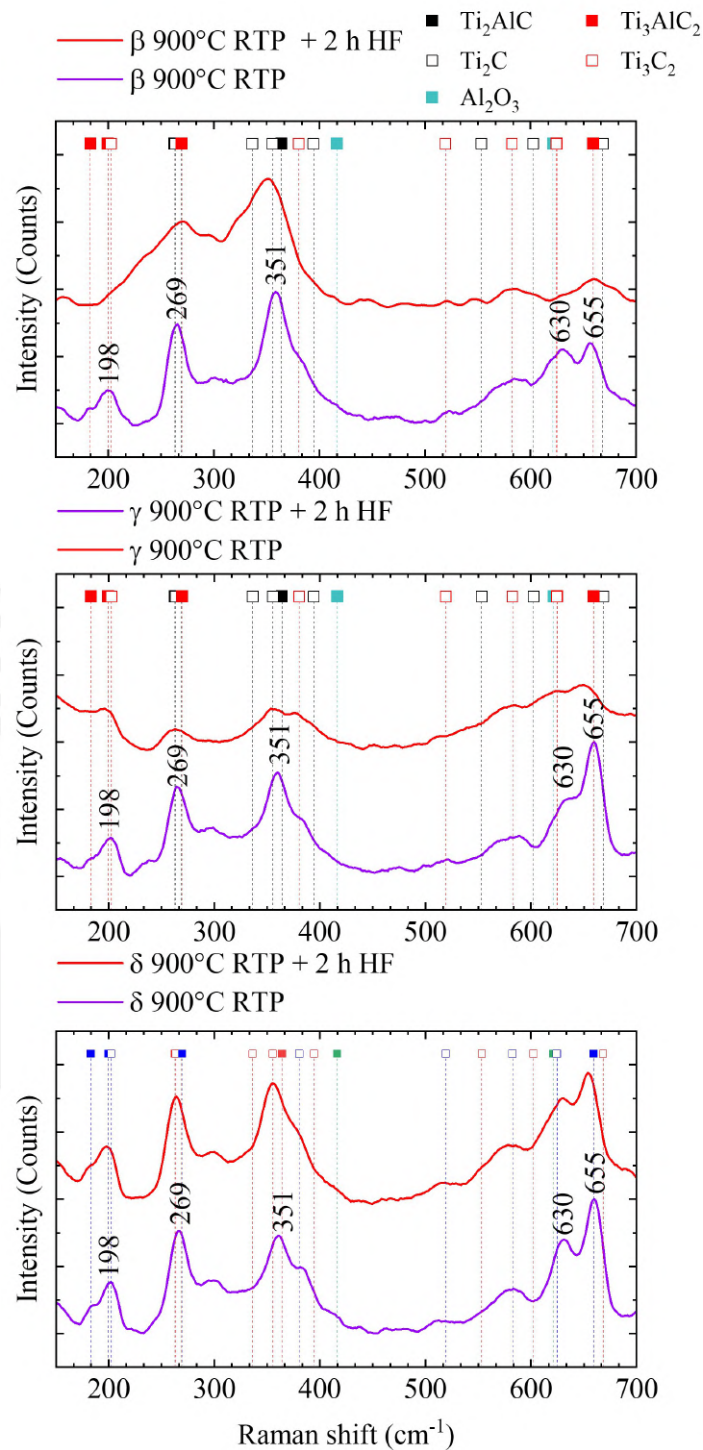


Figure 4.25 Raman spectra of MAX phases deposited at OAD ( $\beta$  ( $23^\circ$ ),  $\gamma$  ( $31^\circ$ ) and  $\delta$  ( $27^\circ$ )) and annealed at 900°C ( $\text{Ti}_2\text{AlC}$  and  $\text{Ti}_3\text{AlC}_2$ ) by RTP process as prepared and after the HF etching process

In sample  $\beta$  ( $23^\circ$ ), the  $\text{Ti}_3\text{AlC}_2$  peak at  $\omega = 580 \text{ cm}^{-1}$  slightly increases its area and



width with increasing etching time, showing the growth of the MXene percentage in the thin film. Sample  $\delta$  ( $27^\circ$ ) shows a similar behaviour when comparing the as deposited state with the HF etched samples. The  $\text{Ti}_3\text{C}_2$  peaks start to form while increasing the etching time.

Table 4.15 FWHM values of nanostructured MAX phases deposited at OAD ( $\beta$  ( $23^\circ$ ),  $\gamma$  ( $31^\circ$ ) and  $\delta$  ( $27^\circ$ )) and annealed at  $900^\circ\text{C}$  ( $\text{Ti}_2\text{AlC}$  and  $\text{Ti}_3\text{AlC}_2$ ) by RTP process as prepared and after the HF etching process

Sample	Peak	FWHM As Prepared	FWHM After Etchng	$\Delta$ FWHM Difference
$\beta_i$ ( $23^\circ$ )	$\omega \sim 269 \text{ cm}^{-1}$	$68.61 \pm 0.13$	$22.25 \pm 0.17$	-46.36
	$\omega \sim 350 \text{ cm}^{-1}$	$44.02 \pm 0.44$	$38.12 \pm 0.70$	-5.90
	$\omega \sim 630 \text{ cm}^{-1}$	$19.9 \pm 0.12$	$21.96 \pm 0.09$	2.05
	$\omega \sim 655 \text{ cm}^{-1}$	$32.10 \pm 0.21$	$28.74 \pm 0.25$	-3.36
$\gamma_o$ ( $31^\circ$ )	$\omega \sim 269 \text{ cm}^{-1}$	$33.65 \pm 0.25$	$27.86 \pm 0,13$	-5.79
	$\omega \sim 350 \text{ cm}^{-1}$	$50.28 \pm 0.50$	$55.61 \pm 0.30$	5.33
	$\omega \sim 630 \text{ cm}^{-1}$	$34.38 \pm 0.28$	$25.89 \pm 0.29$	-8.49
	$\omega \sim 655 \text{ cm}^{-1}$	$35.07 \pm 0.95$	$46.03 \pm 0.97$	10.96
$\delta_o$ ( $27^\circ$ )	$\omega \sim 269 \text{ cm}^{-1}$	$24.43 \pm 0.65$	$22.43 \pm 0,35$	-2.00
	$\omega \sim 350 \text{ cm}^{-1}$	$49.06 \pm 0.35$	$48.99 \pm 0.68$	-0.07
	$\omega \sim 630 \text{ cm}^{-1}$	$28.17 \pm 0.68$	$35.7 \pm 0.67$	7.59
	$\omega \sim 655 \text{ cm}^{-1}$	$18.81 \pm 0.57$	$21.73 \pm 0.72$	2.92

## 5 Summary and Conclusions

The deposition rate of the titanium, aluminum and carbon targets was determined by variable angle spectroscopic ellipsometry as well as X-Ray Reflection to calculate the necessary deposition parameters for Ti-Al-C co-deposited thin films. For the synthesis of MAX phases, a multilayer system and a co-deposition precursor with a subsequent ex-situ annealing process at 700 °C and 900 °C for the formation of  $Ti_2AlC$  and  $Ti_3AlC_2$  respectively. In addition, active heating was tried for both configurations to unravel the role of temperature during the deposition process.

The Ti:Al ratio of the as deposited samples for the creation of MAX phases was established at  $\sim 1.2$ . After the deposition, only the multilayer system deposited without active heating achieved this requirement. Even with an increasing annealing temperature, the chemical composition of this sample remained a promising candidate for the formation of MAX phases. After performing the materials properties analyses using various characterization techniques, it can be established that the Ti-Al-C layers in all configurations were deposited amorphously and therefore no indication of MAX phase was present. In the multilayer system without active heating a small peak at  $39^\circ$  in the XRD diffractogram reveals the start of the formation of MAX phase in this sample. Analyzing this sample in Raman spectroscopy, amorphous carbon is still noticeable, but various vibrational modes corresponding of the  $Ti_3AlC_2$  MAX phase start to be noticeable.

Moreover, the deposition of nanostructured Ti-Al-C multilayer thin film with a subsequent annealing treatment was done to create nanostructured MAX phase. XRD and Raman spectroscopy confirmed the presence of MAX phase in the thin film, which was shaped in nanocolumn form. Top-view and cross-section SEM images corroborate the nanocolumnar morphology and the bundling association expected as well as the different column tilt angles. This nanocolumns were achieved due to the off-normal geometrical configuration of the substrate regarding the targets and with the help of a L-shaped substrate holder. When analyzing its chemical composition, the ideal ratio afore mentioned of 1.2 is accomplished for all samples.

The synthesis of MXenes from a MAX phase and nanostructured MAX phase was also studied in this work. For the removal of the aluminum atoms from the MAX precursors, they underwent a wet HF selective etching process. As a reference, MAX phases obtained from a multilayer approach with two annealing temperatures (700 °C

and 900 °C) were etched to first understand the etching mechanism of the MAX phases. After 120 minutes the samples showed multiple cracks on the surface of the sample which induced a delamination of the thin film from the substrate. This delamination is explained by the etching of the Si<sub>2</sub>N<sub>4</sub> protective coating grown in the thin film/substrate interface as well as the the SiO<sub>2</sub> thin film of the substrate. When comparing the chemical composition in the as deposited state and after the etching process, a considerable decrease in the aluminum concentration is observed, since the Ti:Al ratio increases from 1.2 to ~3. When comparing this value with the literature for pure MXenes, our value still remains too high. A possible hypothesis is the creation of a MXene thin film on top of the MAX thin film as a result of the contact with the HF etching solution. This effect can be supported by the XRD and Raman results. When increasing the MXene fraction, the corresponding (002) MAX phase diffraction peak shifts towards lower angles, increasing the width of the peak, since MAX phase is still present and its peak remains immovable. As a result, with increasing MXene fraction, the FWHM value increases correspondingly. A similar effect can be found in Raman spectroscopy, where the width of the vibrational modes of MAX phase increases when the MXene percentage increases. Furthermore, the identification of the top layer of the thin film can be supported by the electrical resistivity measured after the etching process. The measured resistivity values correspond with the ones expected from the literature from Ti<sub>3</sub>C<sub>2</sub> and Ti<sub>2</sub>C and therefore it can be established that MXene can be found on the surface of the thin film.

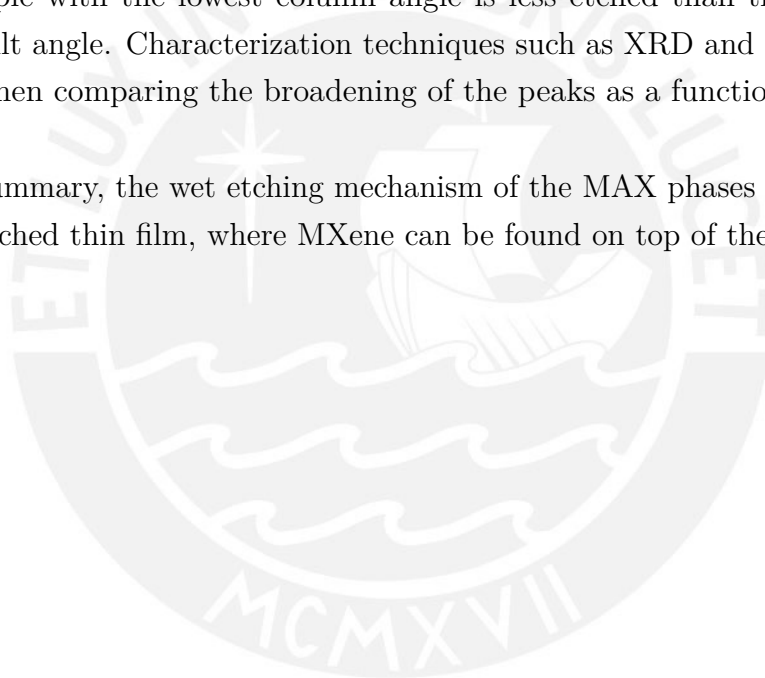
Nanostructured MAX phase were likewise analyzed. The main goal of this analysis is to unravel the relationship between the deposition angle  $\alpha$ , and by extension the column tilt angle  $\beta$ , and the response to the selective chemical etching by HF solution, as well as the analysis of the resultant MXenes and their morphology. The delamination process is again seen in this samples. However, the MAX phases annealed at 700 °C that correspond to the creation of Ti<sub>2</sub>AlC delaminate within 30 minutes whereas the samples annealed at 900 °C withstand 120 minutes.

Taking a closer look at the Ti<sub>2</sub>AlC samples, the chemical composition analysis indicates that the samples with the highest column tilt angle ( $\delta$  and  $\gamma$ ) delaminate faster and with an inferior aluminum etching than the ones with a low column tilt angle ( $\beta$ ). This is explained by the porosity of the sample. With increasing column tilt angle, the porosity of the sample equally increases. This allows the HF etching solution to penetrate in the sample and come in contact with the Si<sub>3</sub>N<sub>4</sub> protective coating faster, making the samples delaminate earlier. The successful etching of the  $\beta$  sample can be explained by the chemical composition as well as the broadening of the XRD peak.

More aluminum atoms get removed when compared with the normal-configuration MAX phases. For this reason, a possible explanation is the etching of the grain boundaries between the nanocolumns, whereas the core of the nanocolumn remains as MAX phase. The defect density is higher in the grain boundaries between the columns, a bigger effective surface is attacked by the HF solution when compared with the MAX phases deposited as a compact layer. Therefore, a higher percentage of the MAX phase is etched.

When the samples annealed at 900 °C are observed, an opposite effect is obtained. The samples with the highest column tilt angle present a superior aluminum etching than the ones with a low column tilt angle. Since the porosity increases with a higher column tilt angle, the HF solution penetrates more in the sample with the same time. The sample with the lowest column angle is less etched than the ones with higher column tilt angle. Characterization techniques such as XRD and Raman support this theory when comparing the broadening of the peaks as a function of the column tilt angle.

As a summary, the wet etching mechanism of the MAX phases showed as a result a partial etched thin film, where MXene can be found on top of the MAX thin film.



## 6 Further experiments

Firstly, the choice of the substrate has to be adequate. Some authors [28][65] report the deposition of MAX phases on  $\text{Al}_2\text{O}_3$ , MgO (111) and MgO (100) substrates preseeded with a 20 nm thin epitaxial TiC layer to provide improved growth conditions for the MAX phases due to the affinity of both phases. In this case, the alumina substrate would be out of the election due to future problems in the etching process. Taking this into account, future experiments could implicate depositing the MAX phase thin films on MgO with a thin TiC layer to avoid future delamination problems like the ones reported in this work.

When observing the deposition parameters of other authors, the substrate temperature is the first significant difference. Garkas et al. (2010) details a substrate temperature of  $T_{\text{Substrate}} = 520\text{ }^\circ\text{C}$ , a much higher value than our deposition temperature ( $100\text{ }^\circ\text{C}$ ). With an increasing deposition temperature, the mobility sputtered atoms and therefore the crystallinity of the deposited thin films can be improved [61]. This simple change could improve the Ti-Al-C precursor and the co-deposition from elemental targets without a subsequent annealing process could be possible. To further promote the crystalline deposition of the elements, a negatively charged voltage, also called bias, can be applied at the substrate [83], which affects crystallographic orientation of the resulting thin films.

Furthermore, the deposition configuration can be entirely rethought. One option implicates the deposition of the MAX phase via radio frequency reactive sputtering with composite Ti:Al target in  $\text{C}_2\text{H}_2/\text{Ar}$  atmosphere used as C source [90]. Other options like deposition via unbalanced type II DC magnetron sputtering using high elemental targets [65] or co-sputtering by middle-frequency (MF) magnetron sputtering from compound targets[86] opens the door to many deposition possibilities and configurations which leads to several MAX phase morphologies. The annealing temperature plays a crucial role in the formation of MAX phase from its precursors. Although the chosen annealing temperatures should be enough to create both 211 and 312 MAX phases, some authors try a succeeding temperature of  $1200\text{ }^\circ\text{C}$  [33]. The annealing time often differs from the one chosen in this work, whereas various authors anneal their samples for 1 hour [57], given the atoms more time to reorganize themselves and create the MAX phase.

During the etching process, parameters such as the HF concentration, etching tem-

perature, and etching time have a crucial influence on the formed products. Firstly, our etching process was carried out at room temperature. An increasing etching temperature could decrease the etching time and the need for a high etching concentration [48]. Moreover, the lowest HF etching solution concentration reported in literature is found at 5 wt% [101] whereas the lowest etching time in this case was established at 2 hours. The etching times at low HF concentration often average 12 hours. At room temperature with a decreasing HF solution concentration, the etching time increases (e.g., 5 wt% for 24 h, 10 wt% for 18 h, and 30 wt% for 5 h) [103].





# Acronyms Glossary

This glossary lists the acronyms used in this thesis together with their meanings.

2d	2-dimensional
Al	Aluminium
Ar	Argon
BB	Bragg-Brentano
BE	Backscattered Electrons
C	Carbon
CCD	Charge-coupled Device
Cu	Cooper
CVD	Chemical Vapor Deposition
DC	Direct Current
EDX	Energy Dispersive X-ray
FUV	Far Ultraviolet
FWHM	full width at half maximum
GI	Grazing Incidence
H	Hydrogen
HF	Hydrofluoric Acid
K	Kelvin
LiF	Lithium Fluoride
MS	Magnetron Sputtering
N	Nitrogen
Na	Sodium
NIR	Near Infrared Region
OAD	Oblique Angle Deposition
PTFE	Polytetrafluoroethylene
PVD	Physical Vapor Deposition
RF	Radio Frequency
RT	Room Temperature
RTP	Rapid Thermal Processing
sccm	Standard cubic centimeters per minute
SE*	*Secondary Electrons (in chapter 2.5)
	*Spectroscopic Ellipsometry (in chapter 2.6)

---

SEM	Scanning Electron Microscope
Ti	Titanium
TiC	Titanium Carbide
V	Volt
VASE	Variable Angle Spectroscopic Ellipsometry
W	Watt
XRD	X-Ray Diffraction
XRR	X-ray Reflectometry



# Bibliography

- [1] Accelerating Microscopy. *EDX Analysis with SEM: How Does it Work?* 2019.
- [2] H Adachi and K Wasa. “Thin Films and Nanomaterials”. In: *Handbook of Sputtering Technology*. Elsevier, 2012, pp. 3–39.
- [3] Alchetron.com. *Rapid thermal processing - Alchetron, the free social encyclopedia*. 2017.
- [4] *AlF<sub>3</sub> Crystal Structure - SpringerMaterials*. 11/14/2022.
- [5] M Alhabeab, K Maleski, B Anasori, P Lelyukh, L Clark, S Sin, and Y Gogotsi. “Guidelines for Synthesis and Processing of Two-Dimensional Titanium Carbide (Ti<sub>3</sub>C<sub>2</sub>T<sub>x</sub>MXene)”. In: *Chemistry of Materials* 29.18 (2017), pp. 7633–7644.
- [6] H Alnoor, A Elsukova, J Palisaitis, I Persson, EN Tseng, J Lu, L Hultman, and P Persson. “Exploring MXenes and their MAX phase precursors by electron microscopy”. In: *Materials Today Advances* 9 (2021), p. 100123.
- [7] R Alvarez, JM Garcia-Martin, MC Lopez-Santos, V Rico, FJ Ferrer, J Cotrino, AR Gonzalez-Elipe, and A Palmero. “On the Deposition Rates of Magnetron Sputtered Thin Films at Oblique Angles”. In: *Plasma Processes and Polymers* 11.6 (2014), pp. 571–576.
- [8] AnaPath. *Electron Microscopy - AnaPath*. 8/11/2022.
- [9] B Anasori, M Dahlgqvist, J Halim, EJ Moon, J Lu, BC Hosler, EN Caspi, SJ May, L Hultman, P Eklund, J Rosén, and MW Barsoum. “Experimental and theoretical characterization of ordered MAX phases Mo<sub>2</sub>TiAlC<sub>2</sub> and Mo<sub>2</sub>Ti<sub>2</sub>AlC<sub>3</sub>”. In: *Journal of Applied Physics* 118.9 (2015), p. 094304.
- [10] Andy Pearce, Oxford Vacuum Science. *Sputter deposition*. 4/27/2017.
- [11] AZoM.com. *The Difference Between Physical Vapor Deposition (PVD) & Chemical Vapor Deposition (CVD)*. 2018.
- [12] AZoM.com. *What is Raman Spectroscopy?* 2018.
- [13] Y Bai, X He, and R Wang. “Lattice dynamics of Al-containing MAX-phase carbides: a first-principle study”. In: *Journal of Raman Spectroscopy* 46.9 (2015), pp. 784–794.

- [14] A Barranco, A Borrás, AR Gonzalez-Elipe, and A Palmero. “Perspectives on oblique angle deposition of thin films: From fundamentals to devices”. In: *Progress in Materials Science* 76 (2016), pp. 59–153.
- [15] MW Barsoum, T El-Raghy, and M Ali. “Processing and characterization of Ti<sub>2</sub>AlC, Ti<sub>2</sub>AlN, and Ti<sub>2</sub>AlC<sub>0.5</sub>N<sub>0.5</sub>”. In: *Metallurgical and Materials Transactions A* 31.7 (2000), pp. 1857–1865.
- [16] DC Bell and AJ Garratt-Reed. *Energy Dispersive X-ray Analysis in the Electron Microscope*. Garland Science, 2003.
- [17] BR Braeckman, F Boydens, H Hidalgo, P Dutheil, M Jullien, AL Thomann, and D Depla. “High entropy alloy thin films deposited by magnetron sputtering of powder targets”. In: *Thin Solid Films* 580 (2015), pp. 71–76.
- [18] AA Bunaciu, EG Udriștioiu, and HY Aboul-Enein. “X-ray diffraction: instrumentation and applications”. In: *Critical reviews in analytical chemistry* 45.4 (2015), pp. 289–299.
- [19] IM Chirica, AG Mirea, Ș Neațu, M Florea, MW Barsoum, and F Neațu. “Applications of MAX phases and MXenes as catalysts”. In: *Journal of Materials Chemistry A* 9.35 (2021), pp. 19589–19612.
- [20] H Chu, S Song, C Li, and Des Gibson. “Surface Enhanced Raman Scattering Substrates Made by Oblique Angle Deposition: Methods and Applications”. In: *Coatings* 7.2 (2017), p. 26.
- [21] L Corbari, MA Cambon-Bonavita, GJ Long, F Grandjean, M Zbinden, F Gaill, and P Compère. “Iron oxide deposits associated with the ectosymbiotic bacteria in the hydrothermal vent shrimp *Rimicaris exoculata*”. In: *Biogeosciences* 5.5 (2008), pp. 1295–1310.
- [22] M Dahlgvist, B Alling, IA Abrikosov, and J Rosén. “Phase stability of Ti<sub>2</sub>AlC upon oxygen incorporation: A first-principles investigation”. In: *Physical Review B* 81.2 (2010).
- [23] *Development of X-ray crystallography | A publish.illinois.edu site - University of Illinois at Urbana-Champaign*. 2/3/2022.
- [24] L Ding, Y Wei, Y Wang, H Chen, J Caro, and H Wang. “A Two-Dimensional Lamellar Membrane: MXene Nanosheet Stacks”. In: *Angewandte Chemie (International ed. in English)* 56.7 (2017), pp. 1825–1829.

- [25] Z Du, C Wu, Y Chen, Q Zhu, Y Cui, H Wang, Y Zhang, X Chen, J Shang, B Li, W Chen, C Liu, and S Yang. “High-Entropy Carbonitride MAX Phases and Their Derivative MXenes”. In: *Advanced Energy Materials* (2021), p. 2103228.
- [26] ECM USA Vacuum Furnace Systems. *Jipelec<sup>TM</sup> - Rapid Thermal Processing & Annealing Furnaces*. 6/8/2020.
- [27] Edinburgh Instruments. *What is Raman Spectroscopy? / Raman Spectroscopy Principle*. 5/26/2021.
- [28] J Emmerlich, H Högberg, S Sasvári, POÅ Persson, L Hultman, JP Palmquist, U Jansson, JM Molina-Aldareguia, and Z Czigány. “Growth of Ti<sub>3</sub>SiC<sub>2</sub> thin films by elemental target magnetron sputtering”. In: *Journal of Applied Physics* 96.9 (2004), pp. 4817–4826.
- [29] Ewen Smith. *Modern Raman Spectroscopy: A Practical Approach*. Wiley, 2005.
- [30] Z Feng, P Ke, and A Wang. “Preparation of Ti<sub>2</sub>AlC MAX Phase Coating by DC Magnetron Sputtering Deposition and Vacuum Heat Treatment”. In: *Journal of Materials Science & Technology* 31.12 (2015), pp. 1193–1197.
- [31] AC Ferrari and J Robertson. “Raman spectroscopy of amorphous, nanostructured, diamond-like carbon, and nanodiamond”. In: *Philosophical transactions. Series A, Mathematical, physical, and engineering sciences* 362.1824 (2004), pp. 2477–2512.
- [32] DJ Gardiner. *Practical Raman spectroscopy*. Springer-Verlag, 1989.
- [33] W Garkas, C Leyens, and A Flores-Renteria. “Synthesis and Characterization of Ti<sub>2</sub>AlC and Ti<sub>2</sub>AlN MAX Phase Coatings Manufactured in an Industrial-Size Coater”. In: *Advanced Materials Research* 89-91 (2010), pp. 208–213.
- [34] Geochemical Instrumentation and Analysis. *Energy-dispersive detector (EDS)*. 4/26/2017.
- [35] M Ghidui, MR Lukatskaya, MQ Zhao, Y Gogotsi, and MW Barsoum. “Conductive two-dimensional titanium carbide ‘clay’ with high volumetric capacitance”. In: *Nature* 516.7529 (2014), pp. 78–81.
- [36] J Gonzalez-Julian. “Processing of MAX phases: From synthesis to applications”. In: *Journal of the American Ceramic Society* 104.2 (2021), pp. 659–690.

- [37] R Grieseler, T Kups, M Wilke, M Hopfeld, and P Schaaf. “Formation of Ti<sub>2</sub>AlN nanolaminate films by multilayer-deposition and subsequent rapid thermal annealing”. In: *Materials Letters* 82 (2012), pp. 74–77.
- [38] KSS Harsha. *Principles of Vapor Deposition of Thin Films*. Burlington: Elsevier, 2006.
- [39] MM Hawkeye and MJ Brett. “Glancing angle deposition: Fabrication, properties, and applications of micro- and nanostructured thin films”. In: *Journal of Vacuum Science & Technology A: Vacuum, Surfaces, and Films* 25.5 (2007), p. 1317.
- [40] H He, Q Gan, H Wang, GL Xu, X Zhang, D Huang, F Fu, Y Tang, K Amine, and M Shao. “Structure-dependent performance of TiO<sub>2</sub>/C as anode material for Na-ion batteries”. In: *Nano Energy* 44 (2018), pp. 217–227.
- [41] H Hiller. “Crystallography and Cohomology of Groups”. In: *The American Mathematical Monthly* 93.10 (1986), p. 765.
- [42] H Högberg, L Hultman, J Emmerlich, T Joelsson, P Eklund, JM Molina-Aldareguia, JP Palmquist, O Wilhelmsson, and U Jansson. “Growth and characterization of MAX-phase thin films”. In: *Surface and Coatings Technology* 193.1-3 (2005), pp. 6–10.
- [43] W Hong, BC Wyatt, SK Nemani, and B Anasori. “Double transition-metal MXenes: Atomistic design of two-dimensional carbides and nitrides”. In: *MRS Bulletin* 45.10 (2020), pp. 850–861.
- [44] A Iakunkov, A Nordenström, N Boulanger, C Hennig, I Baburin, and AV Talyzin. “Temperature-dependent swelling transitions in MXene Ti<sub>3</sub>C<sub>2</sub>T<sub>x</sub>”. In: *Nanoscale* 14.30 (2022), pp. 10940–10949.
- [45] InSciLab. *InSciLab - FWHM & Crystallite Size (Scherrer equation) from XRD using Origin /2 methods*. 2019.
- [46] J. M. Nieuwenhuizen and H. B. Haanstra. In: *Philips Technology Review* (1966), pp. 27–87.
- [47] J.A. Woollam. *Ellipsometry FAQ - J.A. Woollam*. 1/8/2018.
- [48] A Jawaid, A Hassan, G Neher, D Nepal, R Pachter, WJ Kennedy, S Ramakrishnan, and RA Vaia. “Halogen Etch of Ti<sub>3</sub>AlC<sub>2</sub> MAX Phase for MXene Fabrication”. In: *ACS nano* 15.2 (2021), pp. 2771–2777.
- [49] R Jenkins and JL de Vries. *Practical X-Ray Spectrometry*. Second Edition. New York, NY: Springer US, 1969.



- [50] John R. Ferraro, Kazuo Nakamoto and Chris W. Brown. *Introductory Raman Spectroscopy*. Second Edition. Elsevier, 2003.
- [51] John Wiley, ed. *Energy Dispersive Spectroscopy: Essential Knowledge Briefings*. Second Edition. Microscopy and Analysis, 2015.
- [52] S Jolly, MP Paranthaman, and M Naguib. “Synthesis of Ti<sub>3</sub>C<sub>2</sub>T<sub>z</sub> MXene from low-cost and environmentally friendly precursors”. In: *Materials Today Advances* 10 (2021), p. 100139.
- [53] AG Karydas and T Paradellis. “A study of silicon escape peaks for X-ray detectors with various crystal dimensions”. In: *AIP Conference Proceedings*. AIP, 4-7 Nov 1998, pp. 858–861.
- [54] J Kowalska and S DeBeer. “The role of X-ray spectroscopy in understanding the geometric and electronic structure of nitrogenase”. In: *Biochimica et biophysica acta* 1853.6 (2015), pp. 1406–1415.
- [55] Y Lan, Y Zou, X Ma, L Xu, L Shi, and J Zhang. “Fabrication of amorphous Al<sub>2</sub>O<sub>3</sub> optical film with various refractive index and low surface roughness”. In: *Materials Research Express* 7.8 (2020), p. 086405.
- [56] OD Leaffer, S Gupta, MW Barsoum, and JE Spanier. “On Raman scattering from selected M<sub>2</sub>A<sub>3</sub>C compounds”. In: *Journal of Materials Research* 22.10 (2007), pp. 2651–2654.
- [57] Y Li, G Zhao, Y Qian, J Xu, and M Li. “Deposition and characterization of phase-pure Ti<sub>2</sub>AlC and Ti<sub>3</sub>AlC<sub>2</sub> coatings by DC magnetron sputtering with cost-effective targets”. In: *Vacuum* 153 (2018), pp. 62–69.
- [58] A Loerinczi and M Popescu. “Silicon substrate influence on the X-ray diffraction patterns of thin amorphous films”. In: Romania: Petru Maior University, 2002, p. 130.
- [59] TY Ma, JL Cao, M Jaroniec, and SZ Qiao. “Interacting Carbon Nitride and Titanium Carbide Nanosheets for High-Performance Oxygen Evolution”. In: *Angewandte Chemie (International ed. in English)* 55.3 (2016), pp. 1138–1142.
- [60] Y Ma, N Liu, L Li, X Hu, Z Zou, J Wang, S Luo, and Y Gao. “A highly flexible and sensitive piezoresistive sensor based on MXene with greatly changed interlayer distances”. In: *Nature communications* 8.1 (2017), p. 1207.
- [61] CG Madras, L Goldman, PY Wong, and IN Miaoulis. “The Effect of Substrate Temperature on the Crystallinity and Stress of Ion Beam Sputtered Silicon on Various Substrates”. In: *MRS Proceedings* 338 (1994).

- [62] *Magnetron Sputtering [Working Title]*. IntechOpen, 2018.
- [63] Marta Miranda Marti. “Effect of temperature on Cr/SiO<sub>2</sub> Janus-like thin films regarding nanostructure and electrical properties”. Bachelor thesis. Ilmenau: Ilmenau University of Technology, 13/01/2021.
- [64] D Martin Knotter and TJJ Denteneer. “Etching Mechanism of Silicon Nitride in HF-Based Solutions”. In: *Journal of The Electrochemical Society* 148.3 (2001), F43.
- [65] V Mauchamp, W Yu, L Gence, L Piraux, T Cabioch, V Gauthier, P Eklund, and S Dubois. “Anisotropy of the resistivity and charge-carrier sign in nanolaminated Ti<sub>2</sub>AlC: Experiment and ab initio calculations”. In: *Physical Review B* 87.23 (2013).
- [66] M Mazumder, R Ahmed, M Hasan, SJ Lee, and MS Lee. “Spectroscopic Ellipsometry of Asphalt Binder: A Study of Optical Constants”. In: *International Journal of Civil Engineering* 18.3 (2020), pp. 251–259.
- [67] I Miccoli, F Edler, H Pfnür, and C Tegenkamp. “The 100th anniversary of the four-point probe technique: the role of probe geometries in isotropic and anisotropic systems”. In: *Journal of physics. Condensed matter : an Institute of Physics journal* 27.22 (2015), p. 223201.
- [68] Miko Yasaka. “X-ray thin-film measurement techniques: X-ray reflectivity measurement”. In: *Rigaku Journal* 26 (2010), pp. 1–9.
- [69] Multi-Wavelength Ellipsometers - Film Sense. *Technology Information*. 8/4/2022.
- [70] M Naguib, MW Barsoum, and Y Gogotsi. “Ten Years of Progress in the Synthesis and Development of MXenes”. In: *Advanced materials (Deerfield Beach, Fla.)* 33.39 (2021), e2103393.
- [71] M Naguib, M Kurtoglu, V Presser, J Lu, J Niu, M Heon, L Hultman, Y Gogotsi, and MW Barsoum. “Two-dimensional nanocrystals produced by exfoliation of Ti<sub>3</sub>AlC<sub>2</sub>”. In: *Advanced materials (Deerfield Beach, Fla.)* 23.37 (2011), pp. 4248–4253.
- [72] Noelly Zully Calderon Ipanique. *PhD Dissertation (yet to be published)*. 2022.
- [73] O Kaipoldayev. “Studying of 2D titanium carbide structure by Raman spectroscopy after heat treatment in argon and hydrogen atmospheres”. In: *Eurasian Chemico-Technological Journal* 19.2 (2017), pp. 197–200.
- [74] *Optical Diagnostics for Thin Film Processing*. Elsevier, 1996.

- [75] *Periodic Tables for SEM, TEM, Mass Spec, and NMR / JEOL EDS Perio.* 10/19/2022.
- [76] V Presser, M Naguib, L Chaput, A Togo, G Hug, and MW Barsoum. “First-order Raman scattering of the MAX phases:  $\text{Ti}_2\text{AlN}$ ,  $\text{Ti}_2\text{AlC}_{0.5}\text{N}_{0.5}$ ,  $\text{Ti}_2\text{AlC}$ ,  $(\text{Ti}_{0.5}\text{V}_{0.5})_2\text{AlC}$ ,  $\text{V}_2\text{AlC}$ ,  $\text{Ti}_3\text{AlC}_2$ , and  $\text{Ti}_3\text{GeC}_2$ ”. In: *Journal of Raman Spectroscopy* 43.1 (2012), pp. 168–172.
- [77] R Quispe, C Torres, L Eggert, GA Ccama, M Kurniawan, M Hopfeld, JL Zárate, MK Camargo, A Rosenkranz, JA Acosta, A Bund, P Schaaf, and R Grieseler. “Tribological and Mechanical Performance of  $\text{Ti}_2\text{AlC}$  and  $\text{Ti}_3\text{AlC}_2$  Thin Films”. In: *Advanced Engineering Materials* 24.10 (2022), p. 2200188.
- [78] ResearchGate. (2) *What is the interpretation of humps (broad peaks) in a XRD pattern which repeat themselves in a exact range?* 9/28/2022.
- [79] H Ritala and M Tuohiniemi. “Study on  $\text{Al}_2\text{O}_3$  Film in Anhydrous HF Vapor”. In: *Solid State Phenomena* 187 (2012), pp. 45–48.
- [80] A Sarycheva and Y Gogotsi. “Raman Spectroscopy Analysis of the Structure and Surface Chemistry of  $\text{Ti}_3\text{C}_2\text{T}_x$  MXene”. In: *Chemistry of Materials* 32.8 (2020), pp. 3480–3488.
- [81] T Schmid and P Dariz. “Raman Microspectroscopic Imaging of Binder Remnants in Historical Mortars Reveals Processing Conditions”. In: *Heritage* 2.2 (2019), pp. 1662–1683.
- [82] M Scimeca, S Bischetti, HK Lamsira, R Bonfiglio, and E Bonanno. “Energy Dispersive X-ray (EDX) microanalysis: A powerful tool in biomedical research and diagnosis”. In: *European journal of histochemistry : EJH* 62.1 (2018), p. 2841.
- [83] JM Seeman. “Bias sputtering: its techniques and applications”. In: *Vacuum* 17.3 (1967), pp. 129–137.
- [84] M Shekhirev, CE Shuck, A Sarycheva, and Y Gogotsi. “Characterization of MXenes at every step, from their precursors to single flakes and assembled films”. In: *Progress in Materials Science* 120 (2021), p. 100757.
- [85] F Shi. “Introductory Chapter: Basic Theory of Magnetron Sputtering”. In: *Magnetron Sputtering [Working Title]*. IntechOpen, 2018.
- [86] R Shu, F Ge, F Meng, P Li, J Wang, Q Huang, P Eklund, and F Huang. “One-step synthesis of polycrystalline  $\text{V}_2\text{AlC}$  thin films on amorphous substrates by magnetron co-sputtering”. In: *Vacuum* 146 (2017), pp. 106–110.

- [87] AK Singh, N Yasri, K Karan, and EPL Roberts. “Electrocatalytic Activity of Functionalized Carbon Paper Electrodes and Their Correlation to the Fermi Level Derived from Raman Spectra”. In: *ACS Applied Energy Materials* 2.3 (2019), pp. 2324–2336.
- [88] JE Spanier, S Gupta, M Amer, and MW Barsoum. “Vibrational behavior of the  $M_{n+1}AX_n$  phases from first-order Raman scattering ( $M=Ti, V, Cr, A=Si, X=C, N$ )”. In: *Physical Review B* 71.1 (2005).
- [89] L Spieß, G Teichert, R Schwarzer, H Behnken, and C Genzel. “Kristallstruktur-analyse”. In: *Moderne Röntgenbeugung*. Ed. by L Spieß, G Teichert, R Schwarzer, H Behnken, and C Genzel. Wiesbaden: Springer Fachmedien Wiesbaden, 2019, pp. 315–324.
- [90] R Su, H Zhang, DJ O’Connor, L Shi, X Meng, and H Zhang. “Deposition and characterization of  $Ti_2AlC$  MAX phase and  $Ti_3AlC$  thin films by magnetron sputtering”. In: *Materials Letters* 179 (2016), pp. 194–197.
- [91] RN Tait, T Smy, and MJ Brett. “Modelling and characterization of columnar growth in evaporated films”. In: *Thin Solid Films* 226.2 (1993), pp. 196–201.
- [92] C Tang, M Klimenkov, U Jaentsch, H Leiste, M Rinke, S Ulrich, M Steinbrück, HJ Seifert, and M Stueber. “Synthesis and characterization of  $Ti_2AlC$  coatings by magnetron sputtering from three elemental targets and ex-situ annealing”. In: *Surface and Coatings Technology* 309 (2017), pp. 445–455.
- [93] Tengfei Zhang. “Syntheses and properties of  $Ti_2AlN$  MAX-phase films”. In: *Journal of Ceramic Processing Research* 13.Special 1 (2012), pp. 149–153.
- [94] JA Thornton. “Influence of apparatus geometry and deposition conditions on the structure and topography of thick sputtered coatings”. In: *Journal of Vacuum Science and Technology* 11.4 (1974), pp. 666–670.
- [95] C Torres. Lima, Peru, 2022.
- [96] C Torres, R Quispe, NZ Calderón, L Eggert, M Hopfeld, C Rojas, MK Camargo, A Bund, P Schaaf, and R Grieseler. “Development of the phase composition and the properties of  $Ti_2AlC$  and  $Ti_3AlC_2$  MAX-phase thin films – A multilayer approach towards high phase purity”. In: *Applied Surface Science* 537 (2021), p. 147864.
- [97] E Unosson. *Antibacterial Strategies for Titanium Biomaterials*. Vol. 1250. Digital Comprehensive Summaries of Uppsala Dissertations from the Faculty of Science and Technology. Uppsala: Acta Universitatis Upsaliensis, 2015.

- [98] DK Unruh and TZ Forbes. “X-ray Diffraction Techniques”. In: *Analytical Geomicrobiology*. Ed. by JPL Kenney, H Veeramani, and DS Alessi. Cambridge University Press, 2019, pp. 215–237.
- [99] B Wang, M Wang, F Liu, Q Zhang, S Yao, X Liu, and F Huang. “Ti<sub>3</sub>C<sub>2</sub>: An Ideal Co-catalyst?” In: *Angewandte Chemie* 132.5 (2020), pp. 1930–1934.
- [100] B Wang, A Zhou, F Liu, J Cao, L Wang, and Q Hu. “Carbon dioxide adsorption of two-dimensional carbide MXenes”. In: *Journal of Advanced Ceramics* 7.3 (2018), pp. 237–245.
- [101] HW Wang, M Naguib, K Page, DJ Wesolowski, and Y Gogotsi. “Resolving the Structure of Ti<sub>3</sub>C<sub>2</sub>T<sub>x</sub> MXenes through Multilevel Structural Modeling of the Atomic Pair Distribution Function”. In: *Chemistry of Materials* 28.1 (2016), pp. 349–359.
- [102] K Wasa, M Kitabatake, and H Adachi. *Thin film materials technology: Sputtering of compound materials*. Norwich, NY: William Andrew Pub, 2004.
- [103] Y Wei, P Zhang, RA Soomro, Q Zhu, and B Xu. “Advances in the Synthesis of 2D MXenes”. In: *Advanced materials (Deerfield Beach, Fla.)* 33.39 (2021), e2103148.
- [104] *What is Raman Spectroscopy? - HORIBA*. 2/2/2022.
- [105] Wikipedia, ed. *Levenberg–Marquardt algorithm*. 2022.
- [106] Wikipedia, ed. *Space group*. 2022.
- [107] William D. Callister, Jr., David G. Rethwisch. *Materials Science and Engineering - An Introduction*. Eighth Edition. Wiley, 2013.
- [108] Woollam, John & Johs, Blaine & Herzinger, Craig & Hilfiker, James & Synowicki, Ron & Bungay, Corey. “Overview of Variable Angle Spectroscopic Ellipsometry (VASE), Part I: Basic Theory and Typical Applications.” In: *Proceedings of SPIE - The International Society for Optical Engineering* 1 (1999), pp. 3–28.
- [109] *X-ray Reflectivity*. 8/10/2022.
- [110] X.-K. Qian. “Electrical and Thermal Properties of Ti<sub>3</sub>AlC<sub>2</sub> at High Temperature”. In: *Journal of Ceramic Science and Technology* 2 (2011), pp. 155–158.
- [111] S Yang, P Zhang, F Wang, AG Ricciardulli, MR Lohe, PWM Blom, and X Feng. “Fluoride-Free Synthesis of Two-Dimensional Titanium Carbide (MXene) Using A Binary Aqueous System”. In: *Angewandte Chemie (International ed. in English)* 57.47 (2018), pp. 15491–15495.

- [112] W Yang, KR Ratinac, SP Ringer, P Thordarson, JJ Gooding, and F Braet. “Carbon nanomaterials in biosensors: should you use nanotubes or graphene?” In: *Angewandte Chemie (International ed. in English)* 49.12 (2010), pp. 2114–2138.
- [113] K Zhang, F Zhu, CHA Huan, and ATS Wee. “Effect of hydrogen partial pressure on optoelectronic properties of indium tin oxide thin films deposited by radio frequency magnetron sputtering method”. In: *Journal of Applied Physics* 86.2 (1999), pp. 974–980.
- [114] MD Zhu, C Shan, C Li, H Wang, HJ Qi, DP Zhang, and WZ Lv. “Thermochromic and Femtosecond-Laser-Induced Damage Performance of Tungsten-Doped Vanadium Dioxide Films Prepared Using an Alloy Target”. In: *Materials (Basel, Switzerland)* 11.9 (2018).





# List of Figures

1.1	Hexagonal crystal structure of the $M_{n+1}AX_n$ phases depending on the index $n$ ( $n = 1, 2, 3$ ) [42] . . . . .	1
1.2	Principles of oblique angle deposition (OAD) [14] . . . . .	2
2.1	Schematic of the target surface processes during the magnetron sputtering deposition [10] . . . . .	4
2.2	Schematic principle of magnetron sputtering by a) direct current (DC) and b) radio frequency (RF) [2] . . . . .	5
2.3	Schematic of the RF magnetron sputtering system of titanium, aluminium and carbon installed in the Physics Section at Pontificia Universidad Católica del Perú and employed in this work [72] . . . . .	6
2.4	Rapid Thermal Annealing (RTP) system configuration [3] . . . . .	7
2.5	a) Types of scattering processes that occur when monochromatic light interacts with a molecule; b) Electronic transitions and its resulting spectra (Reprinted from Reference [104]) . . . . .	8
2.6	Schematic principle of Raman spectrometer setup [81] . . . . .	9
2.7	Crystal structure of $P63/mmc$ space [105] . . . . .	11
2.8	Schematic representation of the vibrational modes of MAX phases depending on its stoichiometry a) 211 and b) 312 [76] . . . . .	12
2.9	Constructive interference described by Bragg's law [107] . . . . .	13
2.10	Schematic representation of X-Ray diffraction (XRD) a) in Bragg-Brentano configuration, where both the X-Ray source and the detector move, and b) in grazing incidence configurations, where only the detector is able to move [23] . . . . .	14
2.11	Schematical setup of a diffractometer [98] . . . . .	15
2.12	Information obtainable and derivable from diffraction experiments (Reprinted from Reference [89]) . . . . .	15
2.13	a) Schematic representation of EDX principle [49]; b) Possible electron transitions and their atomic orbital notation [54] . . . . .	17
2.14	a) SEM functional principle [8]; b) EDX spectrum [21] . . . . .	18

2.15	Schematic of a square 4P probe configuration where the space between the contacts can be described with $s_1 = s_4 = s$ and $s_3 = s_4 = \sqrt{2}s$ [67]	19
2.16	Schematic diagram of spectroscopic ellipsometry system [66]	20
2.17	Schematic of interaction of linearly polarized light with a sample [47]	21
2.18	Schematic of effect to determine thin film thickness with spectroscopic ellipsometry in a multilayer system [12]	22
2.19	Schematic principle of synthesis of MXenes nanosheets [111]	24
2.20	Etching process with 1 % HF by using a Teflon protective mask (indicated in yellow)	24
3.1	SEM top-view image of the Ti, Al and C monolayers as deposited	26
3.2	EDX results in at % of the as deposited titanium, aluminum, and carbon monolayers. Further details of the measurement as well as the corresponding EDX spectra can be found in the annex	26
3.3	X-ray Reflectivity curves (black) of Ti, Al, and C (+ Ti) monolayers deposited on silicon substrates and simulated fitting curves (red) obtained by Leptos. Notice that the values in the x-axis are different for each graph	27
3.4	a) Schematic of co-deposition with elemental Ti, Al and C targets (Adapted from Ref. [97]) b) Schematic of co-deposition with a $Ti_2AlC$ target (Adapted from Ref. [114]) c) Schematic of mosaic target of Ti, Al and C (Adapted from Ref. [17])	29
3.5	Phase diagram for Ti-Al-C [22]	30
3.6	Schematic representation of the deposition of Ti-Al-C multilayer system (Reprinted from Reference [96])	31
3.7	Chemical composition of thin films with various deposition configurations as deposited and its corresponding Ti:Al ratio	33
3.8	EDX analysis of titanium, aluminum and carbon in thin films deposited at different configurations as deposited and after annealing processes using the tubular alumina oven (600 °C, 700 °C, 800 °C, 900 °C and 1000 °C) taking into account only the above mentioned elements. Notice that the lines draw between the data were not measured and are only included to guide the eye.	34

3.9	EDX analysis of thin films deposited at different configurations as deposited and after annealing processes using the tubular alumina oven (600 °C, 700 °C, 800 °C, 900 °C and 1000 °C) taking into account all elements. Notice that the lines draw between the dots were not measured and are only included to guide the eye. . . . .	35
3.10	BB-XRD patterns of Ti-Al-C co-deposited thin films deposited at different configurations as deposited and after annealing processes using a tubular alumina oven (800 °C and 1000 °C) . . . . .	36
3.11	Raman spectra of Ti-Al-C co-sputtered thin films deposited at different configurations as deposited and after annealing processes using a tubular alumina oven (600 °C, 700 °C, 800 °C, 900 °C and 1000 °C) . . . . .	37
3.12	Modes of growth of thin films: (a) Volmer–Weber island growth (b) Frank–van der Merwe layer growth and (c) Stranski-Krastanov layer plus island growth [38] . . . . .	39
3.13	Thornton structure zone model [94] . . . . .	40
3.14	Scheme of oblique angle deposition (OAD) outlining the influence of the deposition angle $\alpha$ in the resultant angle $\beta$ due to atomic self-shadowing effect [20] . . . . .	41
3.15	Schematic of the L-shaped substrate holder employed in this work. Notice that the material flux arriving from the target is simplified as two points to ease the angle calculation . . . . .	42
3.16	Schematic of sample holder and SEM cross-section images of samples deposited at OAD as prepared [95] . . . . .	44
3.17	Top-view SEM images of a) MAX phase thin film deposited at normal-configuration, and b-d) OAD deposited thin films with different column tilt angle as prepared [95] . . . . .	45
3.18	Top-view SEM images of OAD deposited thin films with different column tilt angles at different annealing temperatures using a RTP oven [95] . . . . .	46
3.19	Chemical composition of MAX phases deposited at oblique angle configuration ( $\beta \sim 23^\circ$ , $\gamma \sim 31^\circ$ and $\delta \sim 27^\circ$ ) and annealed at 700 °C and 900 °C by RTP process . . . . .	47
3.20	BB-XRD diffractograms of oblique angle deposited MAX phase thin films ( $\beta \sim 23^\circ$ , $\gamma \sim 31^\circ$ and $\delta \sim 27^\circ$ ) and reference MAX phase sample annealed at different temperatures using RTP . . . . .	48
3.21	Raman spectra of oblique angle deposited thin films ( $\beta \sim 23^\circ$ , $\gamma \sim 31^\circ$ and $\delta \sim 27^\circ$ ) annealed at 700 °C and 900 °C using RTP process . . . . .	49

4.1	Top-view SEM images of surface of MAX phase ( $\text{Ti}_2\text{AlC}$ and $\text{Ti}_3\text{AlC}_2$ ) deposited at normal configuration and annealed at $900^\circ\text{C}$ by RTP process after 2 h selective etching a) at 800x b) at 1600x . . . . .	50
4.2	Top-view SEM image of MAX phase ( $\text{Ti}_2\text{AlC}$ and $\text{Ti}_3\text{AlC}_2$ ) thin film surface annealed at $900^\circ\text{C}$ by RTP process a) as deposited and b) after 2 hours HF selective etching . . . . .	51
4.3	EDX analysis of MAX phases as deposited and after 2 hours selective HF etching. The ratio Ti:Al of both samples is indicated in the Table 4.1	52
4.4	Schematic of resulting morphology of MAX thin film phases after HF selective etching. Notice that the $\text{SiO}_2$ thin film is not depicted as it is not specified by the substrate producer . . . . .	53
4.5	GI-XRD diffractogram sections of MAX phase thin film annealed at $900^\circ\text{C}$ a) as prepared and b) after 2 hours HF etching with variable incident angle ( $0.75^\circ - 3^\circ$ ). The diffractograms can be found in the annex.	54
4.6	FWHM and peak position analysis of the XRD spectrum of MAX phases annealed at $900^\circ\text{C}$ as prepared with variable incident angle ( $0.5^\circ - 3^\circ$ ) .	55
4.7	FWHM and peak position analysis of the XRD spectrum of MAX phases annealed at $900^\circ\text{C}$ after HF etching with variable incident angle ( $0.5^\circ - 3^\circ$ )	56
4.8	BB-XRD diffractogram of MAX phases annealed at $700^\circ\text{C}$ by RTP as deposited (violet) and after 2 hours HF etching (blue); and annealed at $700^\circ\text{C}$ with a subsequent $400^\circ\text{C}$ heat treatment (green) and after 2 hours HF etching (red) . . . . .	57
4.9	Raman spectra of MAX phases annealed at $700^\circ\text{C}$ RTP ( $\text{Ti}_2\text{AlC}$ ) as prepared and after 2 hours HF etching . . . . .	60
4.10	Raman spectra of MAX phases annealed at $900^\circ\text{C}$ ( $\text{Ti}_2\text{AlC}$ and $\text{Ti}_3\text{AlC}_2$ ) by RTP process as prepared and after 2 hours HF etching . . . . .	62
4.11	BB-XRD diffractogram of MAX phases annealed at $900^\circ\text{C}$ ( $\text{Ti}_2\text{AlC}$ and $\text{Ti}_3\text{AlC}_2$ ) as deposited and after 2 h HF etching . . . . .	63
4.12	Electrical resistivity of MAX phase thin films as prepared and after 2 h HF etching. Notice that the error bars are comparatively small in comparison with the symbol and therefore not visible (to be found in the annex) . . . . .	65
4.13	Top-view SEM images of nanostructured MAX phases deposited at OAD and annealed at $700^\circ\text{C}$ ( $\text{Ti}_2\text{AlC}$ ) by RTP process a) $\beta$ ( $23^\circ$ ) after 30 min HF etching b) $\gamma$ ( $31^\circ$ ) after 15 min HF etching c) $\delta$ ( $27^\circ$ ) after 15 min HF etching . . . . .	66

4.14	EDX analysis of nanostructured MAX phase deposited at OAD annealed at 700 °C via RTP as deposited and after various HF etching time . . .	67
4.15	Schematic of resulting morphology of nanostructured MAX phases deposited at OAD after HF selective etching with different column tilt angle. Notice that the objects are not represented in real scale . . . . .	68
4.16	BB-XRD diffractogram of MAX phase deposited at OAD ( $\beta_i \sim 23^\circ$ ) and annealed at 700 °C by RTP process as prepared and after 30 min HF etching . . . . .	69
4.17	Top-view SEM images of MAX phases deposited at OAD and annealed at 900 °C ( $\text{Ti}_2\text{AlC}$ and $\text{Ti}_3\text{AlC}_2$ ) by RTP process after 2 h HF etching process at different magnifications a) 10kx and b) 15kx . . . . .	70
4.18	Top-view SEM images of MAX phases deposited at OAD and annealed at 900 °C ( $\text{Ti}_2\text{AlC}$ and $\text{Ti}_3\text{AlC}_2$ ) by RTP process after 2 h HF etching with different column tilt angles ( $\beta$ ( $23^\circ$ ), $\gamma$ ( $31^\circ$ ) and $\delta$ ( $27^\circ$ )). Notice that only sample $\beta$ resisted until 150 minutes etching time, while the samples with the higher columns tilt angles ( $\delta$ and $\gamma$ ) resisted a total time of 120 minutes . . . . .	71
4.19	EDX analysis of nanostructured MAX phases deposited at OAD ( $\beta$ ( $23^\circ$ ), $\gamma$ ( $31^\circ$ ) and $\delta$ ( $27^\circ$ )) and annealed at 900 °C ( $\text{Ti}_2\text{AlC}$ and $\text{Ti}_3\text{AlC}_2$ ) by RTP process with different etching time. Notice that the lines draw between the dots were not measured and are only included to guide the eye	72
4.20	EDX analysis of nanostructured MAX phases deposited at OAD ( $\beta$ ( $23^\circ$ ), $\gamma$ ( $31^\circ$ ) and $\delta$ ( $27^\circ$ )) and annealed at 900 °C ( $\text{Ti}_2\text{AlC}$ and $\text{Ti}_3\text{AlC}_2$ ) by RTP process as prepared and after different etching time . . . . .	72
4.21	GI-XRD diffractogram of nanostructured MAX phases ( $\beta$ ( $23^\circ$ ), $\gamma$ ( $31^\circ$ ) and $\delta$ ( $27^\circ$ )) and annealed at 900 °C ( $\text{Ti}_2\text{AlC}$ and $\text{Ti}_3\text{AlC}_2$ ) by RTP process as prepared and after the etching process . . . . .	74
4.22	BB-XRD diffractogram of MAX phase deposited at OAD ( $\beta$ ( $23^\circ$ ), $\gamma$ ( $31^\circ$ ) and $\delta$ ( $27^\circ$ )) and annealed at 900 °C ( $\text{Ti}_2\text{AlC}$ and $\text{Ti}_3\text{AlC}_2$ ) by RTP process as prepared and after HF etching . . . . .	76
4.23	Corrected schematical of Figure 4.14 after analyzing the experiment results	77
4.24	Raman spectra of MAX phases deposited at OAD ( $\beta$ ( $23^\circ$ ), $\gamma$ ( $31^\circ$ ) and $\delta$ ( $27^\circ$ )) and annealed at 900 °C ( $\text{Ti}_2\text{AlC}$ and $\text{Ti}_3\text{AlC}_2$ ) by RTP process as prepared and after several HF etching time . . . . .	78

4.25	Raman spectra of MAX phases deposited at OAD ( $\beta$ ( $23^\circ$ ), $\gamma$ ( $31^\circ$ ) and $\delta$ ( $27^\circ$ )) and annealed at $900^\circ\text{C}$ ( $\text{Ti}_2\text{AlC}$ and $\text{Ti}_3\text{AlC}_2$ ) by RTP process as prepared and after the HF etching process . . . . .	80
6.1	Variable-angle spectroscopic ellipsometry measurements of titanium monolayer for thickness determination . . . . .	107
6.2	Variable-angle spectroscopic ellipsometry measurements of Al monolayer for thickness determination . . . . .	108
6.3	Variable-angle spectroscopic ellipsometry measurements of C monolayer for thickness determination . . . . .	108
6.4	GI-XRD diffractogram of MAX phases annealed at $900^\circ\text{C}$ as prepared with different incident angle . . . . .	109
6.5	GI-XRD diffractogram of MAX phases annealed at $900^\circ\text{C}$ after HF etching with different incident angle . . . . .	109



## List of Tables

2.1	Raman shift ( $\text{cm}^{-1}$ ) of the Raman mode of the 211 MAX phases . . . .	11
2.2	Raman shift ( $\text{cm}^{-1}$ ) of the Raman mode of the 312 MAX phases . . . .	11
3.1	Sputtering conditions of titanium, aluminum, and carbon monolayers .	25
3.2	Obtained values (thickness, roughness and density) of the titanium, aluminum and carbon monolayers obtained by X-Ray refraction (XRR)	28
3.3	Measured thickness values of titanium, aluminum, and carbon monolayers by variable-angle spectroscopic ellipsometry (VASE) and X-Ray reflectometry (XRR) . . . . .	28
3.4	Deposition parameters for Ti-Al-C multilayer system to achieve the necessary stoichiometry of the MAX phase . . . . .	31
3.5	Incident vapor angle $\alpha$ , theoretical and experimental tilt angle $\beta$ of the as deposited thin films . . . . .	44
3.6	Ti:Al ratio of nanostructured MAX phases as prepared . . . . .	47
4.1	Ti:Al ratio of MAX phase thin film annealed at 700 °C and 900 °C by RTP process as prepared and after 2 h HF etching . . . . .	52
4.2	Peak position of MAX phases annealed at 700 °C by RTP process and MAX phases annealed at 700 °C by RTP process with a subsequent thermal process at 400 °C for 2 hours, which peaks are located at $2\theta \sim 13^\circ$ and $2\theta \sim 39^\circ$ and obtained from Figure 4.8. Difference between the peak position as deposited and after HF etching . . . . .	59
4.3	FWHM of MAX phases annealed at 700 °C by RTP process and MAX phases annealed at 700 °C by RTP process with a subsequent thermal process at 400 °C for 2 hours, which peaks are located at $2\theta \sim 13^\circ$ and $2\theta \sim 39^\circ$ and obtained from Figure 4.8. Difference between the FWHM value as deposited and after HF etching . . . . .	59
4.4	FWHM of characteristic peaks in Raman spectra (Figure 4.9) of MAX phases annealed at 700 °C ( $\text{Ti}_2\text{AlC}$ ) by RTP process as prepared and after 2 hours HF etching . . . . .	61
4.5	FWHM of characteristic peaks in Raman spectra (Figure 4.10) of MAX phases annealed at 900 °C ( $\text{Ti}_2\text{AlC}$ and $\text{Ti}_3\text{AlC}_2$ ) by RTP process as prepared and after 2 hours HF etching. . . . .	63
4.6	Peak position of MAX phases annealed at 900 °C by RTP process and MAX phases annealed at 900 °C by RTP process with a subsequent thermal process at 400 °C for 2 hours, obtained from Figure 4.11. Difference between the peak position as deposited and after HF etching . . . . .	64
4.7	FWHM of MAX phases annealed at 900 °C by RTP process and MAX phases annealed at 900 °C by RTP process with a subsequent thermal process at 400 °C for 2 hours, obtained from Figure 4.11. Difference between the FWHM values as deposited and after HF etching . . . . .	64
4.8	Etching time passed before delamination for MAX phases deposited at oblique angle deposition and annealed at 700 °C and 900 °C by RTP process . . . . .	66



4.9	Ti:Al ratio of MAX phases deposited at OAD and annealed at 700 °C (Ti <sub>2</sub> AlC) by RTP process as deposited and after HF etching . . . . .	67
4.10	Ti:Al ratio of MAX phases deposited at OAD ( $\beta$ (23°), $\gamma$ (31°) and $\delta$ (27°)) and annealed at 900 °C (Ti <sub>2</sub> AlC and Ti <sub>3</sub> AlC <sub>2</sub> ) by RTP process as deposited and after HF etching . . . . .	73
4.11	Peak position of peak located at $2\theta \sim 9.5^\circ$ . Notice that the analysis of the diffraction peak (002) Ti <sub>2</sub> AlC could not be carried out due to the lack of data as prepared. Difference between the peak position as deposited and after HF etching . . . . .	74
4.12	FWHM of peak located at $2\theta \sim 9.5^\circ$ . Notice that the analysis of the diffraction peak (002) Ti <sub>2</sub> AlC could not be carried out due to the lack of data as prepared. Difference between the FWHM value as deposited and after HF etching . . . . .	74
4.13	Peak position of the (002) Ti <sub>3</sub> AlC <sub>2</sub> peak as prepared and after HF etching of nanostructured MAX phase annealed at 900 °C by RTP process, and calculated down-shifting . . . . .	76
4.14	Calculated difference between FWHM value as prepared and after HF etching for nanostructured MAX phases annealed at 900 °C by RTP process . . . . .	77
4.15	FWHM values of nanostructured MAX phases deposited at OAD ( $\beta$ (23°), $\gamma$ (31°) and $\delta$ (27°)) and annealed at 900 °C (Ti <sub>2</sub> AlC and Ti <sub>3</sub> AlC <sub>2</sub> ) by RTP process as prepared and after the HF etching process . . . . .	81
6.1	Obtained chemical composition of the titanium, aluminum and carbon monolayers . . . . .	107
6.2	Resistivity values of MAX phase thin films as prepared and after 2 h HF etching . . . . .	110

# Annex

## Annex 1

Complementary information of Figure 3.2.

Table 6.1 Obtained chemical composition of the titanium, aluminum and carbon monolayers

Element	Titanium monolayer	Aluminum monolayer	Carbon monolayer
Carbon	$9.67 \pm 12.51$	$2.69 \pm 24.4$	$23.46 \pm 13.16$
Nitrogen	$10.18 \pm 10.57$	$0.74 \pm 17.27$	$1.08 \pm 53.62$
Oxygen	$10.24 \pm 10.55$	$1.72 \pm 3.75$	$2.26 \pm 15.62$
Silicon	$51.67 \pm 4.02$	$50.28 \pm 7.49$	$70.28 \pm 3.79$
Titanium	$18.24 \pm 7.74$	/	$2.92 \pm 18.85$

## Annex 2

Complementary information of Table 3.3.

### Titanium

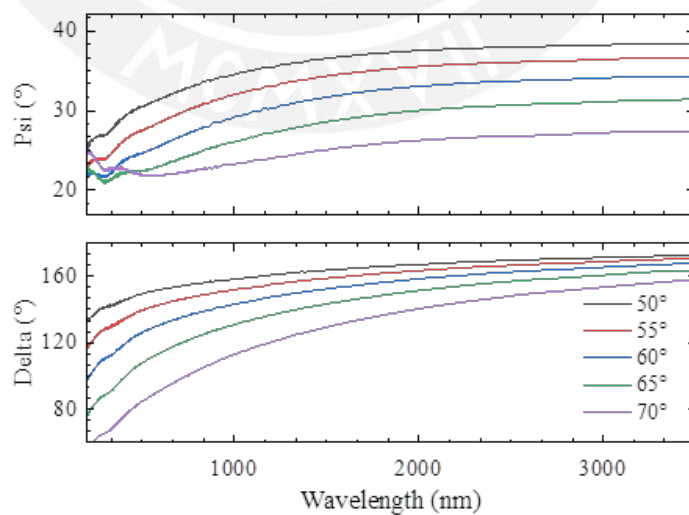


Figure 6.1 Variable-angle spectroscopic ellipsometry measurements of titanium monolayer for thickness determination

## Aluminum

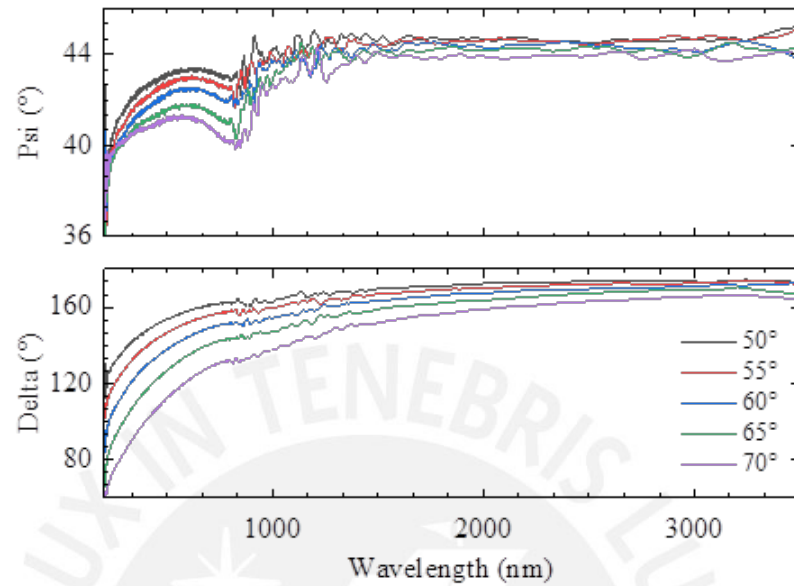


Figure 6.2 Variable-angle spectroscopic ellipsometry measurements of Al monolayer for thickness determination

## Carbon

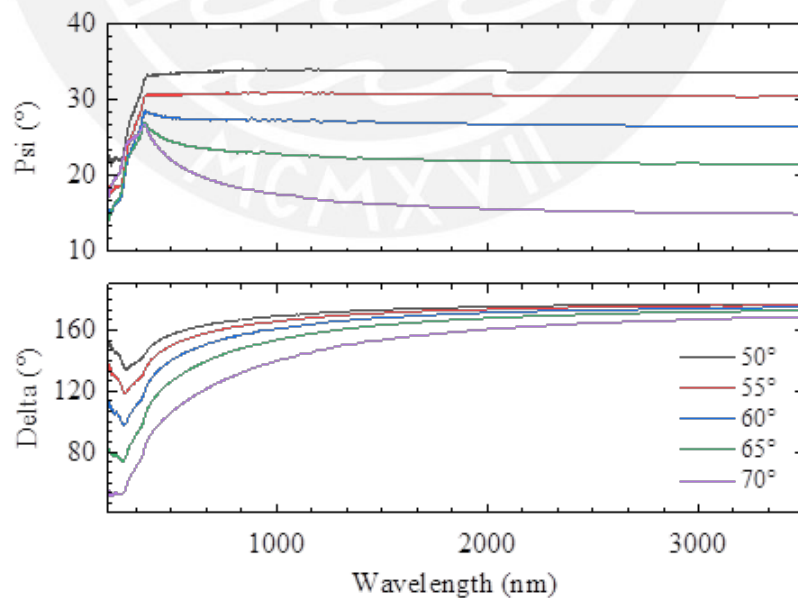


Figure 6.3 Variable-angle spectroscopic ellipsometry measurements of C monolayer for thickness determination

### Annex 3

Complementary information of Figure 4.5.

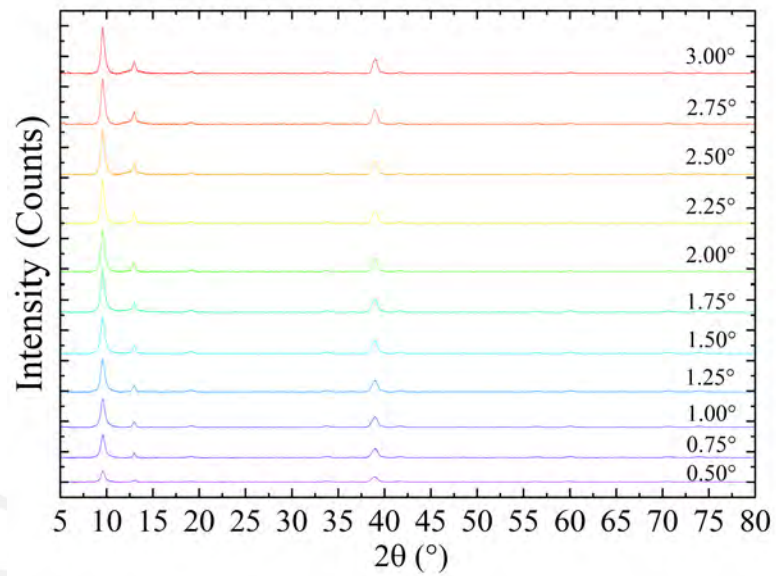


Figure 6.4 GI-XRD diffractogram of MAX phases annealed at 900 °C as prepared with different incident angle

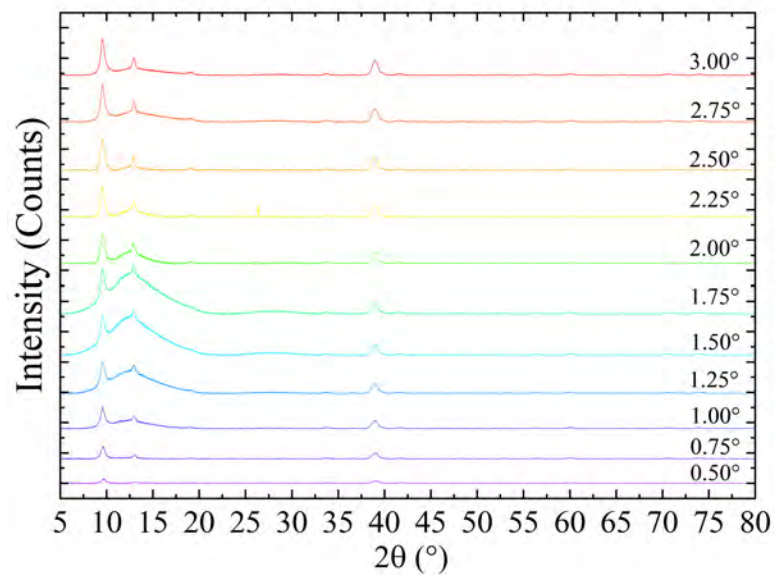


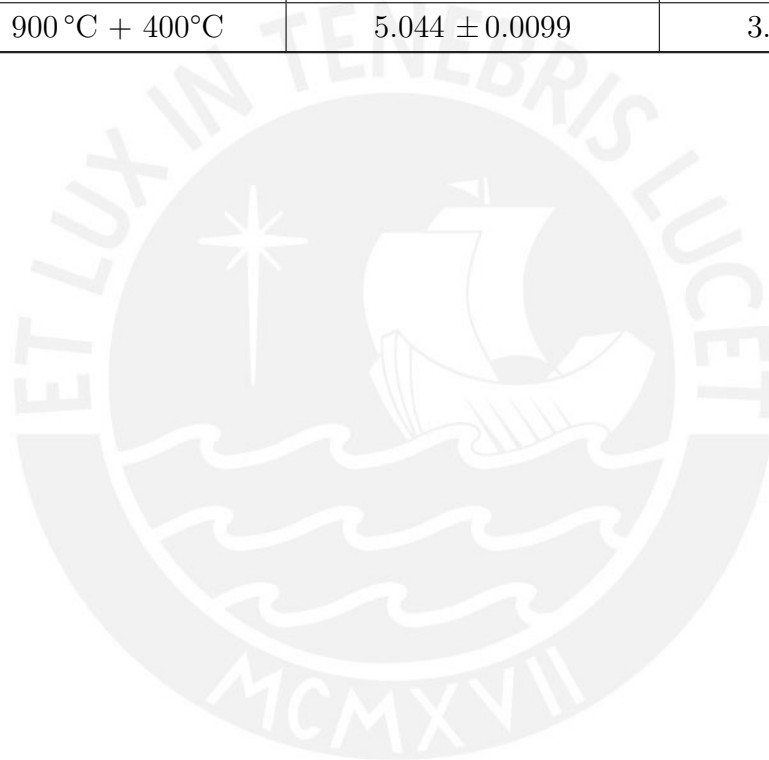
Figure 6.5 GI-XRD diffractogram of MAX phases annealed at 900 °C after HF etching with different incident angle

## Annex 4

Complementary information of Figure 4.12.

Table 6.2 Resistivity values of MAX phase thin films as prepared and after 2h HF etching

Sample	Resistivity As Prepared ( $\mu\Omega\text{ m}$ )	Resistivity After Etching ( $\mu\Omega\text{ m}$ )
RTP 700 °C	$5.1820 \pm 1.0860$	$4.0509 \pm 0.0042$
RTP 700 °C + 400°C	$5.3956 \pm 0.0035$	$4.6946 \pm 0.0021$
RTP 900 °C	$4.871 \pm 0.0084$	$3.522 \pm 0.0019$
RTP 900 °C + 400°C	$5.044 \pm 0.0099$	$3.041 \pm 0.0015$



# Eigenständigkeitserklärung

Ich erkläre hiermit, dass ich die vorliegende Arbeit selbständig verfasst und keine anderen als die angegebenen Quellen benutzt habe. Alle Gedanken, die aus fremden Quellen direkt oder indirekt übernommen wurden, sind als solche kenntlich gemacht. Die Arbeit wurde bisher keiner anderen Prüfungsbehörde vorgelegt und auch noch nicht veröffentlicht.

Ilmenau, 19.01.2023



## **Declaration of Originality**

I confirm that the submitted thesis is original work and was written by me without further assistance. Appropriate credit has been given where reference has been made to the work of others. The thesis was not examined before, nor has it been published. The submitted electronic version of the thesis matches the printed version.

Ilmenau, 19.01.2023

